

Nanostructured, Single-Phase Ferrite Materials:
Synthesis, Characterization, and Assessment of Their
Suitability for Photocatalytic Applications.

—

Dissertation

zur Erlangung des akademischen Grades

„*doctor rerum naturalium*“ (Dr. rer. nat.)

an der Fakultät für Biologie, Chemie und Geowissenschaften
der Universität Bayreuth

Vorgelegt von

André Blößer

Geboren in Königstein im Taunus

Die vorliegende Arbeit wurde in der Zeit von Oktober 2016 bis September 2018 in Gießen am Institut für Physikalische Chemie, sowie in der Zeit von Oktober 2018 bis März 2020 in Bayreuth am Lehrstuhl für Physikalische Chemie III unter Betreuung vom Herrn Professor Dr. Roland Marschall angefertigt.

Vollständiger Abdruck der von der Fakultät für Biologie, Chemie und Geowissenschaften der Universität Bayreuth genehmigten Dissertation zur Erlangung des akademischen Grades eines Doktors der Naturwissenschaften (Dr. rer. nat.).

Dissertation eingereicht am: 13.08.2020

Zulassung durch die Promotionskommission: 16.09.2020

Wissenschaftliches Kolloquium: 14.12.2020

Amtierender Dekan: Prof. Dr. Matthias Breuning

Prüfungsausschuss:

Prof. Dr. Roland Marschall (Gutachter)

Prof. Dr. Birgit Weber (Gutachter)

Prof. Dr. Matthias Breuning (Vorsitz)

Prof. Dr. Josef Breu

Table of content

Abstract

Kurzfassung

1 Introduction	1
2 Theoretical background	5
2.1 Conversion of solar energy using semiconductors	5
2.2 Physiochemical background	7
2.3 Challenges concerning the activity of heterogeneous photocatalysts	11
2.3.1 (Nano-)structuring of photocatalysts	13
2.3.2 Co-catalysts	14
2.3.3 Heterojunctions	14
2.3.4 Sacrificial agents	15
2.4 Semiconducting materials in heterogeneous photocatalysis	16
2.5 Ferrites in photocatalysis	18
2.5.1 Magnesium ferrite – $MgFe_2O_4$	19
2.5.2 Calcium ferrite – $CaFe_2O_4$	22
2.6 The issue of phase purity	23
2.7 The electronic structure of ferrites	24
2.8 Magnetic properties of ferrites	26
2.9 Immobilization of magnetic photocatalysts in mesoporous host networks	29
3 Experimental Part	31
3.1 List of chemicals	31
3.2 Synthesis of spinel ferrites	32
3.2.1 $MgFe_2O_4$	32
3.2.2 $NiFe_2O_4$	33
3.2.3 $MnFe_2O_4$	33
3.3 Synthesis of $CaFe_2O_4$	33
3.4 Synthesis of KIT-6 type mesoporous SiO_2	34
3.5 Synthesis of $MgFe_2O_4@KIT-6 SiO_2$	35

3.6 Modification of the MgFe₂O₄@KIT-6 SiO₂ surface	35
3.7 Preparation of ferrite (photo-)electrodes	36
3.8 Characterization techniques and instrumentation	37
3.8.1 Electron microscopy	37
3.8.2 Diffraction based techniques	37
3.8.2.1 X-ray diffraction	37
3.8.2.2 Selected area electron diffraction.....	39
3.8.3 Spectroscopic methods	40
3.8.3.1 Infrared spectroscopy	40
3.8.3.2 Raman spectroscopy	40
3.8.3.3 UV-Vis-NIR spectroscopy.....	42
3.8.3.4 X-ray absorption near edge structure spectroscopy.....	43
3.8.3.5 Valence-to-core X-ray emission spectroscopy	44
3.8.3.6 Energy dispersive X-ray spectroscopy.....	46
3.8.3.7 Mössbauer spectroscopy	47
3.8.4 SQUID magnetometry	47
3.8.5 Thermoanalytic techniques.....	49
3.8.6 Nitrogen physisorption.....	49
3.8.7 Mercury intrusion porosimetry	50
3.8.8 Photocatalysis.....	51
3.8.8.1 Hydrogen evolution	51
3.8.8.2 Degradation of organic compounds.....	51
3.8.9 (Photo-)electrochemistry	52
3.8.9.1 Mott-Schottky analysis.....	52
3.8.9.2 Chopped-light linear sweep voltammetry and incident photon to current efficiency	53
4 Results and discussion	54
4.1 The microwave-assisted synthesis of MgFe₂O₄ nanoparticles.....	54
4.1.1 The phase composition	54
4.1.2 Optimization of the synthesis.....	55
4.2 Material characteristics of MgFe₂O₄ nanoparticles with optimized stoichiometry.....	56
4.2.1 Phase purity and crystal structure.....	56
4.2.2 Morphology	59
4.2.3 Magnetic properties	62
4.2.4 Optical properties.....	65
4.2.5 X-ray absorption and –emission characteristics.....	67
4.2.6 Photocatalysis and photoelectrochemistry	72

4.3 The microwave-assisted synthesis of other spinel ferrites	73
4.3.1 NiFe ₂ O ₄	73
4.3.2 MnFe ₂ O ₄	75
4.4 The microwave-assisted synthesis of macroporous CaFe₂O₄	78
4.4.1 Synthesis approaches for CaFe ₂ O ₄	78
4.4.2 Formation pathway of macroporous CaFe ₂ O ₄	80
4.4.3 Magnetic properties	85
4.4.4 Optical properties.....	86
4.4.5 X-ray emission spectroscopy	87
4.4.6 Photoelectrochemistry and photocatalysis.....	89
4.5 Microwave-assisted synthesis of macroporous MgFe₂O₄	90
4.6 Combination of MgFe₂O₄ with functional mesoporous host networks.....	92
4.6.1 Combination of MgFe ₂ O ₄ nanoparticles with KIT-6 type mesoporous SiO ₂	92
4.6.2 Combination of MgFe ₂ O ₄ nanoparticles with KIT-6 type mesoporous PMO.....	98
5 Conclusion and outlook	99
6 References	103
7 Appendix	111
7.1 Additional figures.....	111
7.2 List of symbols and abbreviations	116
7.3 Publications derived from this PhD work	118
7.4 Other publications	118
7.5 Contributions.....	119
8 Acknowledgements.....	120
9 Eidesstattliche Versicherung und Erklärung	122

Abstract

In this work the suitability of nanostructured ferrite materials with the general formula AFe_2O_4 (where A is a divalent cation) for photocatalytic applications is investigated. Spinel ferrite $MgFe_2O_4$ nanoparticles and macroporous $CaFe_2O_4$ sponge structures were produced by microwave-assisted syntheses in high-boiling organic solvents and subsequent calcination in air. The elemental composition of the products was monitored by energy dispersive X-ray spectroscopy and the synthesis procedures were optimized to ensure an ideal stoichiometry of the products. Phase purity of the products was confirmed by calcination studies combined with diffraction experiments and by a wide variety of spectroscopic techniques. The morphology of the ferrite materials is characterized by electron microscopy, gas physisorption and mercury intrusion porosimetry. Regarding the electronic band structure of ferrites, a vast dissent is found in published literature. This is addressed by a thorough characterization of the electronic structure using photoelectrochemical measurements, X-ray based spectroscopic techniques, and by a detailed interpretation of their optical absorption spectra. The determined band positions suggest that $CaFe_2O_4$ is suitable for photocatalytic hydrogen evolution under visible light, while $MgFe_2O_4$ is not. Nevertheless, both phases remain inactive in hydrogen evolution test reactions as well as other photocatalytic experiments. X-ray based spectroscopy suggests that the presence of a transition metal with d^5 electronic configuration causes a strong discrepancy between the fundamental electronic band gap and the one determined by optical spectroscopy. The Fe^{3+} crystal field orbitals involved in the ligand-to-metal charge transfer excitations that are responsible for the absorption of visible light are highly localized at the Fe^{3+} centers. The weak orbital overlap causes a low mobility of excited charge carriers explaining the inactivity in photocatalysis. Additional to the optical and photocatalytic properties, the magnetism of the synthesized materials is investigated by Mössbauer spectroscopy and SQUID magnetometry. While $CaFe_2O_4$ exhibits antiferromagnetic behavior, the $MgFe_2O_4$ nanoparticles exhibit a tunable magnetization, that depends on crystallite size and cation inversion and is therefore adjustable by post-synthetic calcination. First attempts towards the synthesis of magnetic $NiFe_2O_4$ and $MnFe_2O_4$ nanoparticles were made, to extend the scope of magnetic nanoparticles that can be synthesized *via* the microwave-assisted reaction. Attempting to combine the optical and magnetic characteristics of ferrites with other chemical functionalities in a composite material, phase-pure $MgFe_2O_4$ nanoparticles were immobilized on functionalized, ordered-mesoporous SiO_2 and organosilica host networks.

Kurzfassung

In dieser Arbeit wird die Tauglichkeit von Ferrit-Nanostrukturen mit der allgemeinen Summenformel AFe_2O_4 (wobei A ein divalentes Kation repräsentiert) für Anwendungen in der Photokatalyse untersucht. Nanopartikel mit der Summenformel $MgFe_2O_4$, sowie $CaFe_2O_4$ mit einer schwammartigen Makroporenstruktur wurden mittels eines mikrowellenbasierten Verfahrens in hochsiedenden organischen Lösungsmitteln und anschließender Temperaturbehandlung an Luft synthetisiert. Die elementare Zusammensetzung der Produkte wurde mittels energiedispersiver Röntgenspektroskopie überwacht und die Syntheseprotokolle wurden optimiert, um eine ideale Produktstöchiometrie zur Bildung von Ferritstrukturen zu gewährleisten. Die Phasenreinheit der Produkte wird in Kalzinationsstudien in Verbindung mit Diffraktionsexperimenten und einer breiten Auswahl spektroskopischer Techniken bestätigt. Die Morphologie der Materialien wird mittels Elektronenmikroskopie, sowie N_2 -Physisorption und Quecksilberporosimetrie charakterisiert. Hinsichtlich der elektronischen Bandstruktur von Ferriten herrscht in der verfügbaren Literatur eine große Uneinigkeit, weshalb die elektronischen Eigenschaften anhand von photoelektrochemischen Messungen, Röntgenspektroskopie, sowie optischer Spektroskopie detailliert diskutiert werden. Die ermittelten Bandpositionen deuten darauf hin, dass photokatalytische Wasserstoffproduktion mit $CaFe_2O_4$ möglich ist, während $MgFe_2O_4$ dazu ungeeignet ist. Nichtsdestotrotz zeigen beide Phasen in durchgeführten Testreaktionen zur Wasserstoffentwicklung, sowie in anderen photokatalytischen Experimenten keine Aktivität. Röntgenspektroskopische Untersuchungen legen nahe, dass aufgrund der Präsenz eines Übergangsmetalls mit d^5 Elektronenkonfiguration im Falle von Ferriten eine starke Diskrepanz zwischen der elektronischen Bandlücke und der aus optischen Messungen bestimmten Bandlücke besteht. Die Ligand-zu-Metall *Charge-Transfer* Übergänge, welche für die Absorption von sichtbarem Licht verantwortlich gemacht werden, gehen aufgrund von schwacher Orbital-Überlappung mit einer starken Lokalisation der angeregten Ladungsträger einher, was die geringe Ladungsträgermobilität und die ausbleibende Aktivität in der Photokatalyse erklärt. Neben den elektronischen Eigenschaften wurde der Magnetismus der Materialien mittels Mößbauer-Spektroskopie und SQUID Magnetometrie untersucht. Während $CaFe_2O_4$ antiferromagnetisches Verhalten zeigt, weisen die $MgFe_2O_4$ Nanopartikel, abhängig von Kristallitgröße und Inversionsgrad, eine variable Magnetisierung auf, die durch die Temperaturbehandlung während der Synthese variiert werden kann. Erste Versuche hin zur Synthese von magnetischen $NiFe_2O_4$ und $MnFe_2O_4$ Nanopartikeln wurden unternommen, um den Anwendungsbereich der verwendeten Mikrowellensynthese zu untersuchen und zu erweitern. Außerdem wurden phasenreine $MgFe_2O_4$ Nanopartikel mit geordnet porösen Silica- und Organosilica Strukturen kombiniert um zu untersuchen, ob auf diese Weise die optischen und magnetischen Eigenschaften von Ferriten mit anderen chemischen Funktionalitäten in einem Kompositmaterial kombiniert werden können.

1 Introduction

The human-caused emission of greenhouse gases and the resulting change of climate and its consequences are considered to be among the most pressing challenges today's society is confronted with.^[1–3] In an ongoing transition from an energy industry that relies mostly on the burning of fossil fuels towards renewable energy sources, there is a huge demand for alternative ways to generate and store power. Tremendous achievements have already been made since the beginning of the twenty-first century. For example, solar and wind energy now make up a considerable part of the energy mix in many countries^[4], and lithium ion batteries have been established as an omnipresent technique to store power generated from renewable sources. The achievable energy densities of lithium ion cells have been increased drastically over the last decade. Their performance is however approaching physical boundaries and it proves ever harder to find new strategies to increase the energy density beyond the current limitations.^[5] While lithium ion batteries are highly convenient to power all kinds of smaller devices like mobile phones and personal computers, there are considerable drawbacks when very large amounts of energy have to be stored. While lithium ion cells are suitable to buffer power spikes in modern smart electrical grids, they are not able to provide the baseload in times where there is no sun or wind to drive the power plants. Reasons for that are their high price and the relatively short life span of the components, as well as the limited maximum power that can be drawn from such systems.^[6] Because of those disadvantages, lithium ion cells in combination with solar and wind energy (while certainly playing an integral part in the energy supply in the future) cannot be considered fitting to meet the long term energy demand of humanity alone. The consumption of energy is predicted to grow continuously over the next century and therefore viable alternatives for fuels have to be found.^[4] Hydrogen is considered by many as the energy carrier of the future, as it can be handled similar to fossil fuels when it comes to transport and storage. It can be used in combustion engines to drive cars and machines and it is possible to efficiently convert the chemical energy into electricity using fuel cells. In either case, water is formed as the only reaction product and therefore no noxious or climate-damaging gases are produced in contrast to the burning of coal, gas or oil-based fuels. While hydrogen therefore has a large potential as a green energy carrier, the available production processes often do not meet the demands of a decarbonized energy sector emphasizing on renewability. Most of the hydrogen produced today is generated *via* the steam reforming process – a nearly century-old technique relying on the dehydrogenation of hydrocarbons synthesized from natural gas and other fossil fuel sources.

From an environmental point of view, it is therefore much more appealing to generate the hydrogen by the endothermic splitting of water (Equation 1), which is basically the back reaction of hydrogen combustion, consequentially producing a closed circuit of resources.



In contrast to a carbon-based energy supply, where the recycling of the end-product carbon dioxide proves extremely challenging, water splitting can be achieved in a green fashion, either by electrolysis using the electrical current generated *via* renewable pathways, or directly by irradiation of an appropriate semiconductor with electromagnetic radiation. The latter technique is denoted photocatalysis or photoelectrochemistry, depending on the employed reaction setup. Its feasibility was first demonstrated by Fujishima and Honda in 1972^[7], who could prove that the absorption of light by titanium dioxide (TiO₂) creates an active species able to reduce protons and oxidize water. Up to this day, TiO₂ is the most-used and best-investigated material in photocatalysis and one of very few materials that is commercially produced specifically for this purpose.^[8] In 2014, the total global market for solar photocatalysts was amounted to 1.5 billion US\$ and a strong growth to nearly 2.9 billion US\$ until 2020 was predicted. The largest share of the market was however attributed to the construction industry, which utilizes TiO₂ mainly for the production of self-cleaning surfaces.^[9,10] The conversion of solar energy by water splitting or the synthesis of organic fine chemicals remain niche applications that have not surpassed the state of academic research yet. Besides hydrogen generation, other applications like the degradation of organic pollutants^[11,12], nitrogen fixation^[13] or the reduction of CO₂ have been considered for photocatalysts.^[14,15] The main reason why TiO₂ could not yet be established as a commercial water splitting photocatalyst is its inability to absorb most of the visible light spectrum. Absorption of visible light is a crucial factor in the development of materials for solar energy conversion, since the ultraviolet (UV) part of the solar spectrum (which can be effectively utilized by TiO₂) makes up only for a small part of the sunlight energy reaching the surface of earth (Figure 1). The efficiencies that can be achieved using TiO₂ are consequently too low to compete with modern multi-junction photovoltaic cells used to drive water electrolysis. Alternatives to TiO₂ with an extended absorption spectrum are therefore highly sought after.

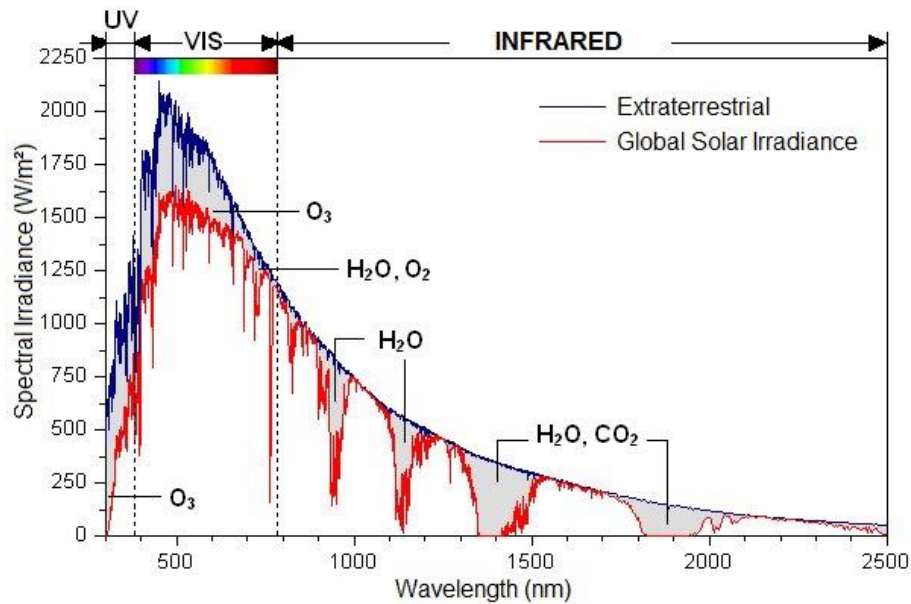


Figure 1: Solar irradiation reaching earth before (blue) and after interaction with the atmosphere (Image taken from [16]).

Over the last decade a wide variety of materials have been considered to meet the criteria for the suitability as a photocatalyst, which are (1) stability; (2) low cost; (3) abundance; (4) efficiency; (5) appropriate absorption characteristics; (6) corrosion resistance; and (7) suitability for large-scale production.^[17] In recent years, ferrites with the molecular formula $A\text{Fe}_2\text{O}_4$ (where A is a divalent cation) have been recognized for their promising absorption of visible light.^[18–20] Many of them consist solely of elements that are among the most prominent in the earth's crust, making them easily accessible and cheap.^[21] Most ferrites form crystals of the cubic spinel structure. Incorporation of larger cations like Ca^{2+} results in a one-dimensional stretching of the unit cell, so that an orthorhombic crystal structure is observed.^[22] Many among the known ferrites were already characterized regarding their electronic structure and photocatalytic performance. The reports show however a large dissent among their results and studies concerning the photocatalytic activity are mostly focused on the degradation of organic dyes, despite it is in many cases suggested that hydrogen reduction or even overall water splitting may be possible.^[19] The main goal of this work was therefore to provide a robust assessment of the suitability of ferrites for photocatalytic hydrogen generation. Syntheses based on microwave heating should be developed and optimized to produce nanostructured MgFe_2O_4 and CaFe_2O_4 . MgFe_2O_4 was chosen as a material of interest, because of its partially inverse spinel structure, which should allow an adjustment of the cation distribution in the crystal lattice *via* the synthesis conditions.^[23] It should be investigated how such a variation of the cation distribution influences the electronic structure and photocatalytic activity. CaFe_2O_4 on the other hand was investigated as it stands out among other ferrites, due to its orthorhombic crystal structure.^[22] The literature on the

electronic structure of CaFe_2O_4 is more consistent than in the case of MgFe_2O_4 and without exception the reported values suggest that the reduction of protons is possible using CaFe_2O_4 .^[19,24] The materials synthesized for this work were to be thoroughly characterized with an emphasis on phase purity, since even small amounts of an impurity can significantly alter the photocatalytic properties of a material. Advanced, hard X-ray based spectroscopic techniques should be employed for a thorough investigation of the electronic structure, since a precise determination of electronic band potentials *via* conventional techniques like Mott-Schottky analysis and optical spectroscopy seemingly proves problematic, as suggested by the large dissent among the literature reported data. Due to their magnetism, some of the synthesized materials can also be considered for magnetic applications, *e.g.* in Biomedicine.^[25,26] A characterization of the magnetic properties was therefore conducted as well. Additional to the production and characterization of pure ferrites, the materials should furthermore be immobilized in surface modified, mesostructured host materials, in an attempt to find strategies for the production of multi-functional composite catalysts combining photocatalysis with other types of catalysis (*e.g.* acid-base catalysis).

2 Theoretical background

2.1 Conversion of solar energy using semiconductors

Different semiconductor-based strategies are currently considered promising for the conversion of sunlight into chemical energy. Usually a coarse differentiation between photovoltaics-driven electrolysis, photoelectrochemistry, and particulate photocatalysis is made.^[27] Respective reaction setups for light driven water splitting are schematically depicted in Figure 2. The applicability of such generalized setups is however not limited to water splitting, but can be adapted to facilitate other chemical reactions as well.

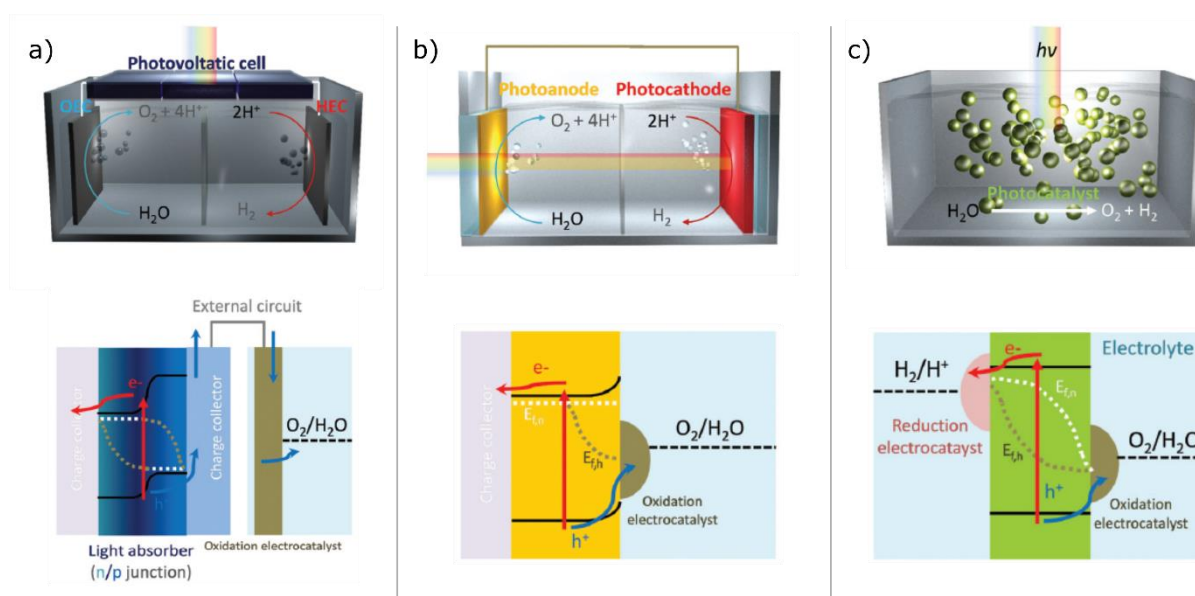


Figure 2: Different concepts for the semiconductor-based conversion of light into chemical energy. a) Photovoltaics driven electrolysis, b) Photoelectrochemistry, c) Particulate photocatalysis. Images taken from [27].

The techniques all rely on the same physicochemical principles for the absorption of light by a semiconductor (which are described in greater detail during the next subchapters) and come with individual advantages and disadvantages.

In a photovoltaics driven electrolysis setup, the light mediated current generation on one hand and the electrochemical reaction on the other hand are completely separated processes. Utilization of sunlight by photovoltaics is a commercially well-established technique and optimized production processes for photovoltaic cells are therefore already available. The spatial separation of absorber device and electrocatalyst offers great freedom in the design and dimensions of the individual components. The generation of an electrical current can be performed with an efficiency of 20–25% using conventional silicon based photovoltaic cells.^[28] Since typical single junction solar cells offer

open-circuit potentials that are lower than the potential needed to drive most chemical reactions of interest, either multiple cells must be connected in series, or power converters have to be employed, both of which may lead to lower efficiencies and higher costs.^[29] The achievable overall efficiency is therefore strictly limited by the performance of the photovoltaic cell and further decreased depending on the efficiency of the employed electrocatalyst.^[30]

Photoelectrochemistry relies on the irradiation of photoactive electrodes in contact with an electrolyte solution. The absorption properties of such systems can be optimized through the construction of tandem cells combining two or more photoactive materials, absorbing in different ranges of the light spectrum.^[31] Photoelectrodes are able to facilitate one half-reaction of a reduction-oxidation (RedOx) process, while the opposite charge is removed through a back contact, generating a photocurrent, which can for example be stored or used to drive another half-reaction in a purely electrocatalytic fashion. The contact with the liquid electrolyte leads to the formation of a space charge layer at the interface that benefits the separation of excited charge carriers (see chapter 2.3). Furthermore, an external electric potential can be applied through a voltage source to further improve charge carrier separation and to adjust the potential of the charge carriers that take part in the RedOx reaction at the semiconductor-electrolyte interface. The contact with aqueous electrolyte solutions however may also reduce the lifetime of the photoelectrode due to corrosion^[32], and the scalability of such systems is presumed limited due to difficulties in engineering.^[29]

Particulate photocatalysis relies on the utilization of light to facilitate both oxidative and reductive tasks simultaneously on single heterogeneous photocatalyst particles in suspensions. Excited charge carriers with positive and negative charge that are generated upon illumination of the particle must therefore be separated from another and diffuse to active sites at the surface, where they can undergo electrocatalytic reactions. Since it is not possible to apply an external bias on individual particles in such a system, the electronic structure of the semiconductor must be appropriate to facilitate the target reaction. Additionally, it is often mandatory to combine the absorber material with small amounts of an additional electrocatalyst (a so-called co-catalyst) to facilitate the charge transfer from the semiconductor particle to the reactant. As photocatalysis combines the processes of light absorption and chemical reaction on a single particle, it offers a more direct approach for the conversion of solar energy. Reaction setups are less complex compared to the concepts based on photovoltaic cells or photoelectrodes and consequentially they are easily scalable in most cases.^[29] Since many ferrites are comprised of cheap and abundant elements and therefore make up promising candidates especially for application at the large scale, the focus of this work was laid on the applicability of ferrites in particulate photocatalytic systems.

2.2 Physiochemical background

The electronic structure of a crystalline solid can be derived by a linear combination of atomic orbitals (LCAO), similar to the construction of molecular orbitals for smaller compounds. Since the number of contributing atom orbitals gets extremely large in bulk solids, the resulting crystal orbitals typically are delocalized and show a strong energetic dispersion (Figure 3).

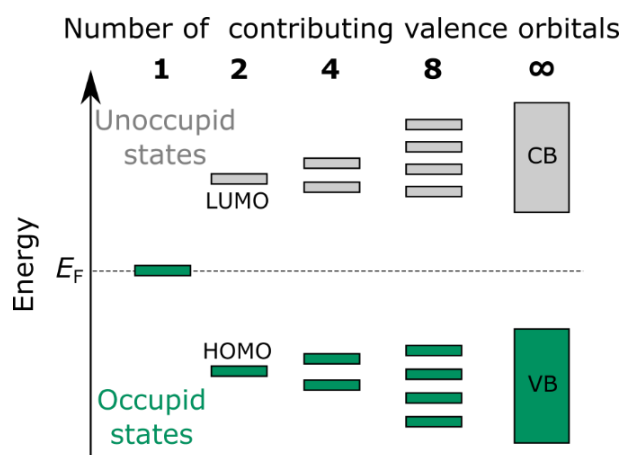


Figure 3: Scheme illustrating the formation of energy bands through linear combination of atomic orbitals.

Because of this dispersion, the electronic structure of crystalline solids is more conveniently described by the density of states (DOS) at a specific energy or simplified as energy bands. Energies at which no electronic states exist are consequently denoted band gaps. According to the *Aufbau* principle, the available electronic states of the solid in the ground state are filled with electrons starting from the band lowest in energy. The energies of the respective states correspond to the *eigenvalues* of the Bloch wave function $\Psi(\vec{r})$ of the electrons (Equation 2), where \vec{k} is the wave vector, \vec{r} is the position in the crystal lattice and $u(\vec{r})$ is a function that represents the periodicity of the respective crystal lattice.^[33]

$$\Psi(\vec{r}) = e^{i\vec{k}\cdot\vec{r}} \cdot u(\vec{r}) \quad (2)$$

Due to the periodic nature of crystalline solids, it is sufficient to calculate the energies for the first Brillouin zone of the reciprocal lattice to derive their electronic structure. Similar to the highest occupied molecular orbital (HOMO) and the lowest unoccupied molecular orbital (LUMO) in a molecule, the highest occupied electron band (valence band, VB) and the lowest unoccupied electron band (conduction band, CB) define the electrochemical characteristics of the solid. Electrons in the core bands are strongly bound to the atomic nuclei and therefore play no role in RedOx chemistry, while the valence electrons can move through the crystal lattice with relative ease and may also be transferred to surface bound reactants. The band gap between VB and CB can be classified as either

direct or indirect, depending on the position of the valence band maximum (VBM) and conduction band minimum (CBM) in the first Brillouin zone. If VBM and CBM share the same k-vector, the respective transition is called *direct* (Figure 4). If, on the other hand, VBM and CBM are shifted on the k-vector axis, an excitation of a valence band electron into the conduction band additionally requires the absorption of a lattice vibration (phonon), to compensate for the difference in momentum. The respective band gap is denoted *indirect* in that case. Since the absorption of a phonon has a limited probability, the direct excitation of an electron from the VB to the CB can be induced with a higher efficiency. Nevertheless, the lifetime of the excited state is usually increased for materials with an indirect band gap, since the corresponding disexcitation is also a phonon mediated process, resulting in a prolonged lifetime of the excited state. Indirect semiconductors are therefore often considered better suited for an application as photocatalyst.

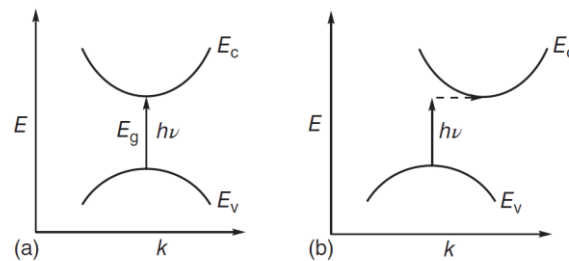


Figure 4: Schematic depiction of a direct and an indirect band gap. E_c and E_v are the energies of the CB and VB states, respectively (Image taken from [34]).

Depending on the position of their Fermi level (E_F), solids can be classified as either metallic, semiconducting or insulating. From a statistical point of view, the Fermi level reflects the energy where the probability of an electron occupying an available energy state is exactly 0.5.^[34] The Fermi level is therefore correlated to the energetic position of occupied and unoccupied states in the band structure. In case of a metallic solid, the Fermi level is located inside the valence band. A large number of unoccupied states just above the Fermi level allows for an effortless thermal activation of the valence electrons, causing the high electronic conductivity that is well known for metals. For semiconductors and insulators, the VB is completely filled with electrons, while the CB is constituted by empty electronic states. The differentiation between semiconductor and insulator is often made according to the energy of band gap (E_g) separating VBM and CBM. The threshold between semiconductor and insulator is not precisely defined, yet materials with a band gap smaller than 4 eV are usually treated as semiconductors, while those with larger band gaps are considered to be insulators (or wide-gap semiconductors in some cases). In the case of an ideal intrinsic semiconductor, the Fermi level is located exactly in the middle of the band gap. Most real semiconductors however possess a Fermi level that is located either near the VB or the CB, due to the presence of donor- or acceptor states,

originating from crystal defects or purposely introduced dopants. Depending on the nature of those states, the electronic structure of the semiconductor facilitates either the conduction of electrons *via* the CB (negatively charged, *n*-type) or defect electrons in the VB (positively charged, *p*-type), as the majority charge carriers (Figure 5a).

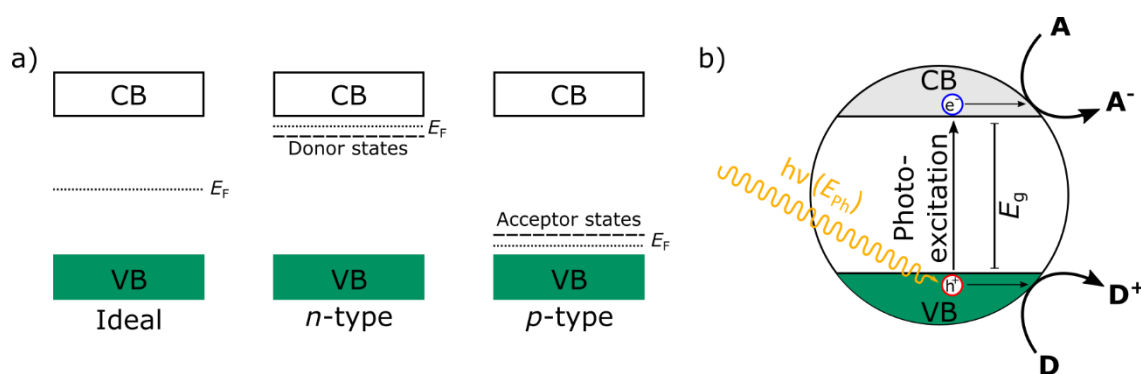


Figure 5: a) Scheme depicting the change of the fermi level energy upon introduction of donor or acceptor states in comparison to an ideal intrinsic semiconductor. b) Simplified scheme illustrating the light induced excitation of a VB electron into the CB, followed by diffusion to the surface and reaction with an adsorbed electron acceptor (A) or electron donor (D).

The band gap of many ceramic semiconductors is too large to allow a thermal activation of VB electrons into the CB at room temperature. The activation barrier can however be overcome when the semiconductor is exposed to electromagnetic radiation with a photon energy (E_{ph}) larger than E_g . For the utilization of visible light, the semiconductor must comprise a band gap in the range of 1.7–3.0 eV. Absorption of the photon leads to the excitation of a VB electron into the CB, leaving a defect electron remaining in the VB. Defect electrons are commonly denoted as a “holes” and for simplification they can be treated like positively charged quasiparticles with their own effective mass. Provided that the band potentials are suitable, excited electrons and holes can be transferred to surface adsorbed acceptor- and donor molecule respectively, forming a radical that is usually converted into a more stable product in a subsequent reaction (Figure 5b). Photon absorption and charge carrier separation are the basic principles of photocatalysis and photoelectrochemistry. When the charge carriers are transferred to chemical reactants and chemical bonds are broken and new ones are formed in the process, the radiative energy is effectively converted into chemical energy by the semiconductor. The thermodynamic potential of the product hereby must be energetically below that of the excited semiconductor-reactant adduct, but not necessarily below that of the adduct in the ground state (Figure 6). The term photocatalysis is therefore somewhat misleading, since the photocatalyst does not only influence the reaction kinetics (like in conventional catalysis), but instead can also facilitate reactions that have a thermodynamically uphill energy balance. A more precise nomenclature that differentiates between photocatalysis (energetically downhill) and artificial photosynthesis

(energetically uphill) has therefore been proposed.^[35] Such a differentiation will however not be made in the course of this work, since a strict separation of the two cases is not required here.

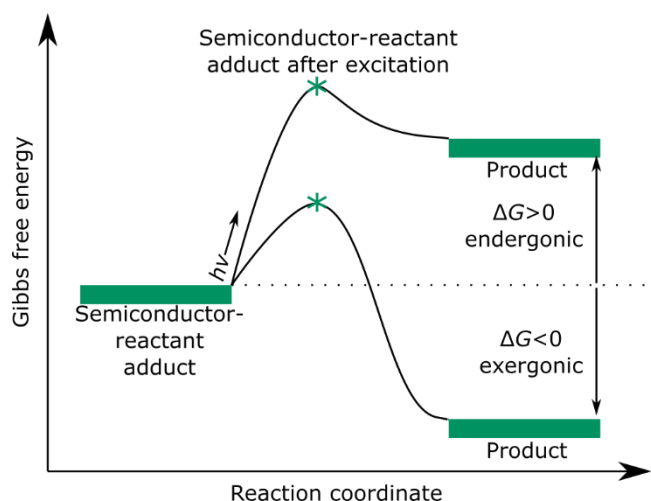


Figure 6: Thermodynamic course of an endergonic ($\Delta G > 0$) and exergonic ($\Delta G < 0$) photocatalytic reaction. After conversion of the reactant, the semiconductor is present in the ground state (Image adapted from [35]).

The required wavelengths to overcome the band gaps of conventional semiconductors range from the near infrared (NIR) regime, over visible light, up into the UV range. Because of the emission characteristics of the sun (See Figure 1, chapter 1), semiconductors with band gaps extending into the visible light region are much better suited for the conversion of solar energy than those which only absorb UV light. Small band gap semiconductors that show absorption already in the NIR regime on the other hand cannot provide the necessary driving force for most target reactions due to their unfavorable band positions. The utilization of NIR light for photocatalytic applications is therefore limited to some up-conversion materials nowadays.^[36–38]

To facilitate the endergonic process of overall water splitting, a minimum band gap of 1.23 eV is required from a purely thermodynamic point of view. The oxidation of water to form molecular oxygen is however a kinetically challenging process involving the accumulation and transfer of four holes in one step. Consequentially a large overpotential must usually be provided to facilitate the hole transfer. A band gap of at least 1.5–1.8 eV has therefore been proposed to be necessary to enable overall water splitting.^[39] A precise adjustment of the band gap of a photocatalyst (band gap engineering) is therefore usually required to make the best use of the incident light for the specific target reaction. The extent of the band gap can for example be adjusted *via* the introduction of dopants. For example, a narrowing of the band gaps of wide gap semiconductors like TiO_2 or $\text{Ba}_5\text{Ta}_4\text{O}_{15}$ was reported after anionic doping with nitrogen.^[40,41] In those examples, the oxygen atoms in the crystal lattice are partially replaced by nitrogen and due to the higher energy of the $\text{N}(2p)$ states compared to $\text{O}(2p)$, the VB undergoes a cathodic shift while the CBM remains mostly unaffected, thus decreasing the energy

gap. Cationic doping was also reported to influence the optical absorption characteristics in the case of TiO₂. However, this came at the cost of reduced thermal stability and shorter lifetimes of excited charge carriers, limiting the overall conversion efficiencies.^[42] Ferrites already exhibit a promising band gap for photocatalytic water splitting and therefore a further optimization of the band gap was not among the major goals of this work. Nevertheless, a correlation between the degree of cation inversion and the electronic band gap has been proposed in the case of spinel ferrites, which might open the way for a fine tuning of the band gap and band positions without the introduction of additional elements.^[43,44]

2.3 Challenges concerning the activity of heterogeneous photocatalysts

Even if a material has fitting band positions for a specific reaction, a high photocatalytic activity is not guaranteed. To promote chemical reactions, excited charge carriers must be separated and diffuse to active sites at the surface of the semiconductor, where they can be transferred to an adsorbed reactant. Hence, the mean free path of excited charge carriers must be larger than the distance between the area of charge generation and the surface for an effective utilization. The activity of a photocatalyst is therefore limited by the extent of recombination between the excited electrons and holes. Recombination is accompanied by the emission of fluorescence radiation and can occur directly (as the back reaction of the initial excitation) or via defect-state mediated pathways. Recombination is the most prominent pathway for a semiconductor to regain its ground state after excitation by light. The efficiency of a photocatalyst to promote a target reaction at a specific irradiation wavelength is commonly measured by its apparent quantum yield *AQY* which is given in percent and calculated by Equation 3, where *n* is the number of involved electrons in the photocatalytic reaction, *R* is the number of reacted molecules and *I* is the number of incident photons.

$$AQY = \frac{n \cdot R}{I} \cdot 100\% \quad (3)$$

Even the most sophisticated photocatalysts available today do not exceed 20% *AQY* at $\lambda=420$ nm and hence recombination is the fate of most of the excited electrons.^[27] For the development of high performance photocatalysts it is therefore of crucial importance to enhance the lifetime of excited charge carriers by diminishing the recombination probability. Since recombination usually takes place few nanoseconds after excitation, it can only be prevented by a rapid spatial separation of the excited electrons and holes. The separation of the opposite charges can be facilitated by an electric field. In the case of photoelectrodes, this is a minor issue, since the electric field can be applied externally using

a voltage source. For photocatalysts however, the situation is more complicated, as charge separation mostly relies on the presence of internal electric fields. When a semiconductor is brought into contact with an electrolyte solution, an electric field is generated at the semiconductor-electrolyte interface, due to Fermi level equilibration. The Fermi level equilibration is caused by the transfer of majority charge carriers from the semiconductor to the electrolyte, leading to the formation of a region that is depleted of this type of charge carriers (called depletion layer or space charge layer). In this surface-near region, the potentials of VB and CB states are altered, which is commonly depicted as a bending of the electronic bands (Figure 7).

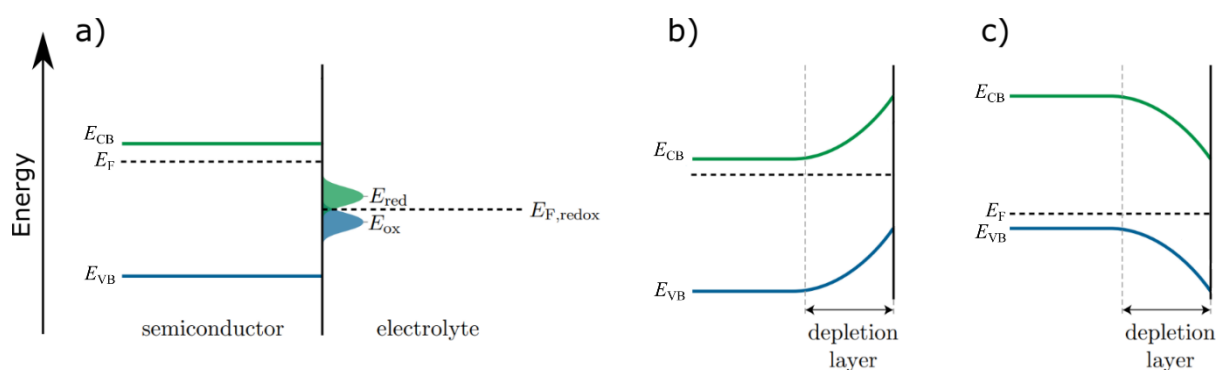


Figure 7: Band structure at the semiconductor-electrolyte interface before fermi level equilibration (a) and after equilibration for an *n*-type (b) and *p*-type (c) semiconductor. E_{ox} and E_{red} represent the oxidation potential and reduction potential at the RedOx Fermi potential $E_{F,redox}$ (adapted from [45]).

The local electric field facilitates the separation of excited charge carriers generated in the space charge layer. The width of the space charge layer W is dependent on the density of donor atoms in the material and can be approximated by Equation 4, where ϵ is the relative permittivity of the sample, ϵ_0 is the permittivity of vacuum, U_{sc} represents the extend of the potential drop in the space charge region, e is the electronic charge and N_D is the donor density.^[34]

$$W = \left(\frac{2\epsilon\epsilon_0 U_{sc}}{eN_D} \right) \quad (4)$$

The thickness of the space charge layer is commonly in the range of 100–1000 nm, depending on the donor density of the material. Considering this, it seems reasonable to produce materials with crystallite sizes roughly in the same size regime for photocatalytic applications. Lower crystallite sizes would hinder the formation of a defined space charge layer, whereas larger crystallites would suffer from increased recombination in the bulk volume where no band bending occurs. Nevertheless, nanostructuring of photocatalysts has often been discussed as a means to improve photocatalytic activity^[46], and several techniques have been proposed^[46] to improve charge carrier separation, especially

in cases where the formation of a defined space charge layer is hindered. For example, beneficial effects of gradient doping^[47], surface deposited co-catalysts^[48,49] or multiphase heterojunctions^[50] on charge separation have been demonstrated. Some attempts to improve charge separation through external influences have been made as well, *i.e.* Gao *et al.* investigated the influence of the Lorentz force caused by a magnetic field on agitated semiconductor particles.^[51]

2.3.1 (Nano-)structuring of photocatalysts

Contrary to the situation in conventional thermal catalysis, an increase of the catalyst surface does not necessarily lead to an increase of activity in photocatalysis. Since recombination occurs at crystal defects (the surface of a crystallite can be considered as its largest defect), a large share of the excited charge carriers undergoes recombination at surface trapping states. Nevertheless, there are also arguments in favor of nanostructured photocatalysts. For example, the charge carrier diffusion pathways to the surface are kept very short, decreasing the probability for bulk recombination. The charge carriers are able to reach the reaction sites at the surface, even if the material is weakly conducting and the mean free path of the excited charge carriers is consequentially short. Besides the surface-to-volume ratio, the nature of the exposed crystal facets also influences photocatalytic activity. The synthesis of materials with preferentially orientated surfaces and selective modification of individual crystal facets have therefore gained growing attention in recent years^[52,53]. Additional to the shortening of the charge carrier diffusion lengths, nanostructuring can be employed as a means of band gap engineering. The electronic dispersion of the bands is decreased in very small particles, causing a widening of the band gap, since fewer orbitals are contributing to the VB and CB (See Figure 3, chapter 2.2). This so-called quantum confinement effect leads to a widening of the band gap. Quantum confinement has for example been reported for TiO₂ particles smaller than 2.1 nm.^[54] Because of the large variety of structure related effects, it is typically not trivial to predict whether nanostructuring has a beneficial or adverse effect on the photocatalytic activity. Recent studies suggest, that the positive and negative effects have to be carefully balanced out and that the best performing morphology for a specific material can often only be determined experimentally, due to the inadequacy of the available theoretical models.^[55,56]

2.3.2 Co-catalysts

Many semiconductors that have been considered for an application in photocatalysis or photoelectrochemistry exhibit an insufficient catalytic or electrocatalytic activity to facilitate the RedOx processes associated with hydrogen evolution.^[57] In such cases, co-catalysts are employed to decrease the overpotentials required for the target reaction. Besides having a purely electrocatalytic effect, co-catalysts can also promote the formation of an internal electric field, due to the formation of a Schottky-contact facilitating the accumulation of charge carriers (Figure 8).

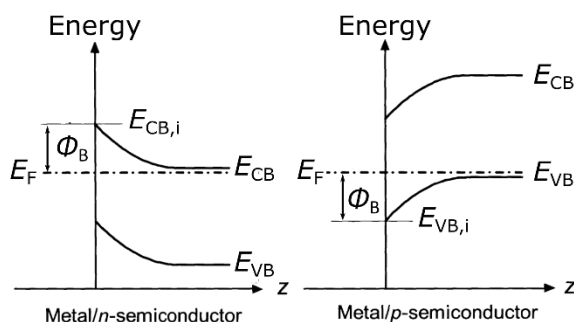


Figure 8: Schematic depiction of the band bending that occurs at a semiconductor-metal interface due to Fermi level equilibration at the Schottky-contact. Φ_B is the Schottky barrier height and $E_{VB,i}$ and $E_{CB,i}$ are the valence and conduction band energy at the metal-semiconductor interface, respectively (Image adapted from [58]).

Commonly noble metals like Pt or Rh are employed as co-catalysts for reductive tasks, while noble metal oxides like IrO_2 and RuO_2 are known to promote the transfer of holes for oxygen evolution.^[59–62] For overall water splitting, Rh- CrO_x core-shell structures have been demonstrated to be very efficient, since the thermodynamically favored oxyhydrogen back reaction on the Rh surface can be effectively suppressed by the chromium oxide layer.^[63] Since inexpensiveness and availability for large scale applications are important criteria for photocatalysts, noble metal free co-catalysts have also been developed to facilitate both hole and electron transfer.^[62]

2.3.3 Heterojunctions

By combining two or more semiconductors, the absorption characteristics and band potentials of the individual materials can be utilized. A semiconductor-semiconductor heterojunction is formed, when both materials are in close phase contact. Unequal band potentials provide a thermodynamic driving force for the separation of excited charge carriers onto the individual semiconductors (Figure 9).

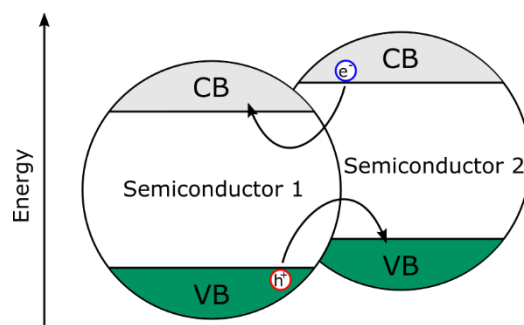


Figure 9: Scheme depicting the separation of excited charges at the heterojunction between two different semiconductors in a composite material.

Additionally, charge carrier migration is facilitated by the internal electric field that is generated at the interface, due to fermi level equilibration.^[64] Considerable increases in performance have been reported for heterojunctions consisting of different crystal morphologies of the same material (e.g. combinations of different TiO₂ modifications^[65]), as well as for composites comprising semiconductors with fundamentally different elemental compositions and absorption characteristics.^[66]

2.3.4 Sacrificial agents

Both a reductive and an oxidative half-reaction must be facilitated by a photocatalyst to regain its ground state after excitation. Since the conversion of a target reactant often involves only one of the half-reactions, appropriate sacrificial agents have to be employed. Sacrificial agents are hole scavengers or electron scavengers that perform the opposing half-reaction to the conversion of the target reactant. Their presence ensures that the photocatalyst maintains charge neutrality during the photocatalytic process. In overall water splitting for example, the oxidation half-reaction proves kinetically very challenging, as described before. Since hydrogen is usually the target product, the oxidation of water can be circumvented by the addition of a sacrificial agent with a more favorable oxidation potential (usually a short-chained alcohol). In this case, the term photoreformation is commonly used. For example, methanol is well-known to be easily reduced by holes in the VB of most common semiconductors and has been excessively studied regarding its potential as sacrificial agent in photocatalysis.^[67] Upon oxidation, the alcohol is intermediately converted to an α -hydroxy alkyl radical. Due to its instability the radical undergoes consecutive reactions, like the injection of the unpaired electron into the CB of the semiconductor (photocurrent doubling), or other reductive tasks.^[68] In the process, the alkyl radical is converted to a carbonyl compound or a carboxylic acid, which can again react as a hole scavenger, increasing the atom efficiency of the reaction. Even if photoreformation is often discussed in relation with water splitting (the technique is also denoted “water half-splitting” in some publications^[69,70]), it must be kept in mind that molecular hydrogen is

generated only from the sacrificial electron donor (when present), as was confirmed by experiments with deuterated agents.^[71] A carbon containing compound must therefore be ultimately consumed, forming CO₂ as a waste product. Since methanol is produced from syngas on a technical scale, its photocatalytic reformation cannot be considered a renewable process and therefore it currently provides no viable alternative for the production of green hydrogen. Nevertheless, the application of hole scavengers often cannot be avoided in the case of visible light absorbing photocatalysts with a suitable CB potential for the reduction of protons, since the smaller band gap compared to UV absorbing semiconductors precludes the necessary overpotential for water oxidation. For that reason, it has been proposed to couple hydrogen evolution with the oxidative photocatalytic degradation of organic pollutants or biomass derived compounds, to avoid the consumption of alcohols or other fossil fuel derived compounds.^[67] Such processes would however still produce CO₂ as a waste product, underlining the necessity for the development of visible light absorbing photocatalysts with custom-tailored band potentials to facilitate overall water splitting in the absence of a sacrificial agent.

2.4 Semiconducting materials in heterogeneous photocatalysis

A huge variety of inorganic solids, showing both *n*-type and *p*-type behavior, have been considered promising photocatalysts.^[39,72,73] The electronic energies of their VBM and CBM are usually defined by the presence of a nonmetal anion and a transition metal cation with either d⁰ or d¹⁰ electronic configuration. Elements belonging to the alkali- or earth alkali metals usually serve only crystal structure defining purposes (Figure 10).^[73]

1	2	3	4	5	6	7	8	9	10	11	12	13	14	15	16	17	18
H																	He
Li	Be											B	C	N	O	F	Ne
Na	Mg											Al	Si	P	S	Cl	Ar
K	Ca	Sc	Ti	V	Cr	Mn	Fe	Co	Ni	Cu	Zn	Ga	Ge	As	Se	Br	Kr
Rb	Sr	Y	Zr	Nb	Mo	Tc	Ru	Rh	Pd	Ag	Cd	In	Sn	Sb	Te	I	Xe
Cs	Ba	La	Hf	Ta	W	Re	Os	Ir	Pt	Au	Hg	Tl	Pb	Bi	Po	At	Rn
Ce Pr Nd Pm Sm Eu Gd Tb Dy Ho Er Tm Yb Lu																	
i)  : d ⁰ ion		} to construct crystal structure and energy structure															
 : d ¹⁰ ion																	
 : Non-metal																	
ii) 		} to construct crystal structure but not energy structure															
iii) 																	
iv) 																	

Figure 10: The role of specific elements in the composition of semiconductor photocatalysts (Image taken from [73]).

A large selection of representative semiconductors is depicted in Figure 11. Notably, compounds comprising a transition metal cation with d^5 electron configuration (e.g. α - Fe_3O_4 , ZnMn_2O_4 , MgFe_2O_4 or CaFe_2O_4) have been recognized as potential candidates, additional to the systematic selection proposed by Kudo *et al.*^[73]

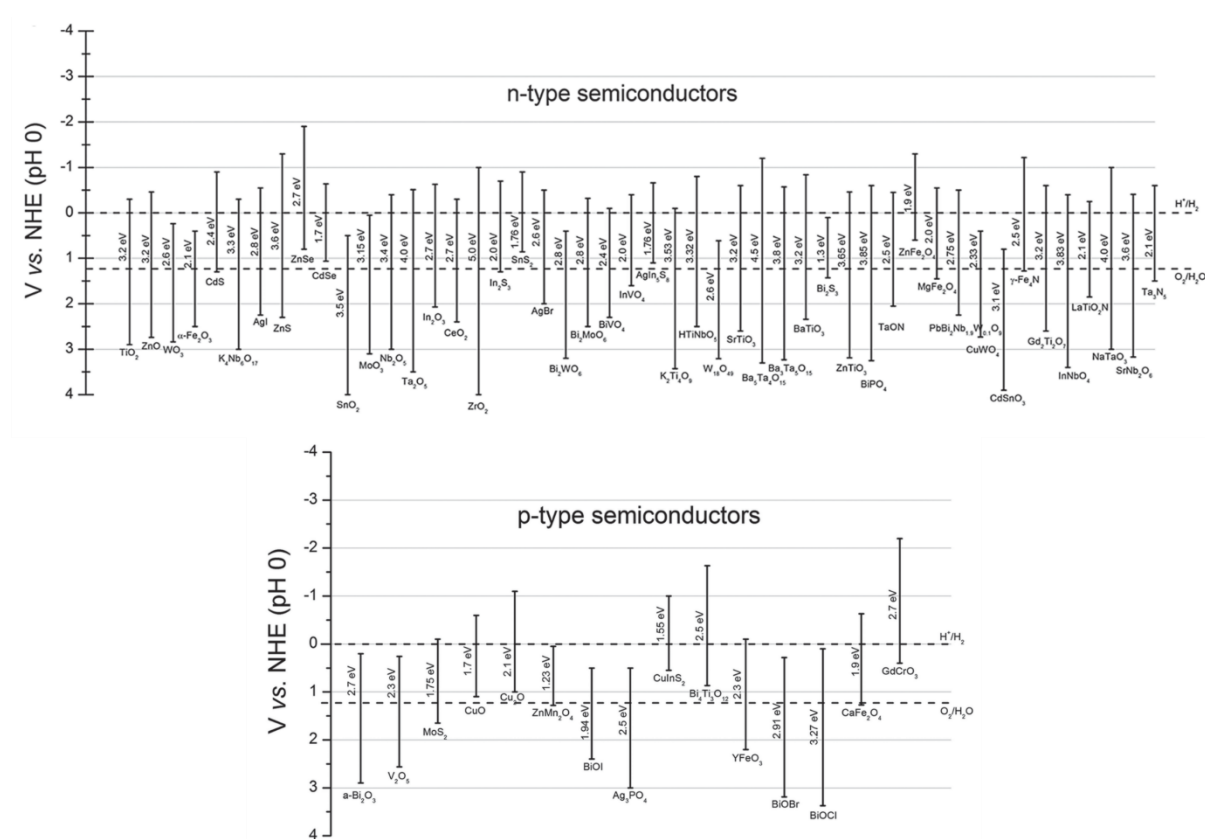


Figure 11: Band positions and band gaps of semiconductors considered for photocatalysis (Image taken from [50]).

The overall scope of investigated materials is even larger today, e.g. graphitic carbon nitride has received tremendous attention over the last years due to its absorption of visible light and very cathodic CBM.^[74] The elemental composition of newly proposed materials tends to get more complex, since many of the currently available materials do not fulfill at least one of the requirements laid out in the introductory chapter. The largest share among the investigated semiconductors is made up by oxides with band gaps larger than 3 eV, which makes them unsuitable for an efficient utilization of visible light. Binary oxides with smaller band gaps, like WO_3 or α - Fe_2O_3 are promising regarding earth abundance and absorption characteristics, yet their applicability in photocatalysis is limited due to low-lying CBM located considerably more anodic than the reversible hydrogen electrode (RHE) potential, thus preventing proton reduction. Replacement of the oxygen anion by sulfur or nitrogen usually leads to a cathodic shift of the VBM and consequently smaller band gaps. For example, sulfides, oxysulfides,

nitrides or oxynitrides provide reasonable absorption of visible light. Yet in many cases, the advantage of the smaller band gap is accompanied by specific shortcomings, *e.g.* stability problems. Sulfur containing photocatalysts for example are susceptible to self-oxidation and can therefore not be used without a hole scavenger, which makes them unsuitable for overall water splitting. Research to overcome this essential drawback is ongoing and just recently Wang et al. claimed the synthesis and application of a stable, visible light absorbing oxysulfide for water splitting.^[75] The development of this material class is however not yet at a stage, where it can be considered a viable alternative to oxides in overall water splitting. Among the materials shown in Figure 11, ferrites with the molecular formula AFe_2O_4 stand out among the oxides having a low band gap in the range of 2 eV as well as fitting band positions to consider them as candidates for photocatalytic overall water splitting under visible light.

2.5 Ferrites in photocatalysis

Ferrites are a class of oxides that contains Fe^{3+} and at least one more transition metal in the form of a divalent cation. Many of the known ferrites have the general molecular formula AFe_2O_4 ($A = Ca^{2+}, Cd^{2+}, Co^{2+}, Cu^{2+}, Fe^{2+}, Mg^{2+}, Mn^{2+}, Ni^{2+}, Zn^{2+}$ and more) and a crystal structure isomorphous to that of the mineral spinel ($MgAl_2O_4$) under ambient conditions, which is why they are commonly called spinel ferrites. However, ferrites with a different unit cell geometry or general formula (*e.g.* garnet ferrites, magnetoplumbite ferrites or orthoferrites) are also known and have been considered for application as photocatalysts.^[18] The bulk crystal structure of some typical ferrites is given in Table 1.

Table 1: Ionic radii of divalent cations found in common ferrites. Values are given both for tetrahedral and octahedral coordination of the metal cation.

A^{2+} Ion	Ionic radius (tetrahedral/octahedral) ^[76] / pm	bulk crystal structure
Ca^{2+}	- / 112	orthorhombic ^[22]
Cd^{2+}	78 / 110	regular spinel ^[77]
Co^{2+}	58 / 90	inverse spinel ^[78]
Cu^{2+}	57 / -	Inverse spinel ^[79]
Fe^{2+}	63 / 92	inverse spinel ^[80]
Mg^{2+}	57 / 89	partially inverse spinel ^[81]
Mn^{2+}	66 / 96	partially inverse spinel ^[82]
Ni^{2+}	55 / -	inverse spinel ^[78]
Zn^{2+}	60 / 90	regular spinel ^[83]

The cubic spinel structure comprises eight formula units per unit cell and can be described as a face centered cubic (fcc) packing of oxygen anions with the metal cations occupying the tetrahedral and octahedral interstitial sites. The size of the interstitial sites allows the incorporation of a wide variety of cations, and varying distributions among the octahedral and tetrahedral sites of the oxygen lattice have been observed. Depending on the charge of the ion on the respective site, a differentiation between regular and inverse spinels is made. In regular spinels the divalent ions occupy 1/8 of the tetrahedral sites and the trivalent ions (Fe^{3+} in the case of spinel ferrites) occupy half of the octahedral sites. When the divalent ions are located exclusively on octahedral sites, the spinel is denoted inverse. In this case 1/8 of the tetrahedral sites are occupied by trivalent ions and the octahedral sites are occupied to 1/4 with divalent- and trivalent ions each. Besides regular and inverse spinels, also partially inverse structures are known, *e.g.* for MgFe_2O_4 . To take cation inversion into account, the molecular formulae of spinel ferrites are commonly denoted as $(\text{A}_{1-\lambda}\text{Fe}_\lambda)_T(\text{A}_\lambda\text{Fe}_{2-\lambda})_O\text{O}_4$, where T and O represent the tetrahedral and octahedral sites respectively and λ is the degree of inversion. The degree of inversion in spinel ferrites depends on the ratio of the cation radii, but also on ligand field stabilization effects, which occur due the partially filled d -orbitals of the constituting transition metal cations. Ferrites are stable in neutral and alkaline aqueous media. In acidic environments however corrosion has been reported.^[84] Apart from this drawback regarding the resistance towards acids, ferrites possess promising characteristics to meet the requirements for an efficient photocatalyst. In recent years, they have attracted growing interest regarding large scale application, due to their elemental abundance^[21] and favorable absorption of visible light. A variety of syntheses and potential photocatalytic applications (including hydrogen reformation) have already been published. The respective works are summarized in available review articles and book chapters.^[18,19,85,86] In many cases, the achieved efficiencies were however considerably lower than the theoretical maximum. Satisfactory explanations for the low activity of ferrites and strategies to improve their photocatalytic performance are still sought after. Since the focus of this work was laid on the investigation of MgFe_2O_4 and CaFe_2O_4 , the characteristics of those materials are described more closely in the following chapters.

2.5.1 Magnesium ferrite – MgFe_2O_4

The application of MgFe_2O_4 for photocatalytic hydrogen evolution was already reported.^[87–89] However, the number of publications where single phase MgFe_2O_4 was used for hydrogen generation is very limited. Reports about photocatalytic degradation of organic compounds using MgFe_2O_4 comprise rhodamine B^[90], methylene blue^[91], tetracycline^[92], acetic acid^[93] and other dyes^[94,95]. The relatively small number of publications on the photocatalytic application of single-phase MgFe_2O_4 is surprising, since the reported band gaps and band potentials suggest that MgFe_2O_4 should be

well-suited for many photocatalytic reactions, including hydrogen reformation (Table 2). Notably however, both *n*-type and *p*-type semiconducting behavior have been determined, and the reported band gaps and especially the absolute band potentials exhibit a vast dissent. Furthermore, the claimed hydrogen evolution rates can be considered doubtful in some cases.^[87,88]

Table 2: Band gaps and band positions of MgFe₂O₄ according to literature examples.

Reference	E_g / eV	E_{VBM} vs. RHE / V	E_{CBM} vs. RHE / V	Way of determination
Benko <i>et al.</i> ^[96]	2.18	+2.38	+0.20	Electrochemical, UV-Vis
Zazoua <i>et al.</i> ^[88]	1.74	-0.38	-2.12	Electrochemical, UV-Vis
Kim <i>et al.</i> ^[87]	2.0	+1.38	-0.62	Electrochemical, UV-Vis
Kirchberg <i>et al.</i> ^[90]	2.43	—	—	UV-vis
Henning <i>et al.</i> ^[97]	—	—	+0.67	Electrochemical
Köferstein <i>et al.</i> ^[98]	2.16–2.38	—	—	UV-Vis
Ulpe <i>et al.</i> ^[44]	3.45–3.57	—	—	Calculated (DDSCH)

A variety of syntheses yielding nanostructured MgFe₂O₄ is known, including co-precipitation^[99], Sol-gel^[100] and mechanochemical routes^[81], electrospinning^[92], templated hydrothermal synthesis^[101] and polymerized complex methods^[89]. In 2002, Sun *et al.* developed a synthesis for Fe₃O₄ nanoparticles with diameters below 20 nm, based on the condensation of iron(III) acetylacetonate in a high-boiling organic solvent.^[102] Later, they demonstrated that the procedure can easily be adapted for the synthesis of various other spinel ferrites.^[103] Based on those works, Kirchberg *et al.* reported a synthesis route for size-uniform MgFe₂O₄ nanoparticles through microwave heating of the respective acetylacetonates in 1-phenylethanol. The work also included surface modification techniques for the long-term colloidal stabilization both in polar and non-polar media.^[90] The particles seemed phase-pure from the given diffraction- and spectroscopic data, however the formation of hematite was observed, when the particles were calcined in an oxygen containing atmosphere, indicating that the presence of an iron oxide by-phase was likely. Furthermore, photocatalytic test reactions were limited to the degradation of organic pollutants and consequentially, the ability of the material to evolve hydrogen was not investigated. The respective synthesis by Kirchberg *et al.* was therefore chosen as the starting point for further optimization in the context of this work, with the aim to synthesize truly phase-pure MgFe₂O₄ nanoparticles for a robust characterization of their photocatalytic abilities.

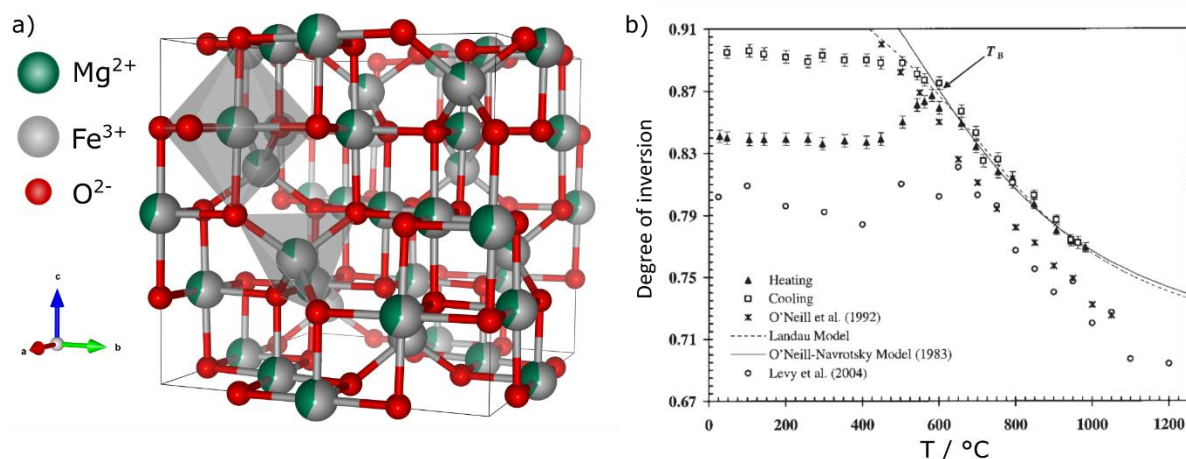


Figure 12: a) Cubic spinel crystal structure of MgFe_2O_4 with a degree of inversion of $\lambda=0.84$. The occupation of the respective lattice sites is illustrated by the pie chart coloring. The unit cell is marked by black lines. b) Changes of the degree of inversion observed for bulk MgFe_2O_4 at elevated temperatures (Image taken from [23]).

MgFe_2O_4 crystallizes in a partially inverse cubic spinel structure (Space group 227, $Fd\bar{3}m$) with a lattice constant of 8.40 Å (Figure 12a).^[23] The degree of inversion has been reported to be dependent on the synthesis conditions and on the thermal history of the sample. Using *in-situ* synchrotron powder X-ray diffraction (PXRD, Figure 12b), Antao *et al.* systematically investigated temperature induced changes of the degree of inversion for a solid-state reaction (SSR) derived MgFe_2O_4 sample.^[23] Notably, starting from $\lambda=0.84$, the degree of inversion reaches a maximum of 0.86 at 601 °C in the heating branch. Further temperature increase leads to a decrease of λ towards a nearly random ($\lambda=0.67$) distribution of cations at temperatures above 1000 °C. Subsequent cooling of the sample leads to an increase of λ , until it reaches 0.90, exceeding the maximum observed in the heating branch. Below 500 °C, the degree of inversion remains constant since the activation barrier for cation ordering cannot be overcome. For MgFe_2O_4 nanoparticles obtained from low temperature syntheses a random distribution of the cations over the available interstitial sites has been reported.^[104] The reported values suggest, that the inversion degree of MgFe_2O_4 can be tuned in a window of $0.67 < \lambda < 0.90$. For syntheses that produces a product with a random cation distribution, considerable changes of the degree of inversion should already be observable after post-synthetic calcination at temperatures above 500 °C. The adjustment of the degree of inversion likely has an impact on the electronic valence structure. Cation inversion related changes of the optical band gap were however not reported yet and Granone *et al.* recently stated that the effect on the electronic structure mainly influences intra-atomic crystal field transitions occurring in the NIR regime, in the case of ZnFe_2O_4 .^[43]

2.5.2 Calcium ferrite – CaFe_2O_4

Considerations regarding the application of CaFe_2O_4 in photoelectrochemistry date back to 1987, when Matsumoto *et al.* investigated the suitability of CaFe_2O_4 as a photocathode for hydrogen production under illumination with a 500 W Xe lamp.^[105] In 1994 they could demonstrate the reduction of dissolved CO_2 by irradiation of an aqueous suspension of CaFe_2O_4 using a 500 W ultra-high pressure Hg lamp.^[106] Particulate photocatalytic hydrogen evolution from an aqueous suspension of single phase CaFe_2O_4 was only reported by one research group.^[87] Notably, hydrogen evolution from phase-pure MgFe_2O_4 was reported in the very same publication. In the respective work, visible light ($\lambda \geq 420$ nm) was used to produce hydrogen from a methanolic solution containing CaFe_2O_4 , which was synthesized by SSR. In a later publication the authors compared the activity of the SSR-derived product with that of CaFe_2O_4 prepared by other synthesis routes.^[107] Compared to MgFe_2O_4 , the band gaps and band potentials found in the literature for CaFe_2O_4 are more homogeneous. A *p*-type semiconductor behavior and a CMB between -0.6 and -0.7 V vs. RHE have been reported, suggesting that the material is suitable for hydrogen reformation.^[106,108] With reported band gaps in the range of 1.8–1.9 eV the absorption characteristics are similar to those of MgFe_2O_4 and consequently the material is able to absorb light from a large fraction of the visible spectrum.^[87,105,109]

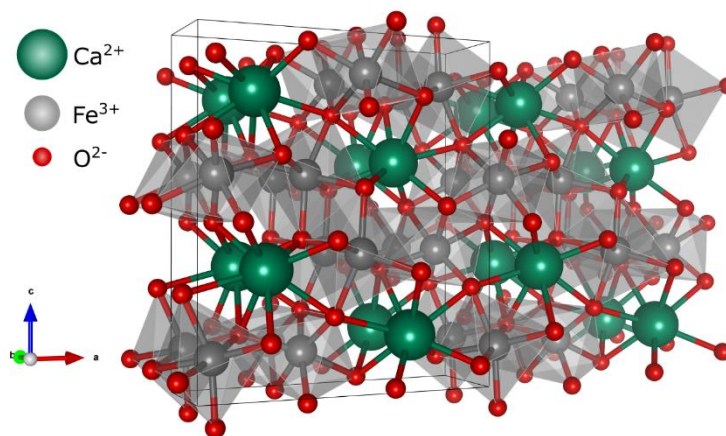


Figure 13: Orthorhombic crystal structure of CaFe_2O_4 .^[110] The unit cell is marked by black lines.

CaFe_2O_4 ferrite stands out from the other ferrites with the same basic molecular formula, as it does not crystallize in the cubic spinel structure, but instead forms orthorhombic crystals. One reason for that is the ionic radius of Ca^{2+} , which is larger than that of the cations found in typical spinel ferrites (Table 1). Hidayat *et al.* proposed that Ca^{2+} is too large to occupy the interstitial sites of the fcc oxygen lattice, preventing the crystallization of CaFe_2O_4 in a cubic spinel structure. Their thermodynamic calculations suggest that only a small fraction of Ca^{2+} is soluble in Fe_3O_4 under retention of the cubic unit cell.^[111] When the Ca^{2+} concentration is increased to meet the stoichiometry of CaFe_2O_4 , the unit cell is stretched and consequently CaFe_2O_4 crystallizes in an orthorhombic structure, where iron is in

six-fold coordination by oxygen arranged in distorted octahedra and Ca^{2+} is in eight-fold coordination (Figure 13).^[22] The unit cell parameters have been determined by Rietveld refinement of synchrotron diffraction data to be $a=9.23 \text{ \AA}$, $b=3.02 \text{ \AA}$ and $c=10.70 \text{ \AA}$. Some reports claim the synthesis of a metastable cubic spinel phase of CaFe_2O_4 .^[112–114] The respective materials were synthesized by sol-gel approaches and the diffraction pattern of the as-synthesized samples suggested the presence of a spinel phase. Upon treatment at temperatures of $\geq 1000^\circ\text{C}$, a conversion to an orthorhombic structure was observed. The respective publications however lack proof that the observation of a spinel structure does not originate from the presence of nanocrystalline Fe_3O_4 , which exhibits a similar diffraction behavior and is a common by-product in this type of ferrite-synthesis.

The orthorhombic unit cell and the complex phase diagram of the Ca-Fe-O system^[111,115] result in an increased synthetic demand compared to ferrites with spinel structure. Typical syntheses producing phase-pure orthorhombic CaFe_2O_4 are performed under SSR conditions requiring calcination temperatures above 1000°C for several hours. As a result, such syntheses yield sintered structures with crystallite sizes of several μm .^[116] Nevertheless, some synthesis routes for nanostructured CaFe_2O_4 have been presented, for example by a mechanochemical approach^[81], solution-combustion synthesis^[117], polymerized complex route^[107], self-propagating combustion synthesis^[107] or electrospinning^[118,119]. Reports about nanostructured CaFe_2O_4 photoelectrodes are scarce, due to the challenging synthesis. However recently some achievements were made. For example, Kirchberg *et al.* were able to prepare mesostructured CaFe_2O_4 electrodes by an evaporation induced self-assembly process followed by short calcination at 700°C . The resulting electrodes exhibited a hierarchical pore structure and generated photocurrent densities of up to $63 \mu\text{A cm}^{-2}$ upon irradiation with visible light.^[120]

2.6 The issue of phase purity

The presence of additional crystal phases can have a significant effect on the electronic structure and the photocatalytic performance of a material, due to the formation of heterojunctions (see chapter 2.3.3). The effect benefits photocatalytic activity in many cases, since the absorption spectrum can be extended and internal electric fields in the vicinity of the heterojunction facilitate the separation of excited charge carriers. For a robust assessment of the photocatalytic performance of a single-phase material it is therefore crucial to exclude the presence of impurities. Taking a closer look on reports about the application of ferrites in photocatalysis, it is conspicuous that the employed materials often exhibit a mixed cation composition or contain at least one other crystal phase.^[18,86] To allow a robust

assessment of the suitability of the single-phase, the syntheses and characterization protocols used in this work were optimized to ensure phase-purity. For nanostructured spinel ferrites, the identification of by-phases is often not trivial, since PXRD and other diffraction based techniques in many cases prove insufficient to exclude the presence of Fe_3O_4 (magnetite) or $\gamma\text{-Fe}_2\text{O}_3$ (maghemite), due to their similar diffraction patterns.^[121] Excluding the presence of these by-phases using Raman spectroscopy proves just as difficult for samples with a low crystallinity, due to the weak signal intensities. The inadequacies of those standard characterization techniques are the reason for some misinterpretations of characterization data that can be found in the literature regarding ferrites. One way to prove the phase purity of a nanocrystalline material is calcination, provided the respective crystal phase has sufficient thermal stability. Due to sintering effects, crystallites exhibit a growth at elevated temperatures and consequentially the Bragg reflections become narrower, which may lead to a separation of reflections originating from different crystal phases. Furthermore, hematite is formed at temperatures above 400 °C in air, when either Fe_3O_4 or $\gamma\text{-Fe}_2\text{O}_3$ are present additional to the ferrite.^[122] MgFe_2O_4 has been reported to be very temperature stable at ambient pressures, as no phase transitions are reported below its melting point located at roughly 1700 °C.^[123] Therefore, when no hematite is formed upon calcination, it can be concluded that the as-synthesized sample was phase-pure as well. Besides calcination studies, quantitative elemental analysis can also give a hint to the presence of impurities in ferrites. In liquid based syntheses like co-precipitation, sol-gel routes or hydro- and solvothermal reactions it is possible, that the A cation is not, or not fully incorporated into the crystal lattice. A solid solution of the divalent cation in an iron oxide crystal phase can be formed in such a case.^[124,125] An A:Fe cation ratio smaller than 1:2 (as would be expected for an ideal AFe_2O_4 structure) consequentially indicates the presence of an iron oxide by-phase.

2.7 The electronic structure of ferrites

The electronic structure of ferrites was excessively discussed by Ulpe *et al.* who recently reviewed both experimental and theoretical results from the literature.^[44] Furthermore, they developed own models for the calculation of electronic band gaps and absolute band potentials in ferrites, with a focus on ZnFe_2O_4 . The authors acknowledged the great dissent both among the values reported in the literature as well as among their own calculations. While they did not include CaFe_2O_4 into their discussion, they reported experimental band gaps in the range of 1.85–2.43 eV and a calculated band gap of 3.45–3.57 eV (depending on the cation ordering; values calculated using dielectric dependent self-consistent hybrid functionals) for MgFe_2O_4 . The calculated band gap is considerably larger than those determined experimentally. Furthermore, it is also larger than fundamental electronic band gaps of other ferrites (calculated by generalized gradient approximation or hybrid density functional theory

models), which in many cases suggested very small band gaps of 1 eV and less. Only in few cases, the calculated band gaps were in good accordance with those observed experimentally. The influence of oxygen vacancies was identified as a possible explanation for the discrepancies.^[126] A final satisfactory explanation for the huge dissent among the results could however not be provided. The work by Ulpe *et al.* therefore impressively uncovers essential difficulties in the precise determination of the optical characteristics and electronic structure of ferrites, suggesting a high complexity of the involved electronic states and transitions and calling for a further going experimental characterization using non-conventional techniques. Only then, the applicability of ferrites for solar energy conversion can be robustly assessed.

As already mentioned in chapter 2.4, most photocatalysts comprise transition metals with a d^0 or d^{10} electronic configuration. For example, TiO_2 comprises Ti^{4+} as the only transition metal ion, which has a d^0 electronic configuration. The VBM is therefore constituted by the $\text{O}(2p)$ states while the valence band minimum is constituted by the empty $\text{Ti}(3d)$ band. In semiconductors comprising d^{10} elements like for example ZnO, the $3d$ orbitals are completely filled with electrons and the CBM is therefore constituted by empty s - or p -states.^[73] In the case of ferrites, both occupied and unoccupied $\text{Fe}(3d)$ states are present due to the d^5 electronic configuration of Fe^{3+} . Due to the influence of the coordinating negatively charged oxygen ligands, the energetic degeneracy of the $\text{Fe}(3d)$ electrons is lifted, as explained by crystal field theory. The geometry of the crystal field orbitals is dependent on the coordination sphere around the Fe^{3+} center and due to the small orbital overlap, the corresponding electronic states exhibit a strong localization at the respective transition metal center instead of contributing to the dispersed electron cloud.^[127] In accordance with Hund's rule, the electronic states corresponding to the respective crystal field orbitals are further split into spin up (\uparrow) and spin down (\downarrow) states, due to the exchange splitting that is associated with spin pairing (Figure 14a).^[43,128] For first-row transition metals coordinated by oxygen, the extend of the exchange splitting is usually larger than the crystal field splitting and the metal centers adopt an electronic high-spin configuration as a consequence.^[129]

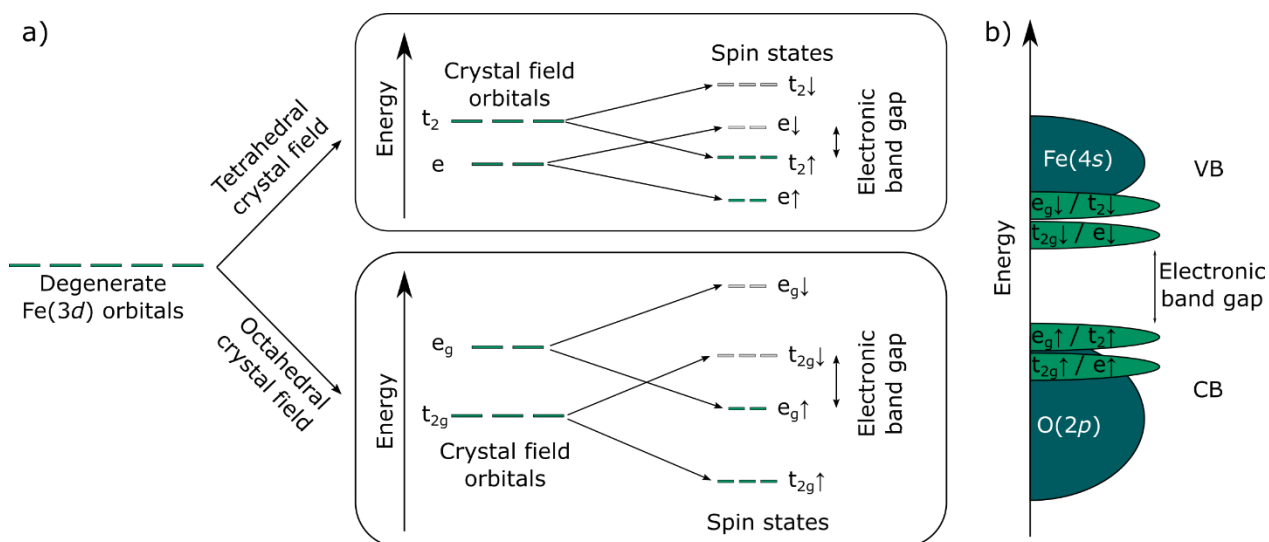


Figure 14: a) Illustration of the crystal field splitting and exchange splitting for Fe(3d) orbitals in tetrahedral and octahedral coordination. The occupation of the available orbitals and states is reflected by the color of the bars (green: occupied; grey: unoccupied), to reflect the electronic high-spin structure of Fe³⁺. Note the differentiation between orbitals (wide bars) and individual electronic states (narrow bars).^[129–131] b) Simplified schematic depiction of the electronic states constituting the fundamental electronic band gap.

As illustrated in Figure 14b, the VBM of ferrites is constituted of Fe($t_{2g}\uparrow$) or Fe($e_g\uparrow$) states depending on the chemical environment of Fe³⁺. Additionally, a significant contribution of O(2p) electron density to the VB is likely, similar to the situation in other iron containing oxides.^[130,132] Taking all this into account, a large variety of electronic states must be considered for a proper interpretation of the optical absorption characteristics of spinel ferrites. In the case of octahedrally coordinated transition metal centers, Tanabe-Sugano diagrams are conventionally used to describe the nature of the respective electronic transitions.^[133] When the Fe³⁺ center is present in tetrahedral and octahedral coordination, like it is the case in the partially inverse spinel MgFe₂O₄, the description of the electronic valence structure becomes however even more complex. A complete and thorough spectroscopic interpretation of the UV-Vis-NIR absorption characteristics of MgFe₂O₄ was therefore not performed yet, to the best of the author's knowledge.

2.8 Magnetic properties of ferrites

Matter can be classified regarding its behavior in a magnetic field. Diamagnetic materials strive to reduce the magnetic flux density inside their volume while paramagnetic materials increase it (Figure 15a). As a consequence, diamagnetic materials experience a force, which is directed towards the point with the lowest magnetic flux density in an inhomogeneous magnetic field, while paramagnetic samples are drawn towards the point with the highest flux density. Whether dia- or paramagnetism is observed, is determined by the electronic structure of the sample. In diamagnetic

materials all orbitals are either empty or occupied by two paired electrons. Their electronic dipole moments are therefore compensated on an atomic level. Paramagnetic materials on the other hand comprise orbitals filled with only one electron. Due to uncompensated electronic spin magnetic moments, a permanent magnetic moment is observed. Depending on the alignment of the magnetic field vectors corresponding to the spin moments, a further classification into paramagnetism, ferromagnetism, antiferromagnetism and ferrimagnetism is made (Figure 15b). In paramagnetic materials the field vectors are oriented in a fashion that compensates for the magnetic moments of the unpaired electrons, in the absence of an external magnetic field. Paramagnetic materials therefore exhibit no permanent magnetization. In ferromagnetic materials, the coupling of spin magnetic moments leads to the formation of magnetic domains. In those domains the field vectors are aligned with parallel orientation. When their direction is similar over the whole sample, a permanent magnetization is observed. Antiferromagnetism and ferrimagnetism describe cases, where the individual magnetic domains are aligned in such a way that the resulting magnetic moment over the whole sample is either zero or reduced compared to a ferromagnetic sample, respectively. The ordering of magnetic domains in a magnetic material is temperature dependent and above a certain temperature the magnetic behavior switches from ferromagnetism or antiferromagnetism to paramagnetism. The temperatures at which the change of magnetic behavior occurs, are called Curie temperature and Néel temperature, respectively.

In the case of magnetic nanoparticles comprising a single magnetic domain, the anisotropy energy of individual particles is very low, allowing them to undergo continuous, thermally activated reorientation, provided that the temperature is high enough. On a large scale such materials behave like a paramagnet and hence the phenomenon is called superparamagnetism.

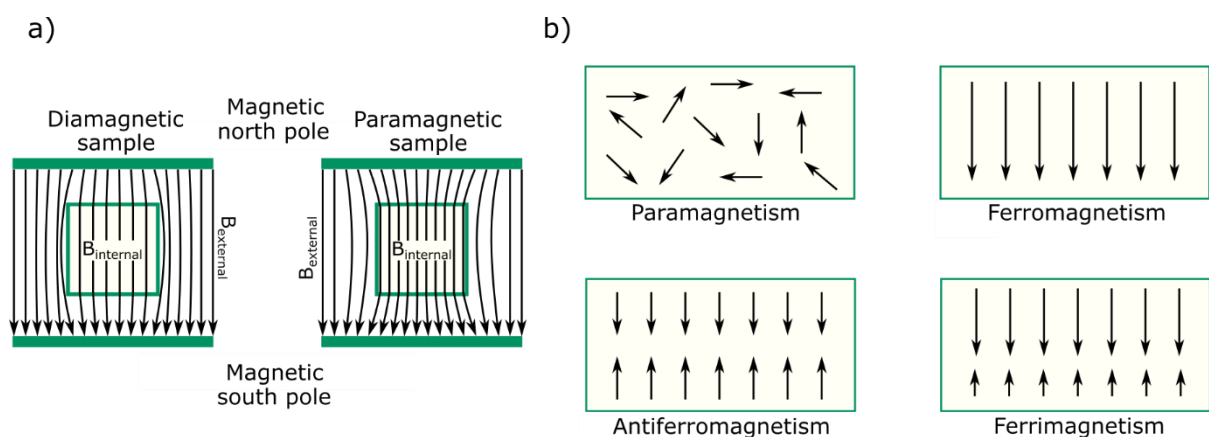


Figure 15: a) Behavior of diamagnetic and paramagnetic matter in a homogeneous magnetic field. b) Schematic illustration of the different types of magnetism in materials with uncompensated electronic spin.^[134]

Due to the presence of Fe^{3+} (and potentially additional divalent A cations with unpaired electronic spin), most ferrites show a response to an externally applied magnetic field. As mentioned before, first row transition metal oxides usually exhibit a high-spin electronic configuration due to the small crystal field splitting energies, resulting in five unpaired electrons in the crystal field orbitals. Ferrites have consequently been considered for a variety of magnetic applications, including ferrofluids^[135], magnetic components in electronics^[136], or as biodegradable agents in medical applications like targeted drug delivery^[25] and magnetic resonance imaging^[26]. Furthermore the magnetism has been reported to be beneficial removal of ferrite catalysts from reaction suspensions.^[137] The most prominent example for the strong magnetism of ferrites is magnetite, which was the first magnetic mineral known to humankind and whose magnetic characteristics are even reflected in its name. Because of the similar crystal structure, MgFe_2O_4 shows comparable magnetic behavior. The magnetic superexchange interactions between Fe^{3+} on tetrahedral and octahedral sites in the crystal lattice is hereby much stronger (roughly by a factor of 10), compared to the one between Fe^{3+} on equivalent crystallographic sites.^[138] Since the magnetic field vectors of Fe^{3+} on tetrahedral and octahedral sites adopt an antiparallel alignment, the saturation magnetization (M_s) is highly dependent on the degree of inversion (Figure 16). Unlike most spinel ferrites, CaFe_2O_4 shows antiferromagnetic behavior and is therefore not suited for magnetic applications.^[139] Regarding the application as a (photo-)catalyst antiferromagnetism can however also be considered an advantage, since interference with reactor components like magnetic stirring equipment can be avoided.

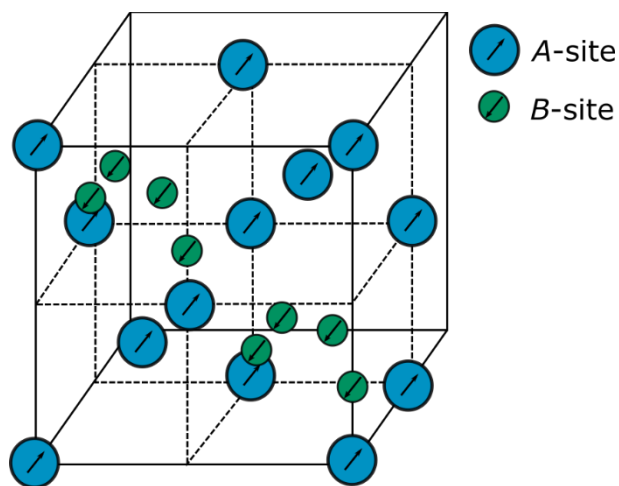


Figure 16: Antiparallel alignment of the spin magnetic moments on A - and B -sites in spinel ferrites. For better clarity, only cations in the front four octants of the unit cell are shown (Image adapted from [140])

2.9 Immobilization of magnetic photocatalysts in mesoporous host networks

Magnetic nanoparticles come with some disadvantages that must be considered for an application in photocatalysis. While their magnetism is advantageous in many cases^[141,142], it can also be unwanted. In suspension reactors, stable dispersions guarantee a uniform illumination of the photocatalyst. Magnetic particles however can get stuck on magnetic stirring equipment or undergo sedimentation because of their tendency to form large agglomerates. Surface modification of the particles can improve the colloidal stability but also may prevent magnetic separation and the surface bound organic compounds might be decomposed under photocatalytic conditions.^[142] As mentioned before, the susceptibility to corrosion in acidic media is a known disadvantage of ferrite nanoparticles, which limits the spectrum of possible applications. Some attempts have been made to conquer such disadvantages by combining magnetic nanoparticles with an inert inorganic material, protecting the surface and limiting interparticular magnetic interactions. For example, core-shell systems consisting of a magnetic ferrite core enclosed in a silica shell were prepared using sol-gel^[143] or microemulsion routes.^[144] It was found that the formation of such composites is facilitated by an effortless binding of silica to the hydroxyl groups on the surface of the ferrite.^[141] Fröba *et al.* were able to immobilize Fe_2O_3 inside a mesoporous MCM-48 SiO_2 host structure, by a wet impregnation method.^[145] They could demonstrate that the iron oxide was located nearly exclusively in the pores, yet lacked crystallinity. Xu *et al.* reported core-shell structures comprising crystalline Fe_3O_4 surrounded by a porous silica shell with a high surface area of $273 \text{ cm}^3 \text{ g}^{-1}$.^[146] Porosity is a prerequisite for the application of such core-shell structures in photocatalysis, since SiO_2 is an electric insulator and the transport of reactants to the active sites on the semiconductor surface must therefore be ensured to allow the transfer of charge carriers. Various mesopore morphologies are accessible through templated condensation of orthosilicates in the presence of surfactants or polymers (Figure 17).

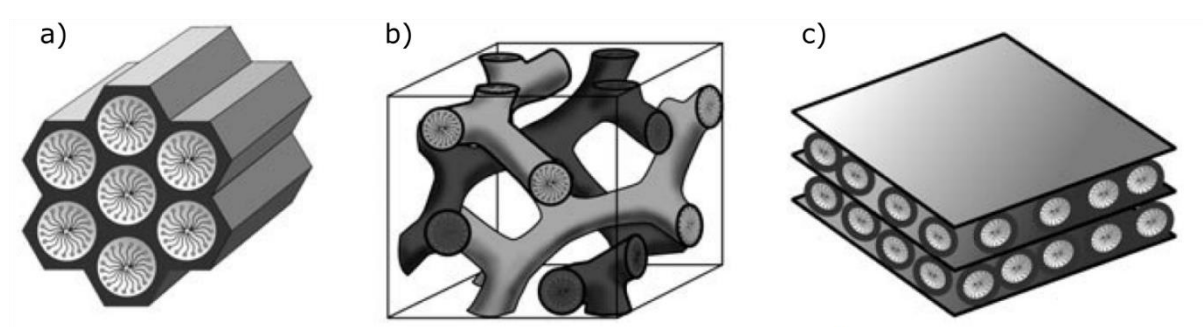


Figure 17: Different types of pore morphologies employed for the mesostructuring of SiO_2 . a) 2D-hexagonal pores (e.g. SBA-15, MCM-41), b) 3D-gyroidal pores (e.g. MCM-48, KIT-6), c) 2D-lamellar pores (e.g. MCM-50). Image taken from [147].

The surface of the SiO₂ host structure can be modified by attaching organic functionalities, *e.g.* via post-synthetic grafting^[148] or by co-condensation during synthesis.^[149] Recently Timm *et al.* developed a post synthetic grafting procedure for the modification of porous silica surfaces with (3-Mercaptopropyl)trimethoxysilane (MPTMS) *via* the gas phase followed by oxidation yielding surface bound sulfonic acid groups.^[150] A very high degree of functionalization could be achieved for porous SBA-15 and KIT-6 structures using this approach. The combination of functional host structures with nanocrystalline photocatalysts could pave the way for the synthesis of multifunctional composites comprising the advantages of different types of catalysis in a single material. Besides SiO₂, other porous structures, like for example periodically mesoporous organosilica (PMO), can also be considered for a combination with ferrite nanoparticles, as they offer comparable chemical stability, high surface areas and the possibility of post synthetic modification with organic functionalities.^[151]

3 Experimental Part

3.1 List of chemicals

All chemicals used in for this work are summarized in Table 3 and were used as received by the supplier, without further purification. For the preparation of aqueous solutions, de-ionized water was used.

Table 3: Summary of all chemicals used for this work.

Compound name	CAS Number	Purity / Concentration	Supplier
Acetone	67-64-1	Technical grade	-
Boron nitride	10043-11-5	98%	Sigma Aldrich
1,4-Butanediol	110-63-4	≥99%	Carl Roth
1-Butanol	71-36-3	99%	Grüssing
Calcium acetate monohydrate	114460-21-8	≥99%	Carl Roth
Cellulose	9004-34-6	Not specified	Sigma Aldrich
2,6-Dichlorophenolindophenol hydrate	1266615-56-8	Not specified	Sigma Aldrich
Diethyl ether	601-29-7	Technical grade	-
Ethanol	64-17-5	>99.9%	VWR
Iron(III) acetylacetonate	14024-18-1	>99%	Acros Organics
Iron(III) nitrate nonahydrate	7782-61-8	>99%	Acros Organics
Iron(III) oxide	1309-37-1	99.999%	Acros Organics
Iron (II,III) oxide	1317-61-9	97%	Sigma Aldrich
Hexachloroplatinic acid hexahydrate	18497-13-7	99.995%	Carl Roth
Hydrochloric acid	7647-01-0	≥37%	Merck
Hydrogen peroxide	7722-84-1	30% w/v	Fisher Scientific
Methanol	67-56-1	99.9%	Fisher Scientific
Magnesium acetylacetonate	14024-56-7	>98 %	TCI
Magnesium acetate tetrahydrate	16674-78-5	≥99%	Sigma Aldrich
Manganese(II) acetylacetonate	14024-58-9	≥97%	Sigma Aldrich
(3-Mercaptopropyl)trimethoxysilane	4420-74-0	95%	Sigma Aldrich
Nickel(II) acetylacetonate	3264-82-2	>98%	Merck
Nitric acid	7697-37-2	65%	Bernd Kraft
Nitrobenzene	98-95-3	99%	Alfa Aesar
<i>n</i> -Pentane	109-66-0	Technical grade	-
1-Phenylethanol (rac.)	98-85-1	98%	Sigma Aldrich
Pluronic® P123	9003-11-6	Not Specified	Sigma Aldrich
Potassium nitrate	7757-79-1	>99%	Acros Organics
Rhodamine B	81-88-9	>95%	TCI
Rhodium chloride	10049-07-7	98%	Sigma Aldrich
Sodium citrate dihydrate	6132-04-3	≥99%	Sigma Aldrich
Sodium hexachlororhodate	14972-70-4	Not Specified	Sigma Aldrich
Sodium sulfate	7757-82-6	≥99%	Carl Roth
Tetraethyl orthosilicate	78-10-4	99%	VWR

3.2 Synthesis of spinel ferrites

For the synthesis of MgFe_2O_4 nanoparticles, a microwave-assisted route by Kirchberg *et al.*, based on the condensation of metal acetylacetonates (acac) in 1-phenylethanol was adapted.^[90] This synthesis was later modified for the incorporation of other divalent cations. For CaFe_2O_4 a new microwave-assisted synthesis pathway was developed.

3.2.1 MgFe_2O_4

The basic steps of the synthesis for MgFe_2O_4 nanoparticles are depicted in Figure 18. For a typical synthesis, 111.3–222.6 mg (0.5–1 mmol, 0–100% stoichiometric excess) of $\text{Mg}(\text{acac})_2$ and 353.3 mg (1 mmol) of $\text{Fe}(\text{acac})_3$ were dissolved in 15 mL of 1-Phenylethanol, with the help of an ultrasonic bath. After complete dissolution, the mixture was put into a sealed borosilicate glass vessel and heated to the target temperature of 200–275 °C under magnetic stirring (600 rpm), using an Anton Paar Monowave 400 laboratory microwave operating at a frequency of 2.45 GHz and set to maximum heating capacity. The temperature was monitored with a built-in IR sensor. After reaching the target temperature, stirring was continued for 30 min and then the solution was quickly cooled down to 55 °C, using compressed air. The obtained suspension was added to 20 mL of *n*-pentane and centrifuged. After decanting the solvent, the particles were washed three times with a mixture of water and acetone (30 mL/5 mL), and once with 25 mL of diethyl ether, with centrifugation and decantation after each washing step. After drying for at least 12 hours at 80 °C and grinding with an agate mortar, brown MgFe_2O_4 powder was obtained. The powder was calcined at 400 °C, 600 °C and 800 °C for 60 min (heating rate: 10 K min^{-1}) to remove organic contaminants, to increase the crystallinity and to induce changes of the degree of inversion.

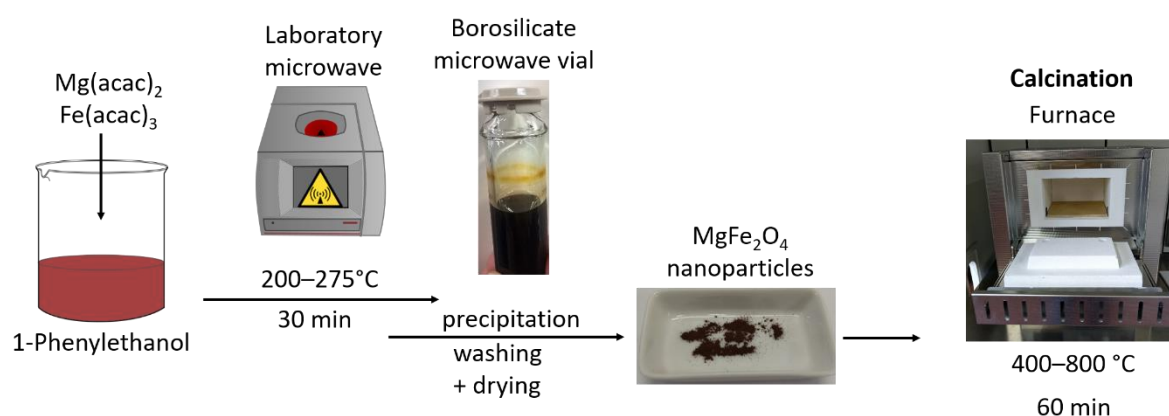


Figure 18: Illustration of the standard synthesis route for spinel ferrite nanoparticles. (Image adapted from *ACS Appl. Nano Mater.* 2020, 3, 11587. Copyright (2020) American Chemical Society.)

3.2.2 NiFe₂O₄

NiFe₂O₄ nanoparticles were synthesized by adaption of the synthesis for MgFe₂O₄ nanoparticles. 128.5 mg (0.5 mmol) of Ni(acac)₂ were hereby employed as Ni²⁺ source. The other reaction conditions and the post synthetic processing were kept equal to the synthesis of MgFe₂O₄.

3.2.3 MnFe₂O₄

For the synthesis for MnFe₂O₄ nanoparticles, the synthesis for MgFe₂O₄ nanoparticles was adapted by employing 126.6 mg (0.5 mmol) of Mn(acac)₂ as Mn²⁺ source. The microwave temperature was set to 250 °C. All other reaction parameters and the post synthetic processing were not altered compared to the synthesis for MgFe₂O₄. Calcination was performed at 400 °C, 600 °C and 800 °C for one hour after reaching the target temperature with a heating rate of 10 K min⁻¹.

3.3 Synthesis of CaFe₂O₄

Macroporous CaFe₂O₄ sponge structures were synthesized by a newly developed microwave assisted route based on the reaction of calcium acetate (OAc) and iron nitrate in 1,4-butanediol followed by calcination at 900 °C. The basic steps of the synthesis are depicted in Figure 19. Similar to the synthesis of MgFe₂O₄, the employed calcium precursor had to be employed in (small) excess to avoid the formation of by-phases after the calcination of the microwave product. In this case, this might however be related to a dissenting amount of crystal water of the employed Ca(OAc)₂·H₂O compared to the data given by the supplier. In a typical synthesis, 96.7 mg (0.55 mmol, 10% stoichiometric excess) of Ca(OAc)₂·H₂O and 404.0 mg (1 mmol) of Fe(NO₃)₃·9 H₂O were dissolved in 15 mL of 1,4-butanediol, using an ultrasonic bath and a laboratory shaker. After complete dissolution, the mixture was put into a sealed borosilicate glass vessel and heated to the target temperature of 300 °C using an Anton Paar Monowave 400 laboratory microwave operating at a frequency of 2.45 GHz and set to maximum heating capacity. The temperature was monitored with a built-in IR sensor. After reaching the target temperature, stirring was continued for 30 min and then the solution was quickly cooled down to 55 °C, using compressed air. The obtained suspension was added to 20 mL of acetone and centrifuged. After decanting the solvent, the product was washed three times with a mixture of water and acetone (30 mL/5 mL), and once with 25 mL of diethylether, with centrifugation and decantation after each step. After drying for at least 12 hours at 80 °C and grinding with an agate mortar, a brown precursor powder was obtained. To convert this powder into macroporous CaFe₂O₄, it was calcined at 900 °C for 60 min (heating rate: 10 K min⁻¹).

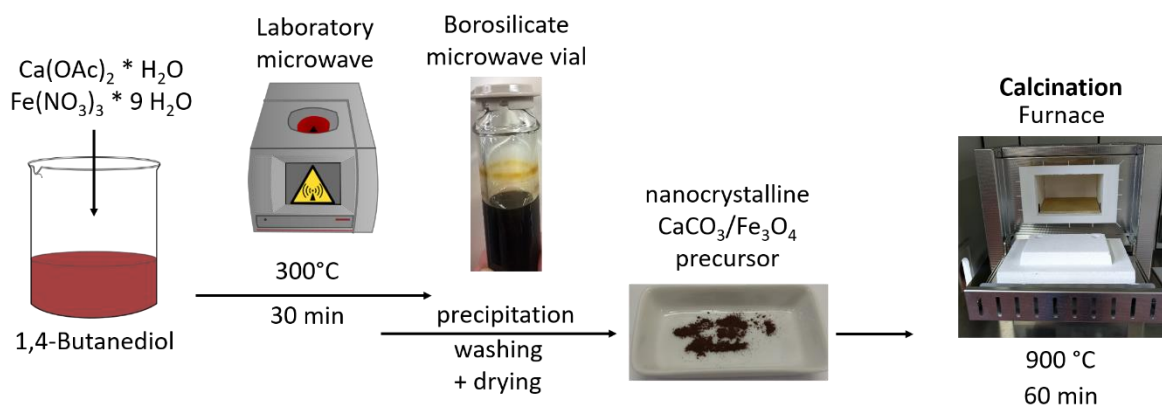


Figure 19: Illustration of the standard synthesis for macroporous CaFe_2O_4 sponges.

3.4 Synthesis of KIT-6 type mesoporous SiO_2

SiO_2 with KIT-6 type *la3d* cubic gyroidal mesopore structure was synthesized according to a procedure described by Kleitz *et al.*^[152] In short, 8.5 g of Pluronic® P123 triblock copolymer were dissolved in a mixture of 240 mL of Ethanol and 20 mL concentrated hydrochloric acid at 40 °C. After complete dissolution (roughly 24 hours), 10 mL of 1-butanol were added. After stirring for one hour at 40 °C, 17 mL of tetraethyl orthosilicate (TEOS) were added *via* syringe under vigorous stirring. Subsequently, the stirring at 40 °C was continued for another 24 hours. The obtained mixture was placed in a sealed autoclave with polytetrafluoroethylene (PTFE) inlet and heated to 100 °C for 60 hours. Afterwards, the white precipitate was filtered off and washed with water and ethanol (three times each) and then refluxed in a mixture of 800 mL of ethanol and 20 mL of concentrated hydrochloric acid for 48 h to remove template residues. The solid was washed with water and ethanol (three times each) and dried at 80 °C for 12 h to obtain a colorless powder.

3.5 Synthesis of $\text{MgFe}_2\text{O}_4@\text{KIT-6 SiO}_2$

For the synthesis of MgFe_2O_4 immobilized in mesoporous SiO_2 , 215 mg of KIT-6 SiO_2 (synthesized by the procedure described in chapter 3.4) were added to a precursor solution containing 194.8 mg (0.875 mmol, 75% stoichiometric excess) of $\text{Mg}(\text{acac})_2$ and 353.3 mg (1 mmol) of $\text{Fe}(\text{acac})_3$ dissolved in 15 mL of 1-Phenylethanol. The mixture was stirred for 72 hours to facilitate the infiltration of the pore system with the precursor solution. The mixture was heated to 250 °C for 30 min in the microwave and then quickly cooled down to 55 °C using compressed air. The obtained suspension was added to 20 mL of *n*-pentane and centrifuged. After washing three times with water/acetone (25 mL/10 mL) and once with 25 mL of diethyl ether (with centrifugation and decantation after each step), the sample was dried at 80 °C for at least 24 hours, to obtain a brown powder.

3.6 Modification of the $\text{MgFe}_2\text{O}_4@\text{KIT-6 SiO}_2$ surface

Sulfonic acid groups were attached to the surface of $\text{MgFe}_2\text{O}_4@\text{KIT-6}$ by adaption of a route developed by Timm *et al.*^[150] Surface modification was performed in two steps. In the first step, thiol groups were grafted to the surface in the gas phase, using a chemical vapor deposition (CVD) related approach. In the second step the thiol moieties were oxidized and protonated to obtain surface-bound sulfonic acid groups. For the grafting of the thiol groups, up to 360 mg of $\text{MgFe}_2\text{O}_4@\text{KIT-6}$ were placed in the PTFE inlet of an autoclave, together with a small PTFE beaker (Figure 20) containing MPTMS (1 mL per 360 mg of SiO_2). The autoclave was flushed with argon for five minutes and then sealed and heated to 120 °C for 48 hours.

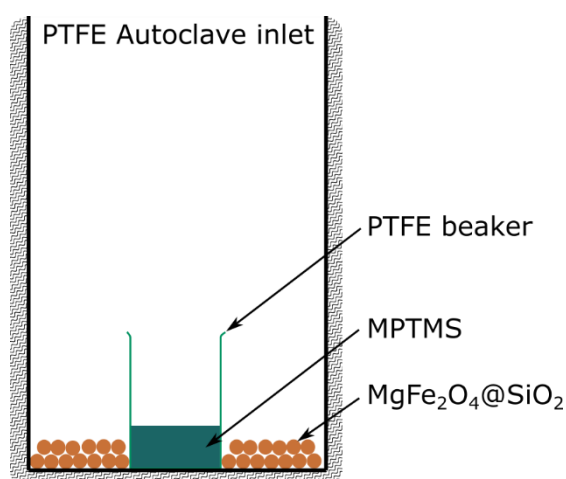


Figure 20: Illustration of the setup that was used for the functionalization of $\text{MgFe}_2\text{O}_4@\text{KIT-6 SiO}_2$ with thiol moieties, in the gas phase.

For the conversion of the thiol groups to sulfonic acid functionalities, 100 mg of the MPTMS functionalized $\text{MgFe}_2\text{O}_4@$ KIT-6 were suspended in 50 mL of 30% aqueous H_2O_2 and shaken for 24 hours at room temperature. Then 400 μL of concentrated nitric acid were added and shaking was continued for six hours. Afterwards the liquid phase was removed by centrifugation and the precipitate was washed once with water and once with ethanol and then dried at 80 °C for at least 24 hours.

3.7 Preparation of ferrite (photo-)electrodes

Ferrite electrodes were prepared by spray coating a fluorine-doped tin oxide (FTO) glass substrate using suspensions of 20-50 mg of freshly ground ferrite powder in 20 mL ethanol (Figure 21). The FTO substrate was mounted at a distance of 12 cm from the nozzle and heated to 250 °C during the spray coating process to allow for a rapid evaporation of the ethanol. The stream of air and suspension was kept constant during the spray coating process and fresh suspension was added to the sprayer in small quantities, to prevent sedimentation of the ferrite inside the sprayer components. Adhesive copper tape was used to cover a fraction of the substrate where it was later connected to the electrical circuit using copper tape and wiring.

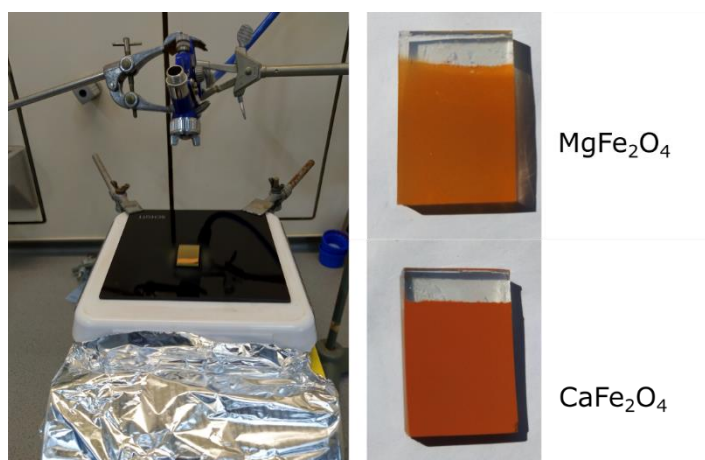


Figure 21: Spray coating setup that was used for the preparation of ferrite films (left) and exemplary MgFe_2O_4 and CaFe_2O_4 films prepared by this procedure (right).

3.8 Characterization techniques and instrumentation

3.8.1 Electron microscopy

Irrespective of the manufacturing quality of its components, the resolution of a microscope is limited by the wavelength of the probing beam due to diffraction phenomena. In case of conventional optical microscopy, which relies on visible light as probe, the maximum achievable resolution is in the range of several hundred nanometers, making the technique inept for the investigation of nanostructures. To display such structures with a satisfactory resolution, probes with a much smaller wavelength must be used. Based on the concept of matter waves that was first proposed by Louis de Broglie, a momentum dependent wavelength can be calculated for subatomic particles. In the case of electrons with a kinetic energy of several keV, the resulting wavelengths are in the range of picometers, making them well-suited even for the investigation of very small structures. Electron microscopy imaging can be performed either in transmission (transmission electron microscopy, TEM), provided the sample is sufficiently thin for the electron beam to pass through, or by scanning the sample with a focused electron beam, while detecting the back-scattered electrons (scanning electron microscopy, SEM). Both types of electron microscopy were used to image the structures produced in the course of this work.

Transmission electron microscopy was performed either with a Philips CM30 transmission electron microscope operated at 300 kV (University of Giessen) or with a JEOL JEM-2200FS energy filtered transmission electron microscope equipped with Schottky field emission gun (operated at 200 kV) and in-column Omega energy filter (University of Bayreuth).

SEM imaging was performed using a Zeiss Merlin field-emission high-resolution SEM (University of Giessen), or a Zeiss LEO 1530 SEM (University of Bayreuth). Measurements were performed with an accelerating voltage of 3 kV and at a working distance of 4–6 mm. For weakly conducting samples, a thin layer of Pt was applied prior to the measurements using a Cressington Sputter Coater 208 HR.

3.8.2 Diffraction based techniques

3.8.2.1 X-ray diffraction

X-ray diffraction (XRD) is a widely used technique for the characterization of crystalline solids. X-rays with wavelengths in the same regime as interatomic distances in chemical compounds are hereby directed onto the sample. If the atomic structure of the sample exhibits a periodicity, the X-ray beam is diffracted by the lattice-like arrangement of atoms. Depending on the distance d between the individual lattice planes, this leads to a beam path difference among X-rays diffracted at different lattice planes and consequently to interference between the diffracted waves. At some angles (usually

given in 2θ , in relation to the incident beam, see Figure 22) the diffracted beam can be observed as a Bragg reflection, while at other angles no diffracted radiation can be detected due to total destructive interference.

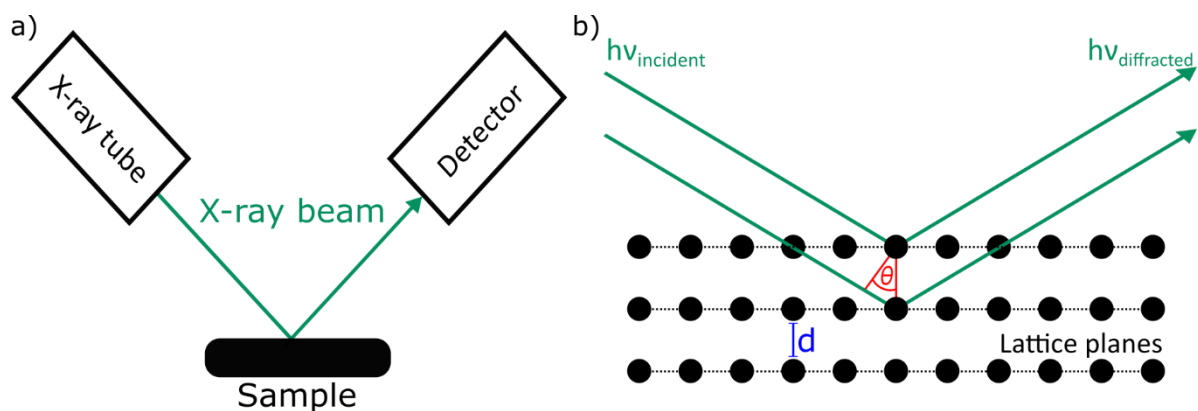


Figure 22: a) Scheme of a conventional powder X-ray diffractometer. b) Scheme illustrating the scattering of an X-ray beam at the lattice planes of a crystal.

In accordance with Bragg's law (Equation 5), the diffracted beam can only be detected at angles where the diffraction is fully constructive. A characteristic pattern for the probed crystal structure can therefore be obtained by scanning different angles.

$$n \cdot \lambda = 2 \cdot d \cdot \sin(\theta) \quad (5)$$

Here, n is a positive integer representing the diffraction order, λ is the wavelength of the employed X-rays, d is the distance between the lattice planes and θ represents the diffraction angle (see Figure 22)

A fundamental differentiation between diffraction experiments conducted on single crystals and on powders is made. While diffraction on single crystals requires crystallites of sufficient size and goes in line with a more demanding sample preparation, it displays the full crystal structure in reciprocal space and can therefore be employed for the determination of unknown crystal structures. PXRD on the other hand offers a quick and facile instrument to determine, whether phases with an already known crystal structure are present in a sample, by comparison with a reference database. Since small crystallites are randomly orientated in powder samples, a ring-shaped diffraction pattern is obtained. It suffices to perform the angle scan in only one dimension, since such a scan captures all information contained in the diffraction pattern (Bragg-Brentano diffractometer geometry). Since literature references for MgFe_2O_4 , CaFe_2O_4 and the common by-phases are available, PXRD provided the convenient means for the characterization of the synthesized materials.

Since the X-ray beam is scattered at the electron-hulls of atoms, X-ray diffraction can also be used to probe ordered porous structures, where the electron density fluctuates between pores and pore walls. Usually specialized small angle X-ray scattering (SAXS) instruments are used, since the respective reflections occur at small diffraction angles. To some degree, it is however also possible to use conventional powder XRD machines for measurements at small angles. Respective measurements are denoted as small angle powder X-ray diffraction (SAPXRD) for better clarity. In this work, SAPXRD was used to confirm the periodicity of MgFe₂O₄@KIT-6 mesoporous composite materials.

PXRD patterns were collected with a PANalytical X'Pert pro diffractometer equipped with a X'Celerator detector (University of Giessen), or a PANalytical EMPYREAN diffractometer equipped with a PixCel 1D detector (University of Bayreuth). In either case, Cu K α irradiation ($\lambda=1.54060$ Å) was used and the X-ray tubes were operated at an accelerating voltage of 40 kV and an emission current of 40 mA. Since Cu K α radiation is able to interact with Fe(1s) electrons and consequently produces diffuse Fe K α fluorescence radiation, the pulse-height discrimination (PHD) values of the detector were set to 8.05 keV and 11.27 keV for the lower and upper level respectively, to reduce the fluorescence background. Depending on the crystallite size of the investigated sample, a step size between 0.03 and 0.08 °2 θ was chosen. The Software X'Pert HighScore V3.0, equipped with a PDF-2 1999 Database was used for data processing and phase identification. Crystallite sizes were approximated from the full width at half maximum (FWHM) of the Bragg reflections using Scherrer's equation (Equation 6), where L is the size of the coherent scattering domain, K is a unit-less factor accounting for the shape of the crystallite, λ denotes the wavelength of the employed X-rays, $\Delta 2\theta$ is the FWHM and θ represents the angle under which the respective Bragg reflection is detected.

$$L = \frac{K \cdot \lambda}{\Delta 2\theta \cdot \cos 2\theta} \quad (6)$$

3.8.2.2 Selected area electron diffraction

Selected area electron diffraction (SAED) is used for the local characterization of crystalline structures. In contrast to PXRD, which requires at least a few milligrams of powder (and therefore numerous crystallites with random orientation), SAED is able to investigate samples on the nanometer scale. Depending on the investigated area and sample preparation, often individual point reflections are visible in the diffraction pattern and even single nanocrystals can be investigated. The technique is based on the diffraction of a parallel, high-energy electron beam with a small diameter and an electron energy that can reach several 100 keV. Electrons in this energy range have a De Broglie wavelength smaller than interatomic distances and diffraction phenomena can therefore be observed. The

diffraction pattern represents the inverse coordinates of lattice planes and therefore their distances can be determined by transformation of the coordinates into real space. SAED experiments are conveniently carried out in a TEM, as the fitting electron optics to generate a suitable electron beam are already present. In this work SAED was used to confirm the findings from X-ray diffraction and to identify crystalline areas in samples that comprised a large fraction of amorphous material. Experiments were carried out in a JEOL JEM-2200FS energy filtered transmission electron microscope with Schottky field emission gun and In-Column Omega energy filter. The acceleration voltage was set to 200 kV.

3.8.3 Spectroscopic methods

3.8.3.1 Infrared spectroscopy

Photons belonging to the infrared (IR) part of the electromagnetic spectrum have a fitting energy to excite molecular vibrations or phonons in solids. Therefore, infrared absorption spectra contain information on the nature of chemical bonds present in a sample. Several IR-based techniques allow for a quick investigation of solids. For example, attenuated total reflection Fourier transform infrared (ATR-FTIR) spectroscopy can probe bonds near the surface of the sample and is therefore sufficient for a full IR characterization in the case of small nanoparticles. For the characterization of powders with larger grain size, diffuse reflectance infrared Fourier-transform (DRIFT) spectroscopy is a convenient technique. In a DRIFT spectrometer, the light that is diffusely scattered by a sample is collected and focused onto the detector by a collimating mirror arrangement. FTIR-ATR and DRIFT spectroscopy were employed for characterization of the metal-oxygen bonds in ferrites, as well as for the identification of organic species in surface-functionalized composites. FTIR-ATR spectra were measured with a JASCO FT/IR-6100 spectrometer in a range of 400–4000 cm^{-1} . DRIFT spectra were recorded in a range of 400–4000 cm^{-1} , using either a Bruker alpha (University of Giessen) or Bruker alpha 2 (University of Bayreuth) spectrometer, equipped with a modular DRIFT unit.

3.8.3.2 Raman spectroscopy

When a molecule or solid is irradiated with monochromatic light of appropriate photon energy (Lasers with wavelengths ranging from the UV to the NIR regime are commonly used for Raman spectroscopy), different types of scattered radiation are observed. Besides the elastically scattered, so-called Rayleigh scattering, also inelastically scattered photons can be detected. The energy of this radiation differs from the wavelength of the incident light, and its intensity is usually much lower than that of the Rayleigh scattering signal. Raman spectroscopy probes the inelastically scattered light in relation to the energy difference (Raman shift) to the incident light. Since the inelastically scattered signals originate from the interaction with vibrational states, they occur in a wavenumber-range of 100–4000 cm^{-1} depending on the chemical environment of the investigated bond, similar to IR

spectroscopy. For a vibration to be Raman-active, the polarizability of the system must change during the course of the molecular oscillation, while the dipole moment remains constant. This makes the technique complementary to conventional infrared spectroscopy, where the situation is reversed and only vibrations that result in a change of the dipole moment can be detected.

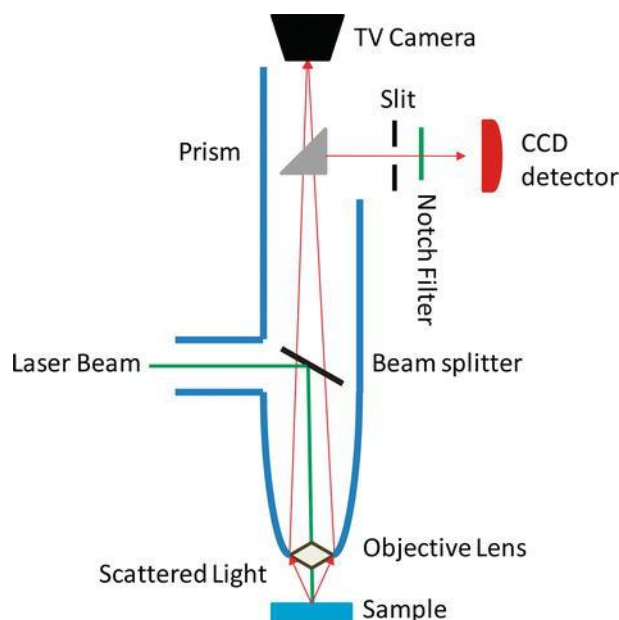


Figure 23: Setup of a conventional Raman spectrometer with microscope optics (Image taken from [153]).

The fact that the laser light is diffusely scattered in all directions upon interaction with the sample allows the construction of spectrometers where both the incident and the scattered light are guided through microscope optics (Figure 23), minimizing the preparation effort and allowing the investigation of extremely small amounts of sample. In this work, Raman spectroscopy was mainly used to exclude the presence of hematite, since Raman spectroscopy is very sensitive to the presence of this particular iron oxide and even small impurities can be easily detected.

To collect Raman spectra of ferrites, small amounts of sample (<1 mg) were prepared on a microscope slide. Raman spectra were collected using a Bruker Senterra Raman spectrometer equipped with microscope optics (20x, 50x or 100x magnification were chosen depending on the signal intensity). The incident beam was provided by a 532 nm Nd:YAG laser operated at 0.2 mW. The software OPUS 7.5 was used for control of the instrument parameters and for data processing. Typical measurements were performed with a spectral resolution of 9–15 cm^{-1} . The spectra were averaged from 100 individual measurements collected with an integration time of 5 s.

3.8.3.3 UV-Vis-NIR spectroscopy

Compared to IR light, UV light and visible (Vis) light are located at higher photon energies in the electromagnetic spectrum. The respective photon energies are too low to excite electronic core states. The excitation of weakly bound valence electrons is however facilitated by UV- and visible light (as well as NIR light to some degree). In the case of semiconductors, electrons can be excited from the valence band into the conduction band if the photon energy is larger than E_g . When the photon energy is lower than E_g , the light is instead reflected by the semiconductor. In the spectrum of a semiconductor, the band gap is visible as a sharp absorption edge located at the wavelength corresponding to E_g . Similar to DRIFT spectroscopy, mirror arrangements (as well as integrating spheres) are available to measure the light that is diffusely reflected by a solid after interaction with its electronic system. The measured reflection spectra can be converted into absorption spectra using Equation 7, which was initially developed by Kubelka and Munk to describe the absorption of pigments and wall colors.^[154] Here, R_∞ describes the diffuse reflectance of an infinitely thick layer of the absorbing material and $F(R_\infty)$ is the absorption function.

$$F(R_\infty) = \frac{(1 - R_\infty)^2}{2R_\infty} \quad (7)$$

For a precise determination of the band gap of a semiconductor usually a so-called Tauc plot is constructed from the absorption spectrum using Equation 8.^[155] The exponent in the equation accounts for the different excitation probabilities of semiconductors with direct and indirect band gaps. The value of n in the exponent is either 0.5 (direct band gap) or 2 (indirect band gap), respectively. Using the Tauc plot, the optical band gap can be derived from the point of intersection of the linear part of the absorption edge and the abscissa.

$$F_{Tauc} = (F(R_\infty) \cdot h\nu)^{\frac{1}{n}} \quad (8)$$

Diffuse reflectance UV-Vis-NIR spectra were recorded in a range of 200–1500 nm, using a Perkin Elmer Lambda 750 spectrometer equipped with a deuterium lamp for the UV regime and a tungsten lamp providing light in the Vis and NIR regime. The lamp change was performed at 319 nm. A Harrick Praying Mantis mirror unit was used to collect the diffusely scattered light. All measurements were taken against a Spectralon PTFE pellet as white standard.

3.8.3.4 X-ray absorption near edge structure spectroscopy

X-ray absorption spectroscopy (XAS) is usually measured in transmission geometry using X-rays from a synchrotron radiation source coupled with a monochromator to select the energy of the incident photons. In this configuration, the technique is comparable to other spectroscopic techniques using electromagnetic radiation, with the exception that the employed X-rays have sufficient energy to probe the electronic core states of a selected element (Figure 24a). X-ray absorption spectra are usually divided into the X-ray absorption near edge structure (XANES) regime in close proximity to an absorption edge and the extended X-ray absorption fine structure (EXAFS) regime at higher excitation energies (Figure 24b). The XANES regime contains information about the empty states comprising the CB and therefore XANES can be a viable technique to probe the electronic structure of semiconductors. Additionally, information on the coordinating ligand sphere around the element under investigation can be obtained.

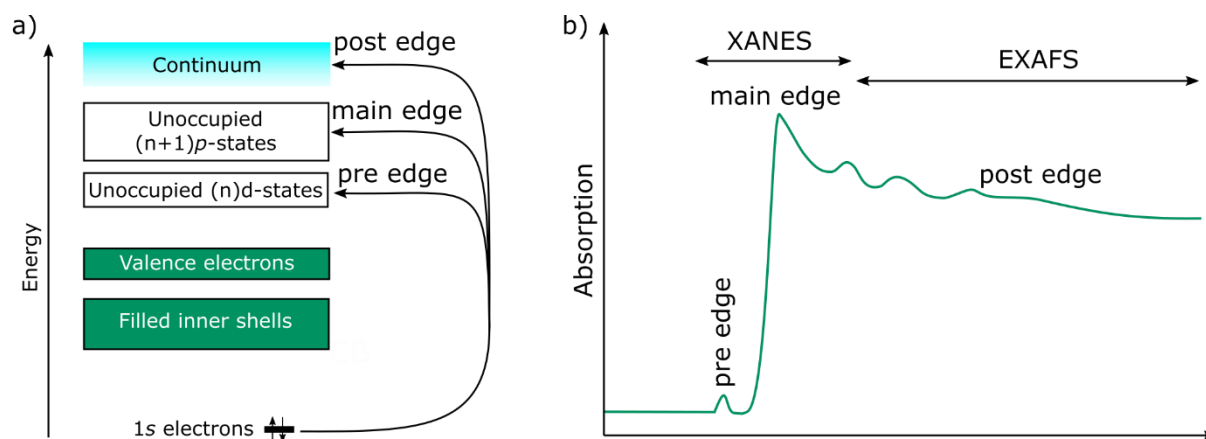


Figure 24: a) Schematic illustration of the X-ray mediated excitations of a 1s core electron into unoccupied electronic states. b) Assignment of the respective regions in an exemplary X-ray absorption spectrum.

For the excitation of 1s electrons (K edge), usually hard X-rays with an energy of several keV are required. In this case, the nature of the main absorption edge is determined by excitations into empty p -states of the element under investigation, because of dipole selection rules. In some cases, where the investigated element contains empty d -states, they can be observed in the spectra as pre-edge signals, due to hybridization phenomena. Since the binding energy of electrons in the core orbitals rises continuously with the atomic number, XAS is an element specific technique. To overcome the strong line broadening (which is a consequence of the short life-time of the generated core-hole) observed in conventional XAS measurements, fluorescence detected techniques were developed.^[156] Such measurements rely on the indirect determination of the XANES spectrum *via* the detection of the emitted X-ray fluorescence. The photon energy of the incident beam is hereby scanned in the energy

range corresponding to the absorption edge of interest. At the same time, the total count of emitted photons (Total fluorescence yield, TFY) or the photon count at a specific emission line (High energy resolution fluorescence detected, HERFD) is detected. The latter technique requires the use of an appropriate spectrometer built in the *Johann*- or the *von Hamos* configuration (Figure 25). Since the number of emitted photons is proportional to the absorption of X-rays, an absorption spectrum can be calculated from the emission intensity. Especially for elements with a high atomic number, HERFD-XANES allows for a much better energy resolution compared to conventional X-ray absorption spectroscopy.^[157] Due to the narrower line widths, HERFD-XANES is able to resolve the pre-edge features corresponding to the excitation of core electrons into CB states.

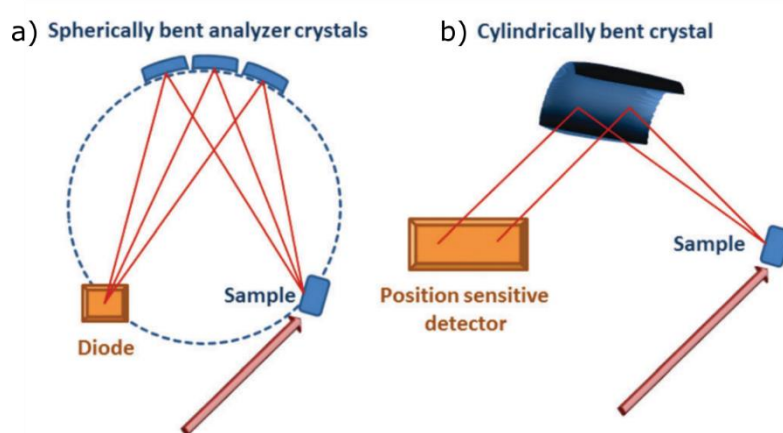


Figure 25: Schematic representation of the Johann type (a) and the von Hamos type (b) spectrometer configurations (Image taken from [156] - Published by the PCCP Owner Societies).

HERFD-XANES spectra were collected in December 2017 at the BM20 beamline at the European Synchrotron Research Facility (ESRF) in Grenoble, France (Experiment Code: CH5027). For the measurements, the samples were diluted with boron nitride, fixed in polyimide foil, and mounted on an XYZ-Stage. The energy of the incident beam was scanned over a range of 7090 – 7220 eV and the fluorescence was detected at an emission energy of 6405 eV (Fe $K\alpha$ line) using a Johann type spectrometer equipped with one analyzer crystal and a position sensitive silicon drift detector.

3.8.3.5 Valence-to-core X-ray emission spectroscopy

As the name suggests, valence-to-core X-ray emission spectroscopy (VtC-XES) probes the radiation that is emitted during the radiative decay of valence electrons into a $1s$ core hole, after a typically non-resonant excitation (Figure 26). In the case of transition metal oxides, the fluorescence radiation originates from the decay of metal d -states with $O2p$ electron density from the ligating oxygen contributing to local wavefunction. Shape and position of the VtC signal therefore contain both information about the energy of the VB electrons and about the chemical environment of the probed

transition metal center. To generate the core hole, a fixed excitation energy of several hundred eV above the K edge is chosen. The emission intensity is then measured depending on the emission wavelength, using a spectrometer of the *Johann*- or *von Hamos* geometry (see Figure 25), similar to the ones used in HERFD-XANES spectroscopy. The probability that a core hole is filled by a metal *p*-electron is considerably higher than by one related to the valence-to-core transitions. The intensity of the respective $K\beta_{2,5}$ signal is therefore smaller than *e.g.* the $K\alpha$ or $K\beta$ signals, typically by several orders of magnitude (Figure 26b). Hence, spectroscopy of the $K\beta_{2,5}$ emission line usually requires an X-ray source with sufficiently high photon flux, as it can nowadays only be provided by a high brilliance synchrotron.

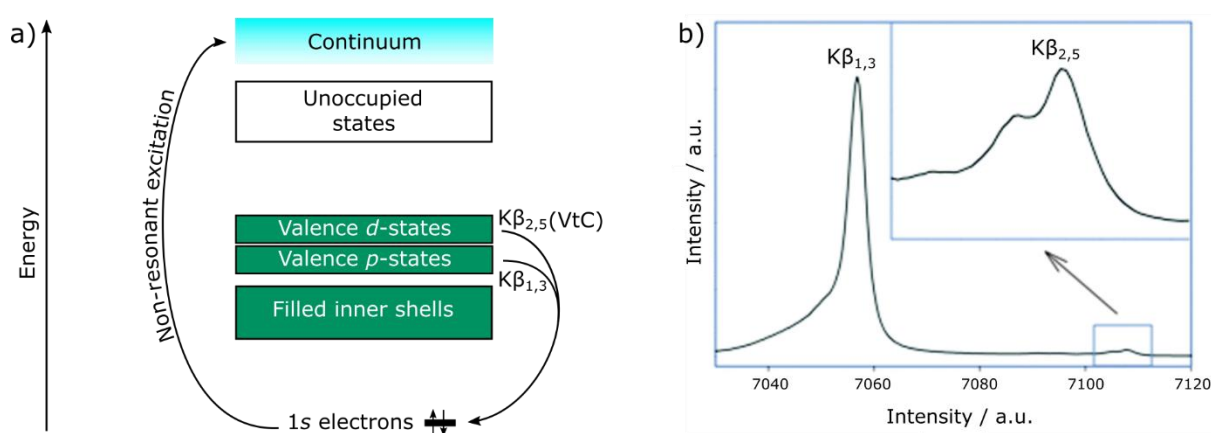


Figure 26: a) Schematic illustration of the electronic transitions probed in VtC spectroscopy. b) Exemplary X-ray emission spectrum of ferrocene to illustrate the intensity difference between the $K\beta_{1,3}$ emission line at 7058 eV and the VtC signal at 7110 eV (Image adapted from [156] - Published by the PCCP Owner Societies).

VtC-XES measurements were performed in November 2019, at the *I20 Scanning* Beamline at Diamond Light Source at Harwell Campus, Oxfordshire, United Kingdom (Experiment Code: SP23538-1). For the measurements, the ferrite samples were pressed to pellets (each containing 100 mg of ferrite powder mixed with 20 mg of cellulose for better binding) and mounted on an XYZ-stage. The incident photon energy was fixed to 7500 eV using a *four bounce* dual-crystal Si (111) monochromator. Emission spectra were collected under ambient conditions, in a range from 7070 – 7140 eV using a *Johann* type spectrometer equipped with 3 analyzer crystals and a *Medipix* 2D detector arranged in a 1 m Rowland Circle. Step width and integration time were tuned for different parts of the spectrum to obtain the best results. The minimum step size was 0.2 eV and the maximum integration time was 30 s in the area where the highest resolution was required. To further reduce noise and to confirm the homogeneity of the samples, the shown spectra were averaged from at least 4 individual scans, which were taken at different sites of the pellet in some cases. Since the $K\beta_{2,5}$ signal is located on the high-energy

exponential tail of the approximately pseudo-Voigt shaped $K\beta_{1,3}$ signal, the background was fitted using a two-phase exponential decay function (Equation 9), and removed from the shown spectra.^[158]

$$y = y_0 + A_1 \cdot e^{-\frac{x-x_0}{k_1}} + Y = Y_0 + A_2 \cdot e^{-\frac{x-x_0}{k_2}} \quad (9)$$

Here x_0 and y_0 represent the offset on the respective axis, A_1 and A_2 are amplitudes and k_1 and k_2 represent decay constants. The respective fit curves are depicted in Figure A1 in the appendix.

3.8.3.6 Energy dispersive X-ray spectroscopy

Energy dispersive X-ray spectroscopy (EDX) probes the X-ray fluorescence emitted upon excitation of a sample with a focused electron beam. The energy of the incident electrons is chosen depending on the elemental composition of the sample and is usually in the range of several keV. Upon interaction with the sample, the incident electrons remove electrons both from inner shell orbitals as well as from orbitals with higher energy. When the resulting core-holes are filled by electrons of a higher shell, X-rays are emitted with specific wavelengths that can be monitored by a detector mounted above the sample. The achievable energy resolution in such an experiment is much lower compared to specialized, synchrotron radiation based XES techniques. However, EDX provides a quick means to acquire a full X-ray emission spectrum of a sample. As described before, X-ray emission spectra are element specific. EDX therefore provides a convenient way to determine the presence of an element in a semi-quantitative fashion. Since most of the components required for the measurement of an EDX spectrum are already present in a scanning electron microscope, EDX measurements are usually performed in a SEM equipped with a dedicated EDX detector.

EDX spectra were collected using either a Zeiss Merlin field-emission SEM, equipped with an Oxford instruments X-Max 50 silicon drift detector (University of Giessen), or a Zeiss LEO 1530 SEM equipped with Thermo Fisher Scientific NS7 UltraDry EDX detector (University of Bayreuth). Acceleration voltages of 10 kV and 15 kV and working distances of 5 mm and 8 mm were used, respectively. Semi-quantitative determination of the elemental composition was performed from spectra acquired at 5 different sites on each sample.

3.8.3.7 Mössbauer spectroscopy

Mössbauer spectroscopy is a nuclear spectroscopic technique able to probe the hyperfine structure of a gamma ray absorber. The technique is based on the Mössbauer effect^[159] as well as on the doppler effect, which is utilized to modulate the energy of the gamma radiation source. Since the presence of a hyperfine structure originates from interactions between the nuclear magnetic dipole moment and the magnetic moments of the surrounding electrons, Mössbauer spectroscopy is sensitive to changes in the local magnetic field around the investigated element. Additional to oxidation numbers and spin states, information about the coordination sphere around cations in a solid can be obtained from such measurements. The applicability of Mössbauer spectroscopy is limited to a small selection of elements, since a gamma emitter with a fitting decay rate must be available to provide gamma radiation of appropriate wavelength and intensity. For the investigation of iron samples, ⁵⁷Co gamma sources fulfill those demands and are additionally relatively cheap. Therefore, Mössbauer spectroscopy is well-suited for the investigation of ferrites. Apart from the exotic nature of the radiation source and the energy modulation, the experimental setup of a Mössbauer spectrometer is similar to those found in other transmission-based spectroscopic techniques.

Low-temperature zero-field Mössbauer spectra were recorded at 14 K/80 K using a SeeCo constant acceleration spectrometer equipped with a ⁵⁷Co radiation source embedded in a Rh matrix and a Janis temperature controller maintaining temperatures within ± 0.1 K (University of Bochum). Data were fit with a hyperfine field distribution and Voigt based fitting to address the ferromagnetic nature of the materials using a least-square routine with the WMOSS program.^[160] Room temperature zero-field Mössbauer spectra were recorded in constant-acceleration mode, using a self-built Mössbauer spectrometer equipped with a 50 mCi⁵⁷Co radiation source embedded in a Rh matrix (University of Bayreuth). All given isomer shifts are referred to α -Fe at room temperature.

3.8.4 SQUID magnetometry

Superconducting quantum interference devices (SQUID) are designed for the precise measurement of very small changes of magnetic fields. The technique relies on the physical phenomena of flux quantization and Josephson tunneling.^[161] When a direct current I_0 is flowing through a superconducting loop in the absence of an external magnetic influence, the current equally splits through the individual branches of the loop. When the system is exposed to an external magnetic field, an additional circular screening current I_S is induced, producing a magnetic field that compensates for the external magnetic flux. This current is in reverse direction to I_0 in one branch but in the same direction as I_0 in the other branch of the loop and consequentially the resulting currents are decreased and increased by the same value, respectively. The circular current however is not strictly proportional

to the external magnetic field, due to the quantization of the magnetic flux in superconducting loops.^[162] The magnetic flux generated by the circular current can only adopt an integer multiple of the flux quantum Φ_0 , which is defined according to Equation 10.

$$\Phi_0 = \frac{h}{2e} \approx 2.07 \cdot 10^{-15} \text{ V s} \quad (10)$$

Here, h is Planck's constant and e represents the electronic charge. A conventional DC SQUID consists of a superconducting loop that is separated into halves by two parallel Josephson junctions (Figure 27). Each Josephson junction consists of a thin insulator layer, which allows the tunneling of cooper pairs above a critical current I_C .^[163] When the critical current is exceeded in either of the branches, a voltage can be measure across the junction, which is dependent both on I_0 and I_S . Due to the flux quantization, a periodic (nearly sinusoidal) flux-voltage characteristic is observed which allows a very precise measurement of changes of the magnetic flux density, caused by a magnetic sample in contact with the SQUID.

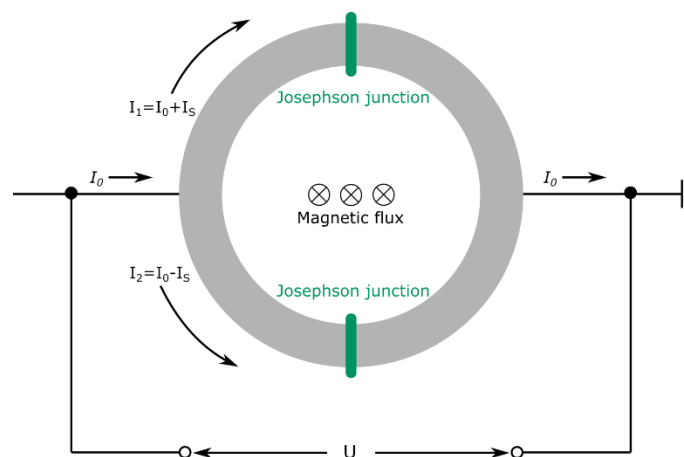


Figure 27: Schematic depiction of a superconducting quantum interference device (Image adapted from [161]).

SQUID measurements were collected using a SQUID MPMS-XL5 instrument from Quantum Design. The samples were cooled down in the absence of an external magnetic field. The field measurements at 10 K and 300 K were performed from 100 Oe to 20000 Oe to -20000 Oe in hysteresis mode, with a step width of 500 Oe. Zero-field cooled magnetization (ZFCM) scans were performed with an applied field of 100 Oe from 10 K to 400 K in sweep mode with a velocity of 5 K min⁻¹. The samples were prepared in gelatin capsules held in a plastic straw. The raw data was corrected for the diamagnetism of the sample holder.

3.8.5 Thermoanalytic techniques

Thermogravimetric analysis (TGA) is used to observe changes in the mass of a sample upon thermal treatment in a specific atmosphere. TGA was performed to determine the percentage of organic residues in the as-synthesized microwave samples. Differential scanning calorimetry (DSC) compares the heating profile of a sample with that of an inert reference. This way changes in the morphology or crystal structure upon thermal treatment can be revealed. DSC was employed to investigate the formation of macroporous CaFe_2O_4 . All thermoanalytic experiments were carried out in air. Thermogravimetric measurements of MgFe_2O_4 nanoparticles were carried out with a Netzsch STA409PC thermos scale (University of Giessen), in a temperature range of 28–1000 °C and with a heating rate of 5 K min⁻¹. TGA and DSC on CaFe_2O_4 were performed using a Netzsch STA449 thermal analysis setup. Data were recorded in a range of 25–1000 °C with a heating rate of 2 K min⁻¹.

3.8.6 Nitrogen physisorption

The adsorption behavior of gases on the surface of solids can be used to characterize their morphology and surface structure. The technique relies on the Van-der-Waals force driven adsorption of gas molecules (adsorptive) on the surface of a solid (adsorbent). Since the attractive forces between a solid and a gas are usually larger than the forces between individual gas particles, physisorption phenomena occur already at low partial pressures (below the saturation vapor pressure of the employed gas), where no condensation is observed. Since the adsorption is measured at a temperature fixed at the boiling point of the employed adsorptive, the obtained adsorption-desorption curves are commonly denoted as isotherms. In many cases, molecular nitrogen is employed as adsorbent, as it is inexpensive and easy to handle. The experiments are therefore performed at 77 K. However, it has been demonstrated that other gases (*e.g.* Ar, Kr, Xe, CO₂) are better suited in many cases.^[164]

In a specific pressure range, the amount of adsorbed gas molecules is proportional to the surface of the investigated materials. It is therefore possible to calculate the surface area of the adsorbent from the respective part of the isotherm. Various models have been developed for the interpretation of isotherms. Among them, the Brunauer-Emmet-Teller (BET) theory is the one most often employed nowadays.^[164,165] For the calculation of the specific surface area of microporous materials, the pressure range is adjusted by using the so-called Rouquerol-plot.^[166] Using the BET equation (Equation 11), the specific surface area of the synthesized materials was calculated by a multi-point analysis of data in the pressure range of $p/p_0=0.05-0.3$.

$$\frac{p}{n(P_0 - p)} = \frac{1}{n_m C} + \frac{C - 1}{n_m C} \frac{p}{p_0} \quad (11)$$

Here, p and p_0 are the equilibrium pressure and the saturation pressure, respectively. The adsorbed gas quantity is represented by n , while n_m stands for the gas quantity that is adsorbed on a monolayer. C is a constant that is dependent on the heat of adsorption.

Nitrogen physisorption was performed using either a Quantachrome Quadrasorb, a Quantachrome Autosorb-IQ2 (both University of Giessen) or an Anton Paar QuantaTec ASiQ-MP-MP-AG instrument (University of Bayreuth). Samples were degassed at 120 °C under vacuum, prior to the measurements. By employing non-local density functional theory (NLDFT) calculations, information on micro- and mesopores in a material can be obtained from gas physisorption isotherms.^[164] In this work, pore size distributions of the porous host networks in composites were calculated by NLDFT, assuming an equilibrium model for silica with slit pores as adsorbent. Pores were classified as micropores ($d_{\text{pore}} < 2 \text{ nm}$) and mesopores ($2 \text{ nm} < d_{\text{pore}} < 50 \text{ nm}$) according to the IUPAC guidelines.^[164]

3.8.7 Mercury intrusion porosimetry

Similar to gas physisorption, mercury intrusion porosimetry (MIP) can be used to investigate the pore structure of a material. In contrast to physisorption, however the pores are filled with mercury that is forced into the pore system at elevated pressures during the measurement. This bears the disadvantage, that the pore system can collapse, which might lead to a wrong interpretation of the resulting data. Furthermore, removal of the mercury, once in the pores, is usually impossible, making MIP an invasive technique. The advantage of this technique lies however in the possibility to investigate macropores ($d_{\text{pore}} > 50 \text{ nm}$), while gas physisorption is limited to the detection of micro- and mesopores. Hence, MIP was employed to investigate the formation of the macropore structure of the CaFe_2O_4 samples synthesized for this work. The measurements were performed in a pressure range of 0–400 MPa using a Thermo Fisher Scientific Pascal 140/440 porosimeter. 140° and 0.48 N/m were assumed as the contact angle and surface tension of mercury, respectively. Data processing was performed with the Software Sol.I.D and the pore sizes were calculated according to the Washburn equation.^[167]

3.8.8 Photocatalysis

The photocatalytic performance of MgFe_2O_4 nanoparticles and macroporous CaFe_2O_4 was investigated using different self-built reactor setups.

3.8.8.1 Hydrogen evolution

Hydrogen evolution experiments using visible light were attempted at 20 °C using a Newport Sol1A solar simulator equipped with a Xe lamp operated at 145 W, providing irradiation from the top. The UV part of the Xe spectrum was removed by an AM1.5G filter that was placed in the light path. For irradiation of the samples with UV-light, a mid-pressure Hg lamp operated at 500 W in an inner-irradiation geometry was used and the temperature was kept at 10 °C. All gas evolution experiments were performed under magnetic stirring in a sealed reactor-detector array, flushed with Ar as carrier gas. Gas detection was performed using either a Shimadzu GC 2014 gas chromatograph equipped with a TCD detector, or a Hiden HPR-20 Q/C quadrupole mass spectrometer. For photodeposition of co-catalysts, up to 1 wt.-% Rh or Pt were added during the experiment, in the form of Na_3RhCl_6 and H_2PtCl_6 , respectively. For overall water splitting tests, 0.1 wt.-% of RhCrOx nanoparticles were deposited previously to the experiment adapting a procedure by Zhao *et al.*^[168]

3.8.8.2 Degradation of organic compounds

Degradation of nitrobenzene was attempted at 20 °C, using a suspension of 100 mg of photocatalyst in a 10^{-4} M ethanolic solution of nitrobenzene. Irradiation was performed from the top using a Newport Sol1A solar simulator equipped with Xe lamp operated at 145 W, both with and without AM1.5G filter in the beam path. The degradation of nitrobenzene was monitored by UV-Vis spectroscopy.

Degradation of rhodamine B (RhB) was attempted at 20 °C, using a suspension of 100 mg of photocatalyst in a 10^{-5} M aqueous solution of RhB. Irradiation was performed from the top using a Newport Sol1A solar simulator equipped with Xe lamp operated at 145 W, both with and without AM1.5G filter in the beam path. The degradation of RhB was monitored by UV-Vis spectroscopy.

Degradation of 2,6-dichloroindophenol was attempted at 0 °C, using a suspension of 50 mg of photocatalyst in an aqueous solution containing $5 \cdot 10^{-5}$ M 2,6-dichloroindophenol and 10^{-2} M KNO_3 . In one case 2.3 w% of Pt were deposited prior to the degradation experiment by adapting a procedure by Baumanis *et al.*^[169] Irradiation was performed from the top using a solar simulator equipped with Xe lamp operated at 300 W. A longpass filter ($\lambda > 360$ nm) placed in the light path, to remove UV-light. The degradation of 2,6-dichloroindophenol was monitored by UV-Vis spectroscopy.

3.8.9 (Photo-)electrochemistry

For all electrochemical measurements, ferrite photoelectrodes were mounted in a PTFE cell with a 1 cm² quartz window, containing a solution of 0.1 M Na₂SO₄ as electrolyte (Figure 28). For chopped-light voltammetry (CLV) and incident photon to current efficiency (IPCE) spectroscopy, 0.015 M of H₂O₂ were added to the electrolyte. Measurements were performed with a Zahner Zennium potentiostat using a three-electrode configuration with the photoelectrode acting as working electrode, a Pt wire as counter electrode and Ag/AgCl in 3M NaCl as reference electrode.

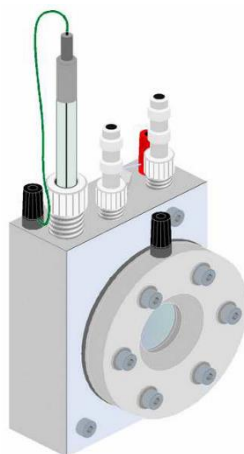


Figure 28: Schematic depiction of the PTFE cell that was used in all photoelectrochemical measurements.

3.8.9.1 Mott-Schottky analysis

Mott-Schottky analysis is an electrochemical method for the determination of flat band potentials and donor densities of semiconductor electrodes. The flat band potential is defined as the external potential that must be applied to cancel out the band bending that occurs at the semiconductor-liquid interface, due to fermi level equilibration. For highly *n*-doped and *p*-doped semiconductors, the flat band potential is located close to the CMB or VBM respectively. Therefore Mott-Schottky analysis provides a means to determine the potential of one of the band edges. When the band gap of the semiconductor is known (for example from optical spectroscopy) the energy of both band edges can be approximated. To construct a Mott Schottky plot, the inverse square capacitance of the semiconductor-electrolyte interface is recorded, while the external potential applied to the electrode is varied. The electrochemical system is hereby commonly described by a simple capacitor equivalent circuit and the capacitance is determined from the imaginary part of the electrochemical impedance spectrum. The course of the Mott-Schottky plot is described by the Mott-Schottky equation (Equation 12), where C is the capacitance, ϵ is the relative permittivity of the sample, ϵ_0 is the permittivity of vacuum, A represents the area of the electrode that is in contact with the electrolyte, N_D is the donor density and V_{fb} is the flat band potential.

$$\frac{1}{C^2} = \frac{2}{\epsilon\epsilon_0 A^2 e N_D} \left(V - V_{fb} - \frac{K_B T}{e} \right) \quad (12)$$

Consequentially the donor density can be calculated from the slope of the linear region of the Mott-Schottky plot, while a positive or negative slope indicates *n*-type and *p*-type semiconducting behavior, respectively. The flat band potential can be determined from the intersection of the extrapolated linear slope with the abscissa. In the case of more complex samples like nanostructured ones, Mott-Schottky analysis comes with a large measurement uncertainty, since the assumed capacitor model is usually too simple to describe such systems. The assumption of an improper equivalent circuit may even result in a completely wrong interpretation of the obtained data.^[170] Nevertheless, the technique is routinely applied for the determination of the band potentials of both bulk-, and nanostructured photocatalysts. In this work, Mott-Schottky analysis was performed on ferrite photoelectrodes that were prepared by spray-coating.

3.8.9.2 Chopped-light linear sweep voltammetry and incident photon to current efficiency

For a chopped light voltammetry, the external bias applied on a photoelectrode is continuously altered over a given potential range, while the current generated from a photoelectrochemical half-reaction on the semiconductor-electrolyte interface, is measured. During the potential sweep, irradiation of the sample with light (of appropriate wavelength for an excitation of valence electrons into the conduction band) is periodically switched off and on. The difference of the photocurrent (generated by the exited charge carries) from the dark current is a measure for the performance of the photoelectrode. Depending on the semiconducting nature of the photoelectrode, the detected photocurrent is either positive (*n*-type) or negative (*p*-type). Information about band positions and overpotentials for the investigated electrochemical reaction can be derived from the onset potential of the photocurrent. For CLV measurements in this work, 1 cm² of the ferrite photoelectrode were illuminated with a white light LED emitting in a range of 400–800 nm.

In incident-photon to current efficiency (IPCE) spectroscopy, the photocurrent at a fixed external bias is put into relation to the known photon flux of a tunable light source and can therefore be used to investigate, whether the absorption characteristics of a material can be efficiently exploited for photocurrent generation. For IPCE spectroscopy, illumination was performed with a commercial Zahner TLS03 LED array. The irradiated area on the photoelectrode was 1 cm².

4 Results and discussion

4.1 The microwave-assisted synthesis of MgFe₂O₄ nanoparticles

4.1.1 The phase composition

A synthesis published by Kirchberg *et al.* in 2017 was chosen as the starting point for the investigation of the photocatalytic capabilities of MgFe₂O₄.^[90] The synthesis produced seemingly phase-pure MgFe₂O₄ nanoparticles with spinel structure, as suggested by PXRD and Raman spectroscopy. When the particles were heated to 600 °C for one hour in an oxygen-containing atmosphere, the formation of a small quantity of α -Fe₂O₃ (hematite) was however observed in the respective publication. This observation led to the hypothesis that an iron oxide species might be present in the as-synthesized sample, which could not be detected by the employed characterization procedures. For MgFe₂O₄ nanoparticles synthesized at 200 °C (reproducing the procedure of Kirchberg *et al.*), Energy-dispersive X-ray spectroscopy (Figure A2, appendix) revealed a stoichiometric Mg:Fe ratio of only 0.3. This is significantly below the value of 0.5, which would be expected for a MgFe₂O₄ sample with ideal spinel structure. The magnesium deficiency is a strong indication for the presence of an iron oxide by-phase in the as-synthesized nanoparticles. This by-phase is converted to α -Fe₂O₃ at elevated temperatures in an oxygen containing atmosphere. The magnesium deficiency likely results from the higher condensation velocity of the Fe(acac)₃ precursor, compared to Mg(acac)₂, leading to a preferred formation of Fe-O-Fe bonds in the early stages of the reaction and consequentially the formation of iron oxide nuclei. Notably there is no indication for the formation of a MgO shell around the particles, which would result from the condensation of Mg(acac)₂ after the depletion of the iron precursor in the later stages of the synthesis. Unreacted magnesium precursor is instead removed during the washing process. It is therefore concluded, that the solvent mediated condensation mechanism that was proposed for this type of synthesis does not proceed quantitatively in the case of MgFe₂O₄.^[171] Instead, due to the differences in precursor reactivity, iron oxides like Fe₃O₄ and γ -Fe₂O₃ are formed and magnesium is only partly incorporated into the crystal structure. The formation of Fe₃O₄ would be accompanied by a partial reduction of Fe²⁺ *via* the oxidation of the solvent 1-phenylethanol to acetophenone, which is not unlikely at temperatures above 200 °C.^[172] A post-synthetic calcination study was conducted to investigate the formation of by-phases more closely. Standard calcination stages for the nanoparticles were defined as 400 °C, 600 °C and 800 °C for 60 min, respectively. The corresponding samples are labeled as T400, T600 and T800 in the further course of this work, for simplification.

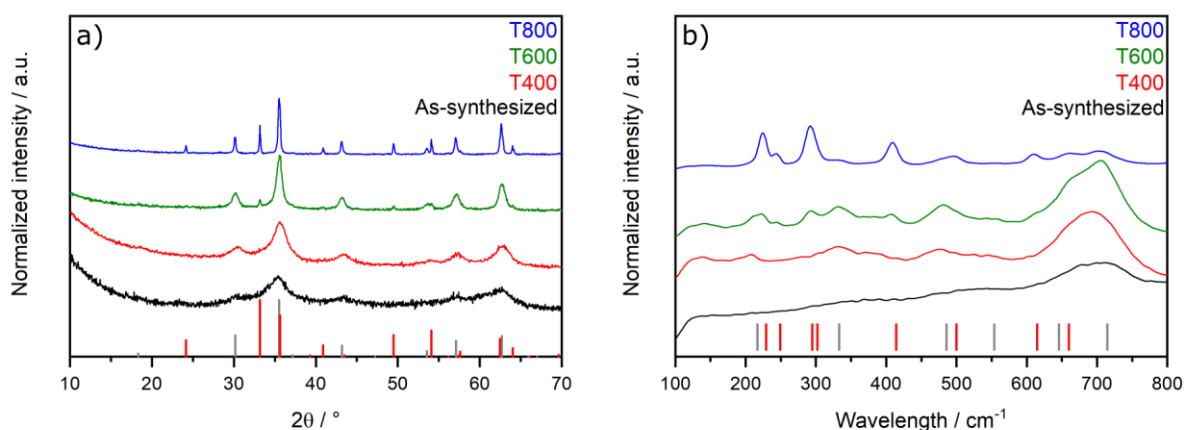


Figure 29: a) XRD patterns of MgFe_2O_4 nanoparticles synthesized with an Mg:Fe ratio of 0.3. The measurements depicted in black correspond to the as-synthesized samples, whereas the colored ones were conducted after calcination at 400 °C (red), 600 °C (green) and 800 °C (blue) respectively. References are given in grey for MgFe_2O_4 (ICDD 01-073-2410) and in red for $\alpha\text{-Fe}_2\text{O}_3$ (ICDD 01-084-0306). b) Raman spectra of the respective samples. References are given in grey for MgFe_2O_4 ^[173] and in red for $\alpha\text{-Fe}_2\text{O}_3$ ^[174]. a,b) adapted from *ACS Appl. Nano Mater.* **2020**, *3*, 11587. Copyright (2020) American Chemical Society.

XRD patterns and Raman spectra of calcined MgFe_2O_4 nanoparticles with a Mg:Fe cationic ratio of 0.3 confirmed the formation of $\alpha\text{-Fe}_2\text{O}_3$, at temperatures around 600 °C (Figure 29). For the T800 sample, the fraction of hematite is considerably increased, and the Raman spectrum is dominated by signals corresponding to this phase, indicating that it was present in large quantities. Therefore, it was necessary to optimize the synthesis procedure, to ensure the formation of a single-phase product, prior to any photocatalytic test reactions.

4.1.2 Optimization of the synthesis

Different strategies were employed to increase the fraction of magnesium in the nanoparticles. Variations of synthesis temperature and reaction time had only a negligible effect on the elemental composition. When the concentration of $\text{Mg}(\text{acac})_2$ in the reaction solution was increased, the magnesium content in the product could be increased, confirming that the condensation of $\text{Mg}(\text{acac})_2$ is hindered compared to the competing condensation of $\text{Fe}(\text{acac})_3$ molecules with each other. Figure 30 shows the respective Mg:Fe-ratio of MgFe_2O_4 nanoparticles synthesized by microwave reaction in a temperature range of 200–275 °C with adjusted precursor composition.

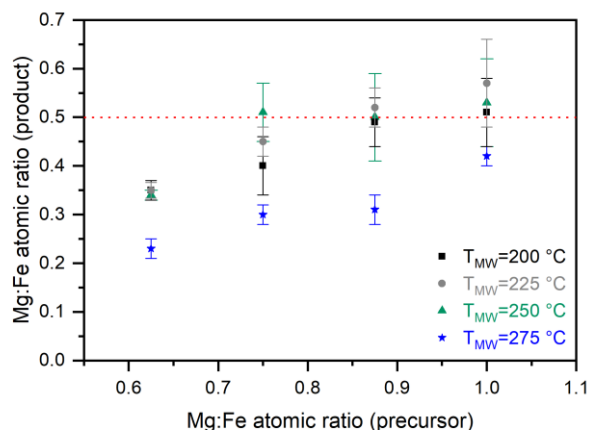


Figure 30: EDX derived Mg:Fe cation ratio of magnesium ferrite nanoparticles synthesized in the microwave in a temperature range of 200–275 °C for 30 min, using different precursor compositions. The dotted red line reflects the ideal stoichiometry of MgFe₂O₄. Figure adapted from *ACS Appl. Nano Mater.* **2020**, *3*, 11587. Copyright (2020) American Chemical Society.

In a temperature range of 200–250 °C, magnesium and iron had to be employed in a ratio of 0.875 (corresponding to an excess of 75%) to ensure an ideal product stoichiometry. An exemplary EDX spectrum of a sample with optimized stoichiometry is depicted in Figure A3 (appendix). The margins of error reflect the standard deviation of five individual sites on sample from which the Mg:Fe ratio was averaged. At a synthesis temperature of 275 °C, the Mg:Fe ratio does not reach 0.5, even when magnesium and iron were employed equimolar during synthesis. A trend can however still be observed and the elemental composition of particles with the highest excess of Mg(acac)₂ is still closer to the ideal value compared to nanoparticles produced by the initial synthesis by Kirchberg *et al.*^[90]

4.2 Material characteristics of MgFe₂O₄ nanoparticles with optimized stoichiometry

Nanoparticles with an optimized elemental composition were subjected to calcination and thorough characterization, to confirm that the formation of iron oxide by-phases can be prevented by an adjustment of the cation composition.

4.2.1 Phase purity and crystal structure

In cases where the Mg:Fe ratio was adjusted to meet the ideal elemental composition of a spinel structure, PXRD and Raman spectroscopy confirm that no α -Fe₂O₃ is formed upon calcination in a temperature range of 400–800 °C (Figure 31). In the case of the sample synthesized at a microwave temperature of 275 °C, a small fraction of hematite can be detected after calcination at 800 °C, since no ideal elemental composition could be attained within the boundaries of the investigated precursor compositions. The concentration of the impurity is lower compared to the particles synthesized by the

direct reproduction of the synthesis by Kirchberg *et al.* and consequentially the reflections originating from α -Fe₂O₃ are hardly visible in the diffraction pattern. The impurity can however be observed as a shoulder on the low-energy side of the E_g signal (333 cm⁻¹) in the Raman spectrum. The observations confirm that the formation of hematite at elevated temperatures is indeed closely related to the Mg:Fe ratio in the nanoparticles.

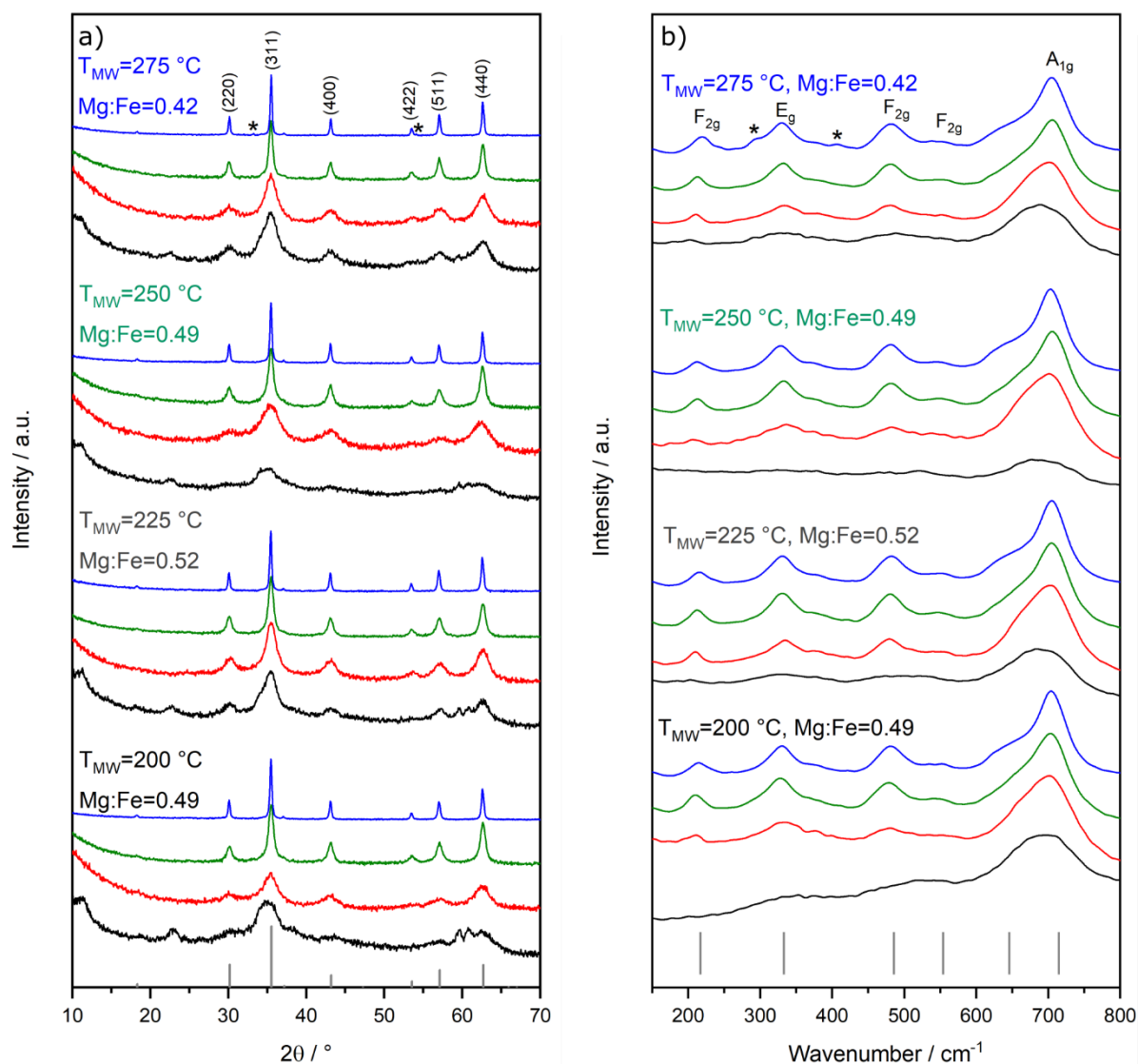


Figure 31: PXRD patterns (a) and Raman spectra (b) of MgFe₂O₄ nanoparticles with optimized stoichiometry, synthesized at different microwave temperatures. The measurements depicted in black correspond to the as-synthesized samples, whereas the colored ones were conducted after calcination at 400 °C (red), 600 °C (green) and 800 °C (blue) respectively. References for the diffraction pattern (ICDD 01-073-2410) and the Raman spectrum^[173] of MgFe₂O₄ are given in grey. Small hematite impurities present in the sample synthesized at 275 °C are marked by an asterisk. a,b) adapted from *ACS Appl. Nano Mater.* **2020**, *3*, 11587. Copyright (2020) American Chemical Society.

The diffraction patterns and Raman spectra are in good accordance with the literature for MgFe₂O₄.^[23,173,175] Since the crystal structure and nature of the Raman-active modes is already well described in the respective publications, they will not be discussed in greater detail during the course of this chapter. Theoretically it should be possible to draw conclusions regarding the degree of inversion from the X-ray diffraction data and Raman spectra, since the (220) reflection in the PXRD patterns and the shoulder observed at 646 cm⁻¹ on the low energy side of the A_{1g} mode in the Raman spectrum are susceptible to changes of the occupation of tetrahedral and octahedral sites.^[173] However, a calculation of the respective values for λ proved to be imprecise, due to the low crystallinity at lower calcination stages, which resulted in broad signals and a low signal-to-noise ratios. Table 4 reveals that the temperature at which the microwave reaction is performed has only a minor influence on the crystallite size (determined by Scherrer's equation, Equation 6, chapter 3.8.2.1) after calcination. For the as-synthesized particles, an approximation of the crystallite size using diffraction data was not possible due to the low crystallinity. With higher calcination temperatures, a continuous increase of the crystallite sizes caused by sintering effects is observed.

Table 4: Crystallite sizes of MgFe₂O₄ nanoparticles synthesized at different temperatures in the microwave and calcined at 400–800 °C.

$T_{MW} / ^\circ\text{C}$	Mg:Fe	$T_{Calc} / ^\circ\text{C}$	$d_{Crystallite} / \text{nm}$
200	0.49	400	3.6 ± 0.3
		600	11.9 ± 0.6
		800	34.6 ± 1.6
225	0.52	400	5.7 ± 1.5
		600	12.2 ± 0.4
		800	33.0 ± 1.4
250	0.49	400	5.2 ± 0.8
		600	11.5 ± 0.9
		800	32.1 ± 1.0
275	0.42	400	6.1 ± 0.5
		600	15.8 ± 0.6
		800	40.1 ± 3.3

Since 200 °C was the minimum temperature, at which phase-pure MgFe₂O₄ nanoparticles could be obtained, this temperature in combination with a stoichiometric excess of Mg(acac)₂ of 75% were chosen as standard synthesis conditions for the production of MgFe₂O₄ nanoparticles. Unless

otherwise specified, any characterization data shown for MgFe₂O₄ nanoparticles in the further course of this work applies to material synthesized by those conditions.

In accordance with the literature, ATR-FTIR spectra of the MgFe₂O₄ nanoparticles show two distinct absorption bands located at 532 cm⁻¹ and 400 cm⁻¹, which originate from Fe-O vibrations with different bond lengths (Figure 32a).^[176] The higher energy vibration at 532 cm⁻¹ is attributed to iron located on tetrahedral sites, while the band at approximately 400 cm⁻¹ originates from octahedrally coordinated iron. The absorption bands at 1520 cm⁻¹ and 1400 cm⁻¹ are attributed to carbonyl groups implying the presence of residual acetylacetonates and to adsorbed moisture, respectively, in accordance with their disappearance after calcination at higher temperatures. Thermogravimetric analysis performed in air confirms this interpretation (Figure 32b).

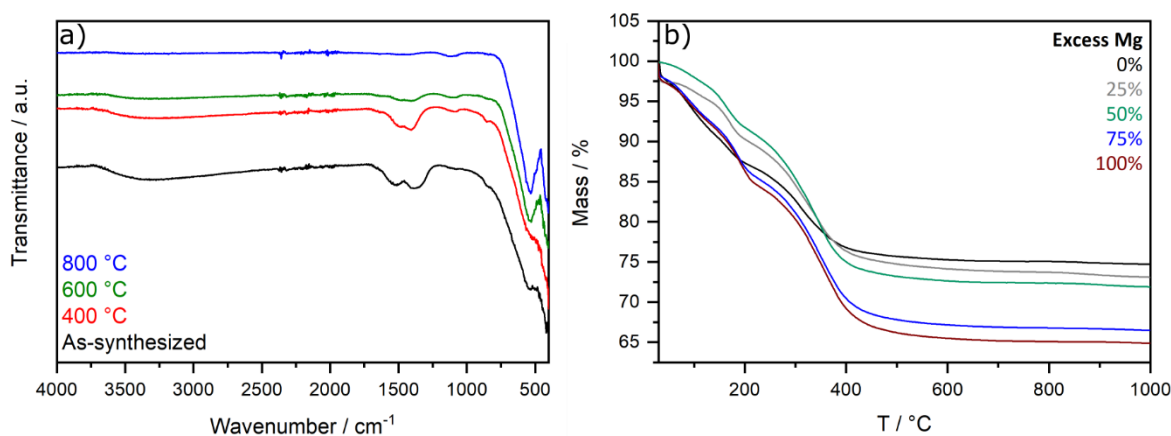


Figure 32: a) ATR-FTIR spectra of MgFe₂O₄ nanoparticles after synthesis (black) and after calcination at 400 °C (red), 600 °C (green) and 800 °C (blue). b) Thermogravimetric mass loss curves of MgFe₂O₄ nanoparticles synthesized at 200 °C with varying excess of Mg(acac)₂. a,b) adapted from *ACS Appl. Nano Mater.* **2020**, *3*, 11587. Copyright (2020) American Chemical Society.

The TGA curves show a mass loss of up to 30% in the temperature range from room temperature to 400 °C, which is attributed to the combustion of the acetylacetonate residues and to the desorption of water. The additional mass loss in a temperature range from 400–1000 °C can likely be attributed to the combustion of small amounts of persistent carbonate species. However, no mass spectrometer was coupled to the TGA setup and respective measurements have to be conducted in the future to confirm this assumption.

4.2.2 Morphology

Electron microscopy (Figure 33,a–h) confirms the nanoparticle morphology of the MgFe₂O₄ samples. Since no surface modification with stabilizing agents was performed and due to the magnetism of the particles, they show a strong trend to form agglomerates.

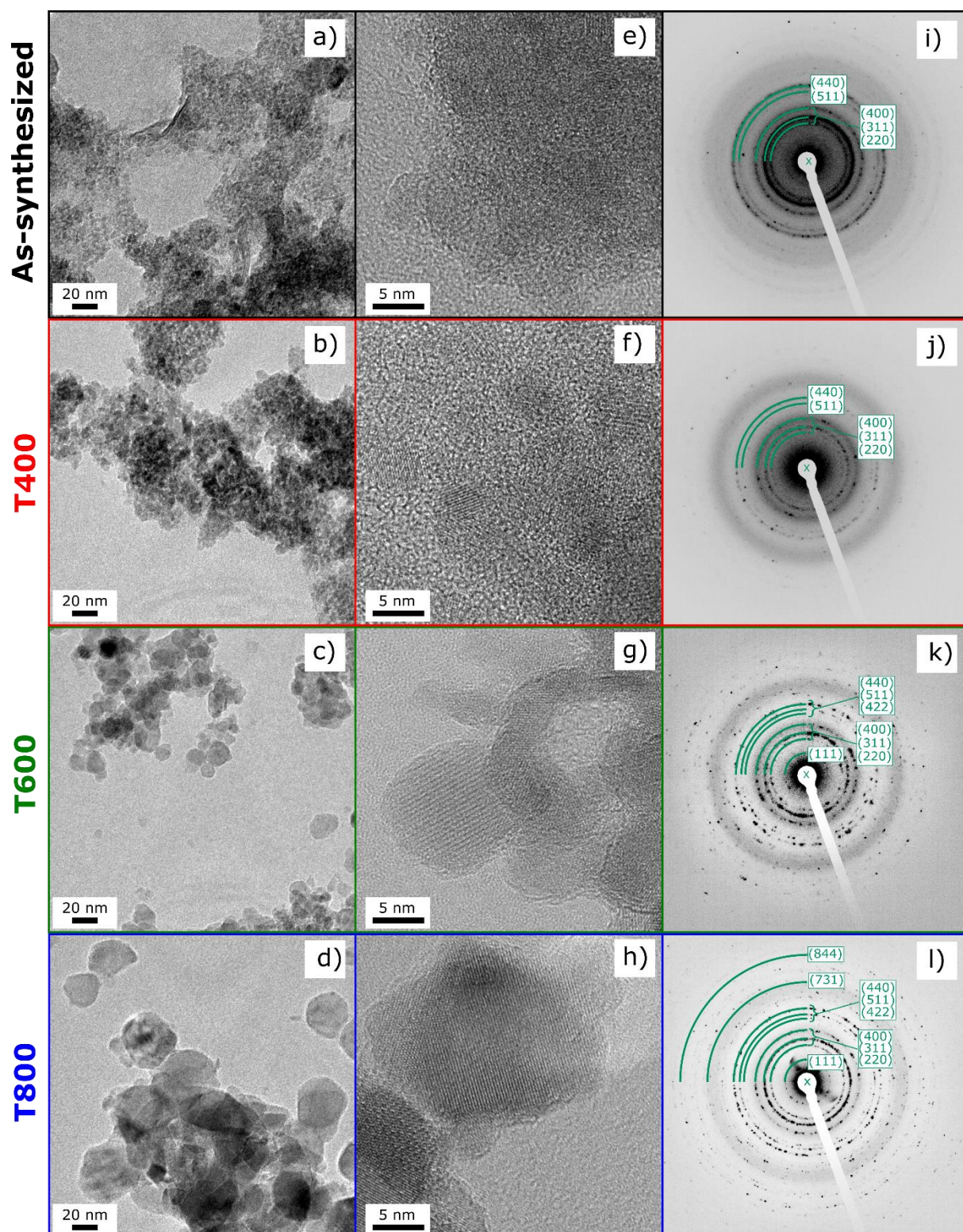


Figure 33: TEM images (a–h) and SAED patterns (i–l) of as-synthesized and calcined MgFe_2O_4 nanoparticles (adapted from *ACS Appl. Nano Mater.* **2020**, 3, 11587. Copyright (2020) American Chemical Society).

For the as-synthesized sample, the identification of individual nanoparticles is challenging, due to their small size and low crystallinity. A continuous growth of the nanoparticles is observed with higher calcination temperatures. From the visual impression, the uniformity of the particle size is decreased

at the higher calcination stages, however a systematic determination of particle size distributions was not conducted. At the higher calcination stages, crystallinity is considerably increased and even reflections belonging to the higher diffraction orders are well resolved. The nanoparticles seemingly remain single-crystalline upon calcination, as observed at higher magnifications, where the (111), (220), (311) and (400) lattice planes become visible. SAED (Figure 33,i–l) underlines the high crystallinity of the calcined samples and confirms that a spinel phase is present in the as-synthesized sample already. For both the as-synthesized nanoparticles and the ones subjected to calcination, N₂-physisorption reveals type IV(a) isotherms with H3-type hysteresis loops, which is common for interparticular voids in non-rigid aggregates of particles (Figure 34a).^[164]

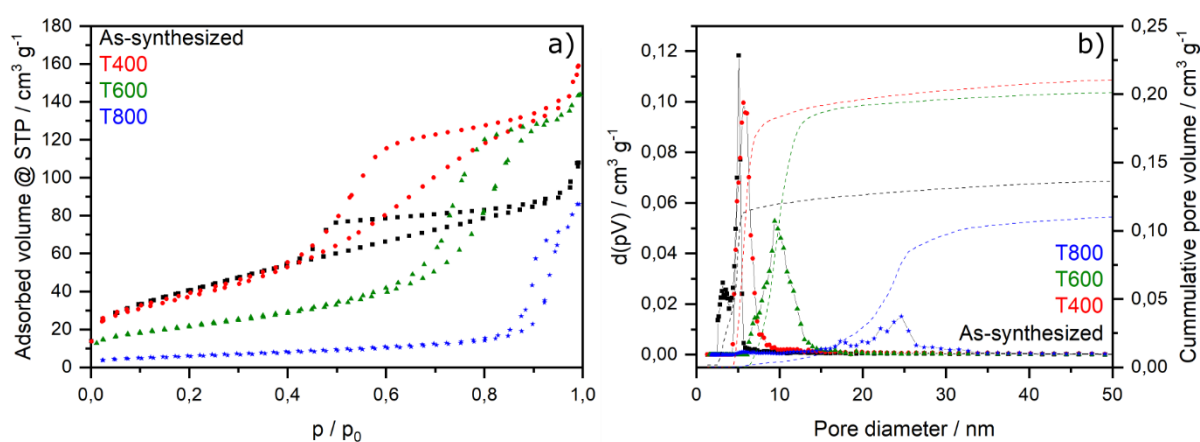


Figure 34: N₂-Physisorption isotherms (a) and NLDFT derived pore-size distribution (b) of MgFe₂O₄ nanoparticles at different calcination stages. a,b) reprinted from *ACS Appl. Nano Mater.* **2020**, *3*, 11587. Copyright (2020) American Chemical Society.

The calcination induced growth of the crystallites is accompanied by a decreasing amount of adsorbed nitrogen at $p=p_0$. The isotherm corresponding to the as-synthesized sample however does not fit into this trend. With increased calcination temperature, the hysteresis loops are shifted towards higher relative pressures, suggesting a growth of the interparticular voids. NLDFT derived pore size distributions and cumulative pore volumina (Figure 34b) help to illustrate the reasons for this behavior. After calcination at 400 °C, the cumulative pore volume is nearly doubled, which suggests that the mass loss observed by FTIR spectroscopy and TGA is related to the combustion of organic residues present in the interparticular cavities of the as-synthesized sample. After the removal of the organic impurity, the cumulative pore volume is decreased continuously with each increase of the calcination temperature due to the temperature induced growth of individual particles (Table 5). The medium pore diameter is increased, and the pore size distribution becomes broader in accordance with the decreased homogeneity of the particle size that was indicated by TEM. As expected, the BET surface area of the higher calcination stages is considerably lower compared to the as-synthesized particles.

Table 5: Results from N₂-physisorption experiments conducted on MgFe₂O₄ nanoparticles at different calcination stages.

T_{Calc}	$d_{\text{Crystallite}} / \text{nm}$	$S_{\text{BET}} / \text{m}^2 \text{g}^{-1}$	Cumulative pore volume / $\text{cm}^3 \text{g}^{-1}$	Weighted average pore diameter / nm
As-synthesized	-	148	0.143	5.2
400 °C	3.6	135	0.219	6.7
600 °C	11.9	77	0.206	10.3
800 °C	34.6	21	0.119	22.1

4.2.3 Magnetic properties

Zero-field ⁵⁷Fe Mössbauer spectroscopy was conducted at a temperature of 80 K, with the aim to reveal changes in the magnetic behavior and the degree of inversion upon calcination. In the case of MgFe₂O₄, a spectrum consisting of two individual sextets (originating from iron in tetrahedral and octahedral coordination) is expected. Such a sextet spectrum, which suggests a permanent magnetic ordering throughout the sample, was only observed for the T600 and T800 calcination stages (Figure 35a). The respective spectra give no indication for the presence of a magnetic by-phase. Due to broad line width, a robust determination of the degree of inversion by a fitting of the individual sub-spectra is unfortunately not feasible. The as-synthesized sample exhibits a doublet with a quadrupole splitting of $\Delta EQ = 0.68 \text{ mm s}^{-1}$, suggesting a (super-)paramagnetic material. The spectrum of the T400 sample is of generally low intensity and it can be assumed that the measurement temperature of 80 K is near the blocking temperature (T_B) of the investigated particles in this case. Those assumptions could be confirmed by Mössbauer spectra recorded at 14 K (Figure 35b). At this temperature, particles of all calcination stages produce a sextet spectrum, confirming a permanent magnetic ordering and a blocking temperature above 14 K. For the as-synthesized sample, some quadruple contribution to the spectrum can still be observed. The line broadening is even more pronounced in the low temperature measurement and the degree of inversion therefore could not be calculated from this data.

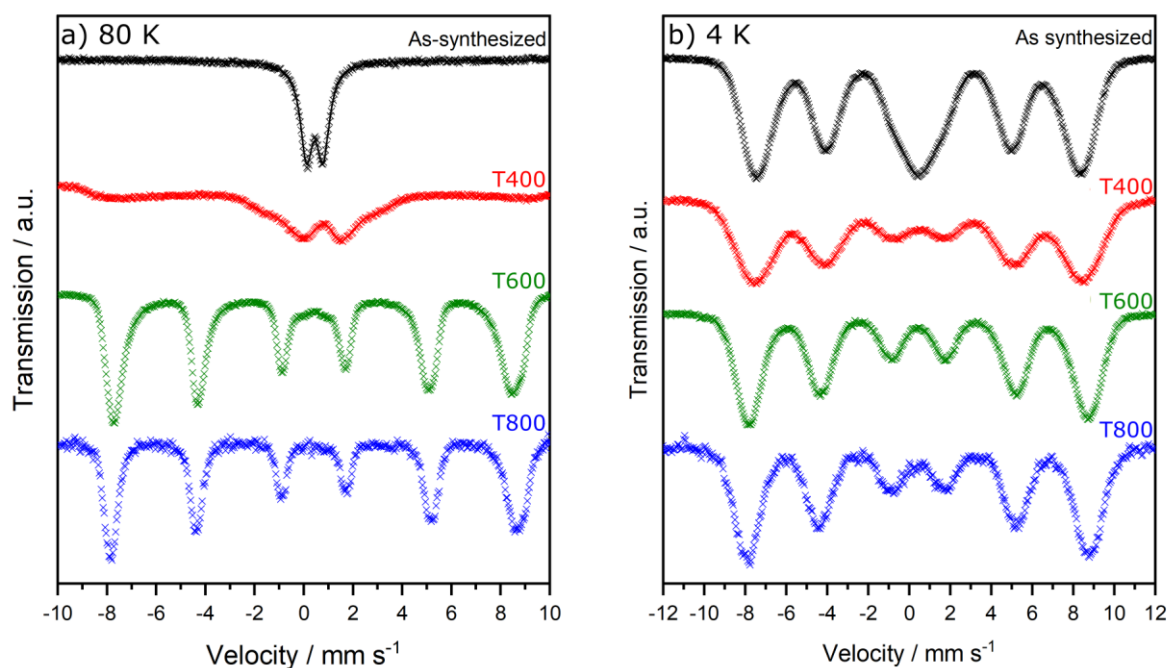


Figure 35: Mössbauer spectra of MgFe₂O₄ nanoparticles at different calcination stages, collected at 80 K (a) and 14 K (b). a, b) reprinted from *ACS Appl. Nano Mater.* **2020**, *3*, 11587. Copyright (2020) American Chemical Society.

The magnetic behavior of the particles that was indicated by Mössbauer spectroscopy could be confirmed using SQUID magnetometry. For a better comparison, the magnetization curves were corrected for the calcination induced loss of diamagnetic mass, which was determined from TGA to be 31.4% for the as-synthesized sample, 3.6% for the T400 sample and 0.4% for the T600 sample. Irrespective of the calcination stage, the magnetization curves collected at 300 K (Figure 36a) do not feature a magnetic hysteresis loop, indicating that the nanoparticles are superparamagnetic at this temperature. For the calcined samples, the saturation magnetization M_s at an external magnetic field of 20000 Oe is increasing with the calcination temperature. The increase of M_s can be interpreted as a continuous decrease of the degree of inversion. However, this conflicts with the results of XANES and VtC measurements (*vide infra*). The decreased M_s at the lower calcination stages is therefore instead attributed to a surface spin disorder effect, which has been reported for small magnetic nanoparticles.^[177] As the nanoparticles exhibit a significant growth at higher calcination temperatures, this effect becomes negligible. The as-synthesized sample does not follow this trend, since it exhibits a considerably higher M_s compared to the sample calcined at 400 °C. This might be an indication for the presence of a crystalline Fe₃O₄ (which has a higher magnetizability) as a trace impurity.^[178] However, no indication for the presence of Fe₃O₄ was found by any of the other employed characterization techniques, and hence the quantity of the contamination must either be very small, or another reason must be responsible for the increased magnetization. One possible explanation is that a cation inversion effect (related to the antiferromagnetic alignment of the spin magnetic

4.2 Material characteristics of MgFe₂O₄ nanoparticles with optimized stoichiometry

moments of Fe³⁺) has a dominating influence on M_S .^[140] In the as-synthesized sample, the crystallinity is low and the weak long range ordering likely prevents the antiparallel alignment of Fe³⁺ on tetrahedral and octahedral sites, leading to a strongly increased M_S . Upon calcination at 400 °C, crystallinity is increased, and consequentially the saturation magnetization is decreased due to the antiferromagnetic exchange interactions.

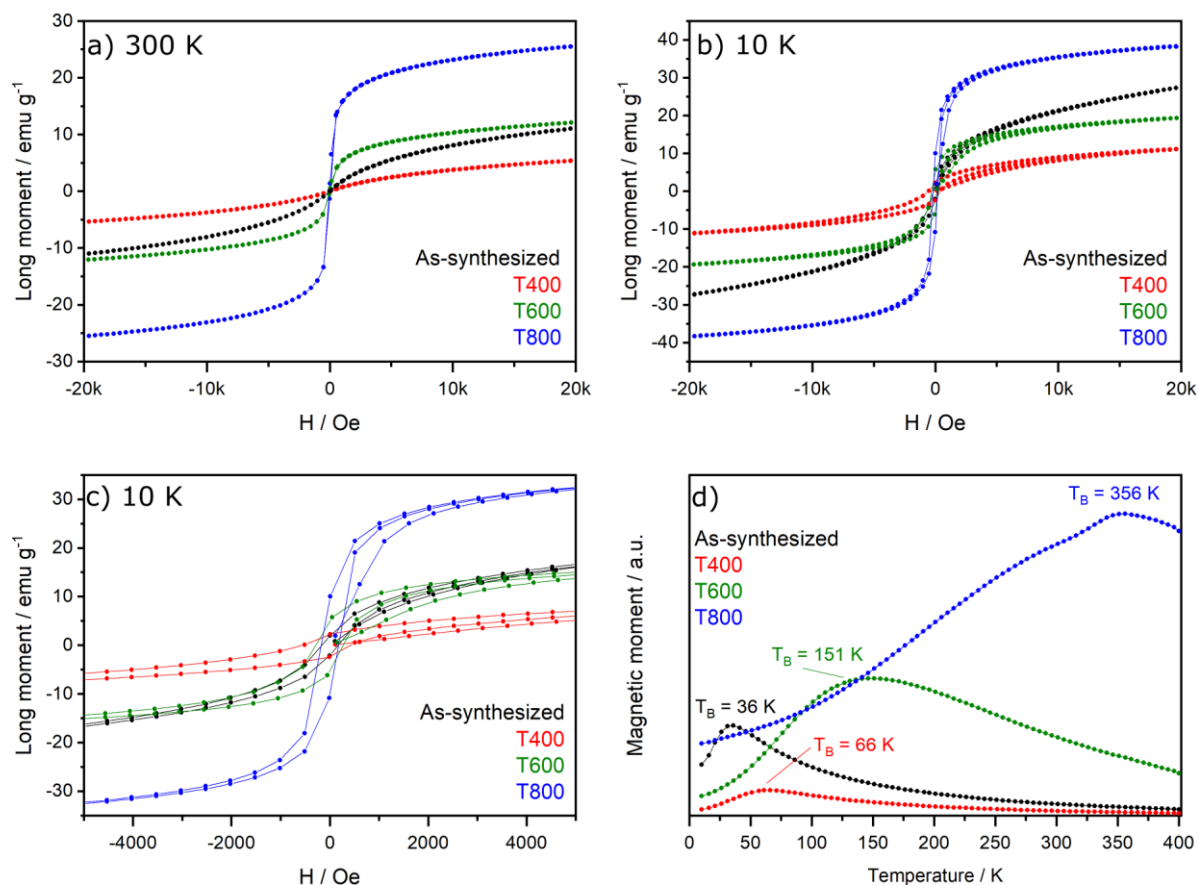


Figure 36: a) SUQID magnetization curves of MgFe₂O₄ nanoparticles at different calcination stages measured at 300 K. b) Magnetization curves collected at 10 K. c) enhanced view of the hysteresis region at 10 K. d) ZFCM measurement in a temperature range of 10–400 °C, with an applied external magnetic field of 100 Oe. a,b) adapted from *ACS Appl. Nano Mater.* **2020**, 3, 11587. Copyright (2020) American Chemical Society.

At 10 K, the enhanced magnetization of the as-synthesized particles is even more pronounced (Figure 36b,c). At this temperature, thermal activation does not suffice, to facilitate the rearrangement of the magnetic moments of the individual nanoparticles and consequentially hysteresis loops are observed for all calcination stages. The determined M_S are higher compared to the measurements conducted at 300 K, indicating that complete saturation was not reached at 20000 Oe. The blocking temperature T_B , at which the magnetic behavior changes from superparamagnetism to ferrimagnetism, was determined from ZFCM measurements at a constant external magnetic field of 100 Oe (Figure 36d). The position of the maximum in the respective magnetization curves hereby

represents T_B . The intensities of the maxima are in accordance with the trend observed for M_S . As expected, T_B raises with increasing calcination temperature and consequently with the size of the individual nanoparticles. Notably the maxima also get broader with higher calcination temperatures, due to the decreased homogeneity in particle size confirming the impression in the TEM images. The determined blocking temperatures are in accordance with Mössbauer spectroscopy, since the samples with a blocking temperature below 80 K did not show a magnetic sextet splitting in the respective spectra. The determined corrected saturation magnetizations and blocking temperatures for all calcination stages are summarized in Table 6.

Table 6: Saturation magnetization at 20 kOe and blocking temperatures of MgFe₂O₄ nanoparticles synthesized at different temperatures. The values for M_S are corrected for the diamagnetic mass loss that was determined by TGA.

Sample	$M_{S,corr}$ (300 K) / emu g ⁻¹	$M_{S,corr}$ (10 K) / emu g ⁻¹	T_B / K
As-synthesized	11.12	27.57	36
T400	5.41	11.18	66
T600	12.15	19.44	151
T800	25.48	38.33	356

4.2.4 Optical properties

Although it is claimed in several publications that the band gap of MgFe₂O₄ is located in the energy range of visible light, the material is in fact able to absorb NIR light as well. This could be demonstrated by diffuse reflectance spectroscopy showing a broad absorption feature between 900 and 1300 nm (Figure 37a). Going towards smaller wavelengths, the reflectance spectra of the MgFe₂O₄ nanoparticles demonstrate the absorption of light from the complete visible spectrum and up into the UV range. This is reflected in the Kubelka-Munk absorption spectra, that were calculated from the respective reflectance spectra (Figure A4, appendix).^[154] Due to the complex electronic structure, which is a consequence of the d⁵ electronic configuration of Fe³⁺, MgFe₂O₄ exhibits no steep absorption edge in the visible or UV region (in contrast to other semiconductors that are conventionally employed in heterogeneous photocatalysis). A semiconductor model assuming a fully delocalized VB/CB is therefore not suitable for the interpretation of the absorption spectrum of MgFe₂O₄. Consequentially, a conventional Tauc plot construction for the determination of the optical band gap is presumed to yield incorrect results, which is likely the reason for the large dissent among optical band gaps that can be found in the literature. Instead, the spectra must be treated as a superposition of absorption bands corresponding to individual local electronic transitions whose energies are defined by the crystal field orbital splitting and exchange splitting (see chapter 2.7).^[130] Figure 37b depicts the first derivative of

4.2 Material characteristics of MgFe₂O₄ nanoparticles with optimized stoichiometry

the diffuse reflectance spectra in the visible regime. For the T800 sample, the observed features suggest that at least three major excitations contribute to the absorption of visible light, which are located at 490 nm (2.53 eV), 570 nm (2.18 eV) and 655 nm (1.89 eV).

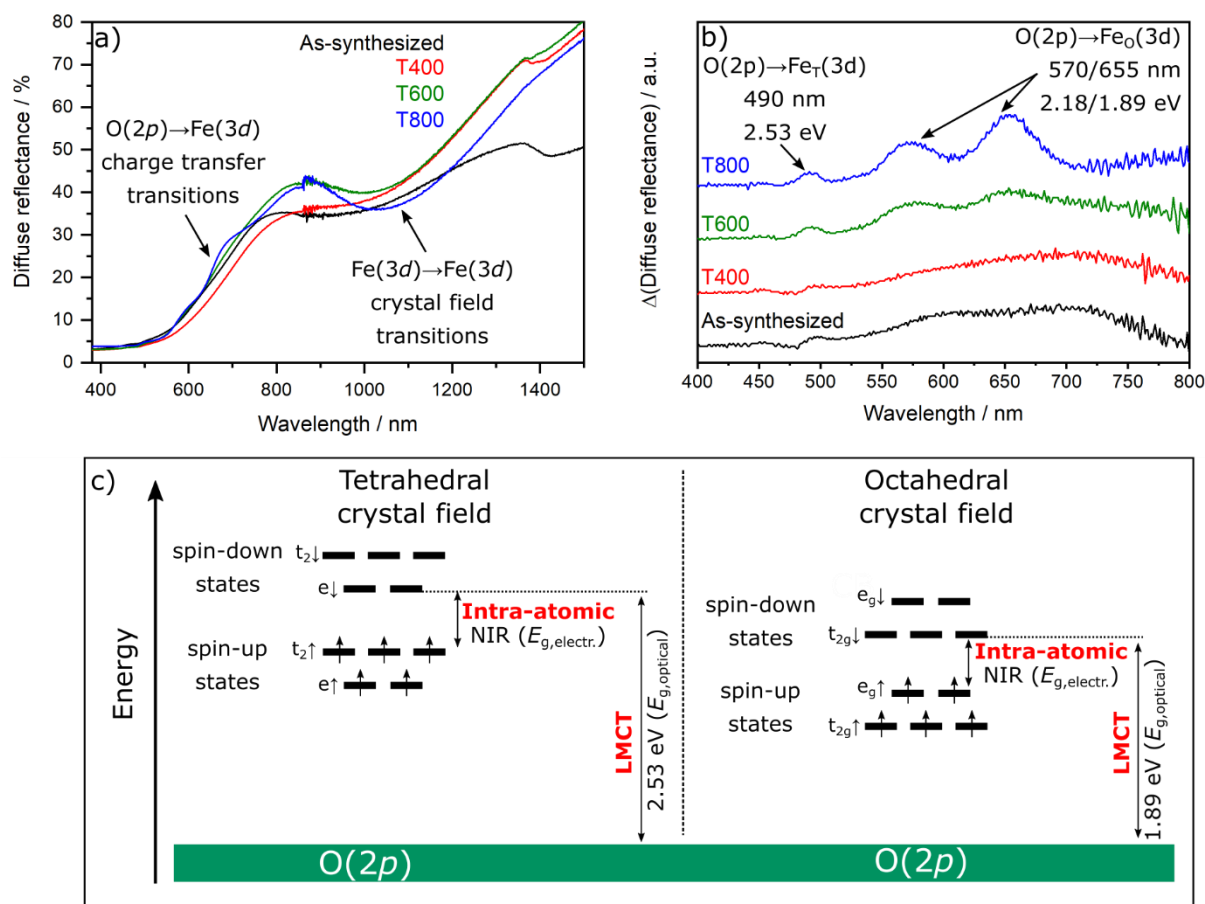


Figure 37: a) Diffuse reflectance spectra of MgFe₂O₄ nanoparticles at different calcination stages. b) First derivative of the diffuse reflectance spectra. The curves are offset for better clarity. c) Proposed schematic illustration of possible visible light and NIR mediated transitions for MgFe₂O₄ in the ground state. The higher energy of the spin-down states is a result of the exchange splitting that is correlated with spin pairing. a,b) adapted from *ACS Appl. Nano Mater.* **2020**, *3*, 11587. Copyright (2020) American Chemical Society.

In accordance with the works of Pailhé *et al.*^[179] and Granone *et al.*^[43], the visible light mediated excitations are exclusively attributed to O(2p) → Fe(3d) ligand-to-metal charge transfer (LMCT) transitions. The absorption bands at 655 nm and 570 nm are correlated to Fe³⁺ in octahedral coordination, while the feature at 490 nm belongs to tetrahedrally coordinated Fe³⁺. Different explanations for the occurrence of two octahedral absorption features can be found. Pailhé *et al.* ascribe this phenomenon to a distortion of the octahedral FeO₆ units, whereas Granone *et al.* attribute it to an exchange splitting effect in the case of ZnFe₂O₄.^[43,179] The NIR absorption is attributed to intra-atomic Fe(3d) → Fe(3d) crystal field transitions. From theory, such transitions are spin and parity forbidden for Fe³⁺ with d⁵ high-spin electronic configuration. The transitions become however allowed due to magnetic spin coupling between neighboring Fe³⁺ ions.^[43] Both the LMCT and the intra-atomic

crystal field excitations involve electronic transitions into the Fe³⁺ spin down states that constitute the CBM (For Fe³⁺ in tetrahedral and octahedral coordination those are e_g↓ or t_{2g}↓, respectively). The smaller energy of the intra-atomic crystal field excitation therefore suggests that the VBM of MgFe₂O₄ is composed of Fe(3d) spin-up crystal field states and not of states corresponding to the oxygen ligands. Due to the large width of the NIR absorption feature it cannot be resolved whether the VBM and CBM are located on the tetrahedral or the octahedral site. Nevertheless, its presence clearly implies that the electronic band gap is constituted exclusively by Fe³⁺ crystal field states and that it is considerably smaller than the band gap suggested by optical spectroscopy.

4.2.5 X-ray absorption and -emission characteristics

To confirm the interpretation of the optical spectra, X-ray absorption and -emission based characterization techniques were employed, to probe the electronic structure of MgFe₂O₄. Furthermore, a deeper insight into changes of the degree of inversion after thermal treatment should be gained from those measurements. To probe the CB states of MgFe₂O₄, the Fe(1s) absorption edge was measured by HERFD-XANES. The electronic structure of the VB was investigated by VtC-XES spectroscopy at the Fe Kβ_{2,5} fluorescence line.

The Fe(1s) HERFD-XANES spectra (Figure 38a) were collected over an incident energy range of 7090–7220 eV. The energy of the main absorption edge (which originates from Fe(1s)→Fe(4p) excitations) was determined to be 7121.7 eV from the first inflection point (Figure 38b).^[180] This way the absence of Fe₃O₄ could be confirmed, since the edge is expected to undergo an energetic shift towards smaller energy when Fe²⁺ is present in the sample.^[181] Indeed, such a shift could be observed for a Fe₃O₄ reference sample, whose main absorption edge was located 1.2 eV below that of MgFeO₄ (Figure 38d). This value is in good accordance with the shift expected for a sample where one third of the iron is in the Fe²⁺ oxidation state and the rest of the iron is present as Fe³⁺.

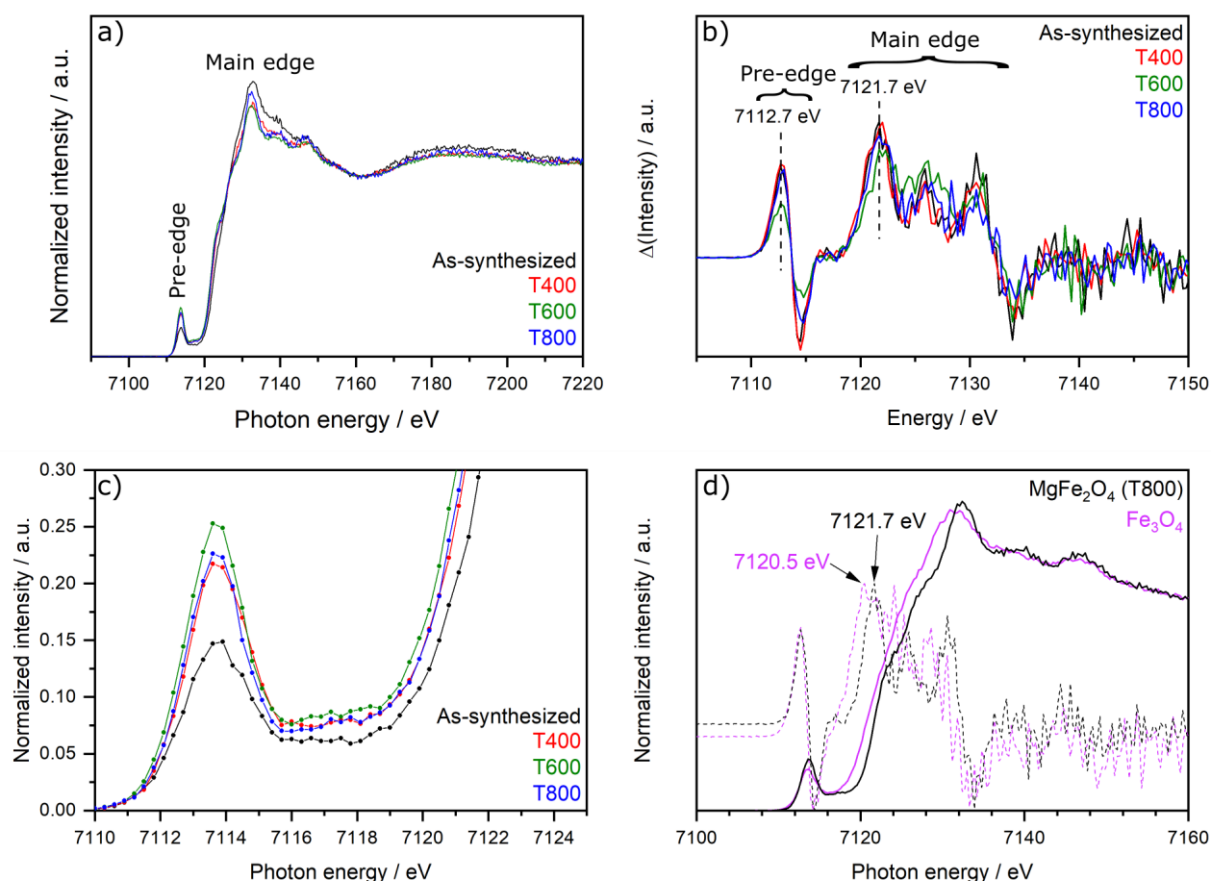


Figure 38: a) HERFD-XANES spectra of MgFe₂O₄ nanoparticles at different calcination stages. The spectra were normalized to the intensity at 7220 eV to account for differences in the concentration of the samples. b) First derivative of the XANES spectra. The maxima corresponding to the inflection points of the pre-edge and main edge are given. c) Enlarged depiction of the pre-edge region in the XANES spectrum. d) Comparison of the XANES spectra of MgFe₂O₄ and Fe₃O₄. For better clarity, only the spectrum of the T800 MgFe₂O₄ sample is shown. a, c, d) adapted from *ACS Appl. Nano Mater.* **2020**, 3, 11587. Copyright (2020) American Chemical Society.

Besides the main edge, a well-resolved pre-edge feature with a maximum at 7113.6 eV is observed in the spectra at all calcination stages (Figure 38c). The first inflection point of the pre-edge signal is located at 7112.7 for all samples, revealing a negligible influence of post-synthetic calcination on the energy of the unoccupied electronic states associated with the CB. Unlike the energetic position of the signal maxima, the intensities of the pre-edge signals show a strong dependency on the employed annealing temperature. Since the involved Fe(1s)→Fe(3d) transitions are highly susceptible to changes in the local environment of the Fe³⁺ centers, information on the degree of inversion can be drawn from the signal intensities. When Fe³⁺ is in tetrahedral coordination by four oxygen atoms, dipole transitions are facilitated due to a local mixing of 3d and 4p wavefunctions. In the case of iron in octahedral coordination such a hybridization effect does not occur due to the equivalent point-symmetry of the d-orbitals and the coordination sphere.^[182,183] The pre-edge intensities are expected to be considerably lower in the case of Fe³⁺ on octahedral sites, since only quadrupole excitations contribute to the pre-edge signal, which are lower in intensity by roughly two orders of magnitude.^[184] The intensity of the

pre-edge signal is therefore correlated to the fraction of iron on tetrahedral sites and can be used for a semi-quantitative estimation of the degree of inversion λ . The XANES spectra reveal that the as-synthesized sample exhibits the lowest degree of inversion, which is likely a consequence of the low crystallinity and random occupation of tetrahedral and octahedral sites during the quickly proceeding condensation during the microwave-assisted heating. A similar randomized cation ordering was already observed for ZnFe₂O₄ nanoparticles that were synthesized by microwave-assisted reaction.^[171] After calcination at 400 °C, the intensity of the pre-edge signal is significantly increased, suggesting a higher degree of inversion, which goes in line with the lower M_s observed by SQUID magnetometry (chapter 4.2.3). Since 400 °C is below the cation rearrangement temperature of roughly 500 °C, it is likely that this increase is caused by structural rearrangements in the direct vicinity of the iron centers, during the decomposition of precursor residues, instead of by ion migration.^[23] The increase of T_{Calc} to 600 °C leads to an increase of λ and upon a further increase of T_{Calc} to 800 °C, λ decreases again, in accordance with the observations by Antao *et al.*^[23] It has to be noted that the MgFe₂O₄ nanoparticles in this study were not quickly quenched to room temperature after the heating process, but instead were allowed to cool down slowly. Nevertheless, the time needed for the sample to cool below the cation rearrangement temperature is seemingly short enough for cation rearrangement processes to be considered negligible.

VtC-XES spectra (Figure 39a) recorded in an emission energy range of 7070–7140 eV could confirm the interpretation of the HERFD-XANES spectra. The spectra show three distinctive features: a $K\beta''$ satellite peak located at 7093 eV, the $K\beta_{2,5}$ main signal with a maximum in the range of 7108–7109 eV and a $KL\beta$ feature at 7120 eV, which will not further be discussed, as it is an artifact originating from Auger electron related multi-electron excitations.^[185] The Fe $K\beta''$ satellite peak is associated with $O(2s)\rightarrow Fe(1s)$ ligand-to-metal crossover transitions.^[156] The probability of such transitions is increased with shorter Fe-O bond length and a higher signal intensity therefore implies an increased fraction of iron in tetrahedral coordination.^[186] The observed trend for the different calcination stages follows the one observed in the XANES pre-edge spectra and therefore confirms that the T600 sample exhibits the highest degree of inversion. The Fe $K\beta_{2,5}$ VtC fluorescence line originates from $Fe(3d)\rightarrow Fe(1s)$ transitions that become allowed due to $O(2p)$ and $Fe(4p)$ contribution to the local $Fe(3d)$ wavefunction. The signal maxima are slightly shifted towards higher energies with increasing degree of inversion. Compared to the spectrum of $\alpha\text{-Fe}_2\text{O}_3$, which was taken as a reference, the signal maxima are shifted up to 0.4 eV towards higher energies, suggesting a more cathodic valence band (Figure 39b).

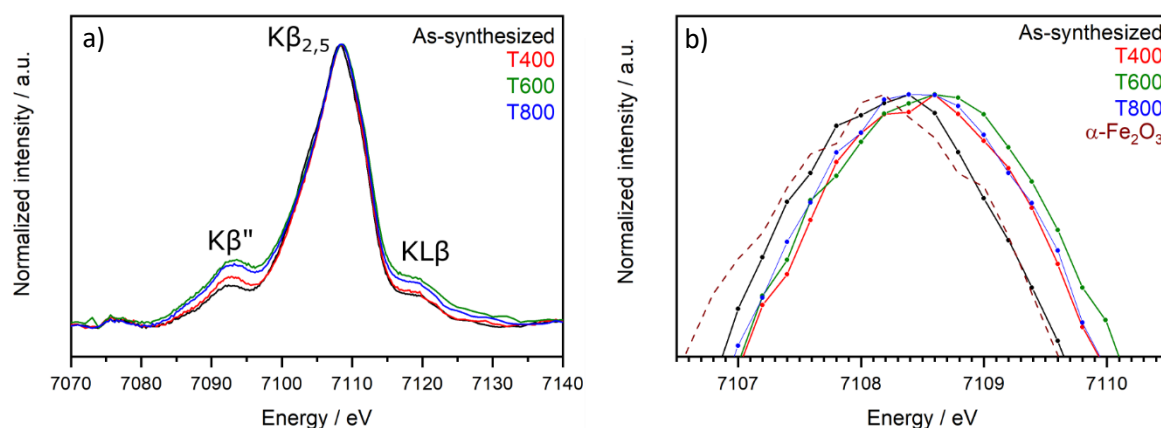


Figure 39: a) VtC-XES spectra of MgFe₂O₄ nanoparticles at different calcination stages. For better comparability, the exponential Kβ_{1,3} fluorescence background was removed (See figure A1, appendix), and the spectra were normalized according to the intensity of the Kβ_{2,5} maximum. b) Enhanced depiction of the Kβ_{2,5} maximum in the VtC-XES spectra of MgFe₂O₄ nanoparticles in comparison to α-Fe₂O₃. a,b) adapted from *ACS Appl. Nano Mater.* **2020**, 3, 11587. Copyright (2020) American Chemical Society.

The position of the high-energy side inflection points of the Kβ_{2,5} signal are associated with the energy of the VBM.^[187–190] The electronic band gap can therefore be estimated from the energetic distance between the Kβ_{2,5} VtC signal and the pre-edge in the XANES spectrum. (Figure 40)

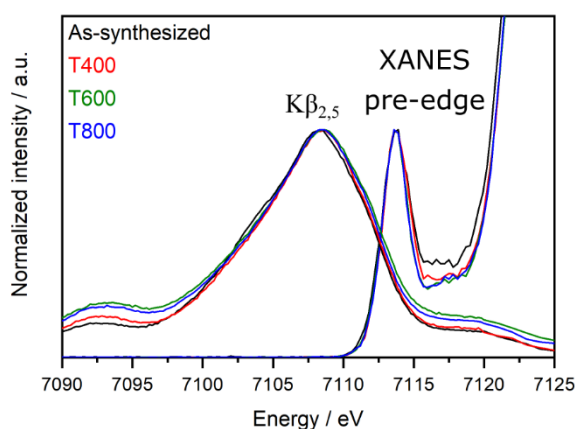


Figure 40: Combined depiction of the normalized Kβ_{2,5} VtC-XES and XANES pre-edge spectra, illustrating a large overlap between occupied and unoccupied states (adapted from *ACS Appl. Nano Mater.* **2020**, 3, 11587. Copyright (2020) American Chemical Society.).

Unlike measurements conducted on semiconductors that do not comprise elements with partly filled *d*-orbitals, the respective signals experience a significant overlap.^[189,190] Similar behavior can be observed in reports about other Fe³⁺ containing materials, despite being properly addressed by the authors of the respective study.^[188] The close proximity of occupied and unoccupied states provides an explanation for the significant NIR absorption observed in the diffuse reflectance spectra. Electronic band gaps ranging from 0.1 eV to 0.5 eV were determined from the distance between the high-energy

inflection point if the VtC signal and the low-energy inflection point of the XANES pre-edge signal (Figure 41). Those values are considerably smaller than the band gap of 1.89 eV that has been observed by optical spectroscopy, confirming that both the VCM and CBM are constituted by Fe(3d) crystal field states. Notably, a shoulder at an energy of 7110 eV can be observed in the all VtC derivative curves (best visible for the sample calcined at 800 °C), likely corresponding to O(2p) states involved in the visible light active LMCT excitations. The distance of this shoulder from the XANES pre-edge inflection point is in the range of 2 eV and therefore in good accordance with the observed visible light absorption of MgFe₂O₄. The employed combination of XANES and VtC-XES therefore confirms the interpretation of the optical spectra and calls for a strict differentiation between the optical and electronic band gap in the case of MgFe₂O₄.

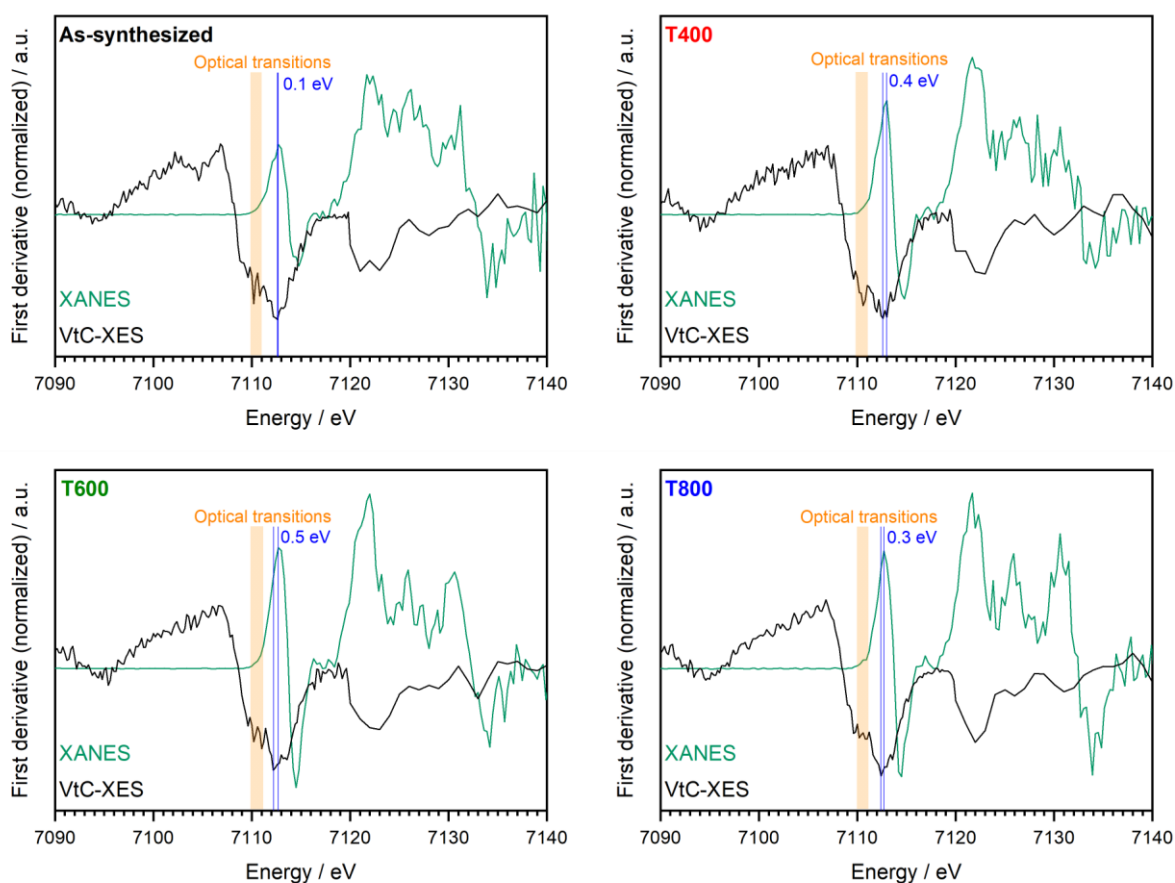


Figure 41: Determination of the electronic band gaps (given in blue) for MgFe₂O₄ nanoparticles at different calcination stages. The individual graphs depict the first derivatives of the XANES pre-edge region (green) and of the VtC K_{β2,5} signal (black), used for the determination of the respective inflection points. The electronic states responsible for the optically active transitions are highlighted in orange (adapted from *ACS Appl. Nano Mater.* **2020**, *3*, 11587. Copyright (2020) American Chemical Society.).

4.2.6 Photocatalysis and photoelectrochemistry

Regarding the application as a photocatalyst, only the visible light mediated LMCT excitations are of relevance, since the intra-atomic crystal field transitions do not facilitate charge carrier separation and therefore cannot be utilized in photocatalytic reactions.^[44] Since the target application of the material is visible light mediated photocatalysis, this is not necessarily a problem. Nevertheless, the MgFe₂O₄ nanoparticles did not show any activity in the reduction of protons from an aqueous solution of MeOH, or in overall water splitting using visible light. The application for other reductive tasks, like the reduction of 2,6-dichloroindophenol, proved unsuccessful as well. The inactivity in reductive reactions is attributed to the low electronic conductivity of the material that (despite the short diffusion pathways that are ensured by the nanoparticle morphology) seemingly prevents the diffusion of excited electrons to the reaction sites on the particle surface. The low mobility of excited electrons is related to the spin polarization of the involved $e\downarrow$ and $t_{2g}\downarrow$ CBM states, which causes a strong localization of the electron on the Fe³⁺ center. Additionally, an ultra-fast self-trapping of excited electrons *via* the formation of a small polaron has been reported for materials containing elements with d^n electronic configuration, like it is the case in ferrites.^[39,191] No degradation of RhB was observed under irradiation with visible light in the presence of phase-pure MgFe₂O₄ nanoparticles, which is in conflict with previous reports.^[90] A possible explanation for this is the iron oxide impurity present in the literature example, which might facilitate charge carrier separation and migration. Nevertheless, the introduction of an internal electric field by deposition of Rh or Pt co-catalysts *via* photodeposition or wet impregnation did not induce any activity in photocatalytic test reactions. The small size of the MgFe₂O₄ nanoparticles might however result in an unfavorable coverage with the co-catalyst and the co-catalyst deposition therefore must be further investigated and optimized.

Due to the nanoparticle morphology, the preparation of MgFe₂O₄ photoelectrodes proved challenging using the spray coating process described in chapter 3.7. Electrodes prepared this way experienced considerable surface effects preventing the formation of a defined space charge layer and therefore the determination of a flat band potential was not possible. For a detailed photoelectrochemical characterization of MgFe₂O₄, the reader is therefore referred to the work of Henning *et al.*, where the photoelectrochemical properties of MgFe₂O₄ thin-films prepared by pulsed-laser deposition were investigated.^[97] Using those photoelectrodes, it was revealed that MgFe₂O₄ behaves like an n-type semiconductor with a flat band potential located at +0.67 V vs. RHE. Furthermore, the generation of a photocurrent could be demonstrated when the photoelectrode was illuminated with visible light in the presence of Na₂SO₃ acting as hole scavenger. The achieved photocurrent densities were very low, since the detrimental effects of ultra-fast polaron trapping and high electric resistivity also apply in the case of a photoelectrochemical cell. Nevertheless, it could be demonstrated, that the excited charge

carriers to some degree could be utilized for the conversion of solar energy, when the influence of the unfavorable charge migration characteristics were diminished by the application of an external electric field.

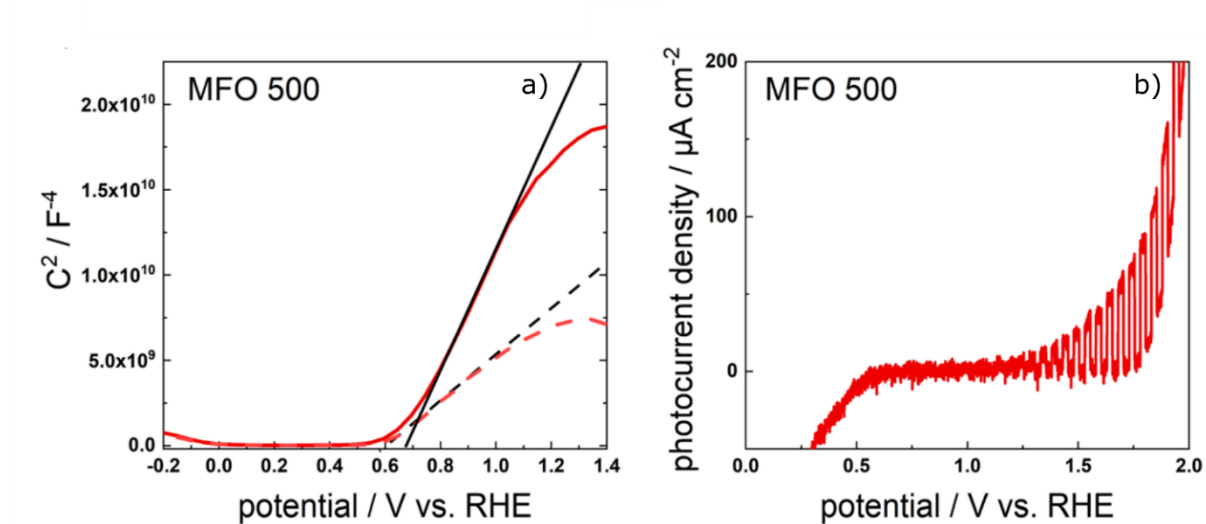


Figure 42: a) Mott-Schottky plot of a PLD derived MgFe₂O₄ thin film electrode measured under dark (solid line) and illuminated (segmented line) conditions. b) Photocurrent density of the respective electrode measured under chopped-light voltammetry conditions upon irradiation with visible light. a,b) reprinted from [97], Copyright (2020) American Chemical Society.

4.3 The microwave-assisted synthesis of other spinel ferrites

Since the divalent metal cations of many known spinel ferrites are available as acetylacetonates, it was tempting to investigate, whether the microwave-assisted synthesis for MgFe₂O₄ could be adapted for the synthesis of other spinel ferrites. A respective synthesis for ZnFe₂O₄ nanoparticles was already published by Suchomski *et al.*^[171] During the course of this work, first attempts were made towards the microwave-assisted synthesis of NiFe₂O₄ and MnFe₂O₄. Basic characterization data for the obtained products are briefly discussed in the following chapter.

4.3.1 NiFe₂O₄

Magnetic NiFe₂O₄ nanoparticles were synthesized in a temperature range of 200–275 °C for 30 min in the microwave. PXRD patterns and Raman spectra (Figure 43) are in good accordance with the literature.^[192,193] The widths of the Bragg reflections reveal that the crystallite size is strongly influenced by the employed microwave temperature. This observation differs from the findings made in the synthesis of MgFe₂O₄, where the microwave temperature had only a negligible influence on the crystallite size.

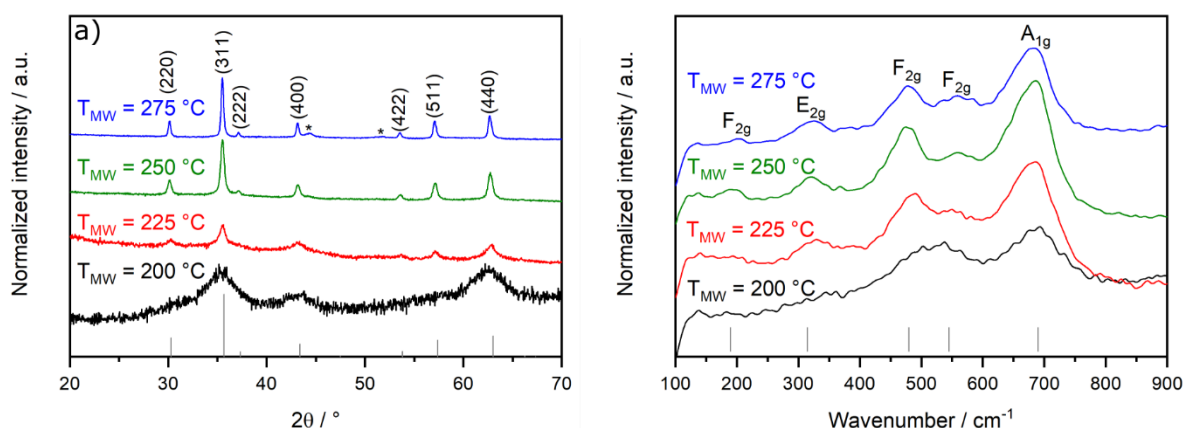


Figure 43: a) PXRD pattern of as-synthesized NiFe_2O_4 nanoparticles obtained at different microwave temperatures. The metallic nickel impurity in the sample synthesized at 275 °C is indexed by an asterisk. b) Raman spectra of the respective NiFe_2O_4 nanoparticles. References for the diffraction pattern and Raman spectrum are given in grey.^[192,193]

Particles synthesized at 200 °C are mostly amorphous and only very weak and broad reflexes belonging to a spinel structure can be identified in the diffraction pattern. An increase of the temperature to 225 °C already leads to an increase of crystallinity and at a synthesis temperature of ≥ 250 °C, a highly crystalline material is obtained. The respective crystallite sizes and EDX derived Ni:Fe cation ratios are summarized in Table 7.

Table 7: Elemental composition and crystallite sizes of NiFe_2O_4 nanoparticles synthesized via microwave-assisted reaction at different temperatures.

$T_{\text{MW}} / ^\circ\text{C}$	Ni:Fe	$d_{\text{Crystallite}} / \text{nm}$
200	0.54	-
225	0.50	9.7
250	0.49	18.5
275	0.59	24.5

At a microwave temperature of 275 °C, a reduction of Ni^{2+} to metallic Ni during synthesis is indicated by additional reflections in the PXRD pattern of the product. Furthermore, with 0.59 the Ni:Fe cation ratio in the sample synthesized at 275 °C is above that of an ideal spinel structure, while nanoparticles with close to ideal stoichiometry are obtained at the lower microwave temperatures (Table 7, see Figure A5 in the appendix, for an exemplary EDX spectrum of NiFe_2O_4 nanoparticles). The reduction of Ni^{2+} is accompanied by considerably increased pressures in the reaction vessel, since metallic nickel is very susceptible to microwave radiation and its presence facilitates the intake of radiative energy. This phenomenon could be confirmed optically *via* the built-in camera of the microwave reactor showing small metallic Ni shards glowing in red. This behavior implies an inhomogeneous temperature

distribution in the microwave solution with hot spots of considerably higher temperature compared to the average temperature of the solution, which was monitored by an IR sensor. Presumably, these hot spots facilitate the crystallization of the spinel phase, as soon as metallic Ni nuclei are formed in the solution. No indication for the presence of metallic Ni was found in the PXRD patterns of nanoparticles synthesized at 250 °C or below. However, the formation of traces of metallic Ni cannot be ruled out and would explain the strong temperature dependence of the crystallinity. The reduction of Ni²⁺ prevents a precise control over the temperature inside the reaction vessel, and therefore negatively influences the reproducibility of the syntheses. The suitability of the microwave-assisted route for the production of NiFe₂O₄ nanoparticles is therefore presumed limited at the moment. A systematic investigation on the calcination behavior of NiFe₂O₄ synthesized by this microwave-assisted route was not conducted and remains to be done in the future.

4.3.2 MnFe₂O₄

The modified synthesis for MnFe₂O₄ yielded a dark brown magnetic powder with a Mn:Fe ratio of 0.52 (See Figure A6 in the appendix for an exemplary EDX spectrum). The PXRD pattern (Figure 44) of the as-synthesized particles reveals the presence of a cubic spinel phase, indicating a successful synthesis of MnFe₂O₄. However, while the diffraction pattern is in reasonable accordance with the reference for MnFe₂O₄ (ICDD 01-073-1964), the Bragg reflections are slightly shifted towards a higher 2 θ -angle. Therefore, they can also be indexed according to the reference pattern for Fe₃O₄ (ICDD 00-001-0449). After calcination at 400 °C for one hour (rate: 10 K min⁻¹) this shift becomes even more pronounced, and the positions of the Bragg reflections are in very good accordance with the reference for Fe₃O₄. A further increase of the calcination temperature leads to a decomposition of the spinel and after calcination at 800 °C, a mixture of α -Fe₂O₃ and MnFeO₃ is obtained, suggesting the oxidation of Mn²⁺ to Mn³⁺ during thermal treatment in air. An oxidation in this temperature range is known for other manganese oxides. For example, MnO is oxidized to Mn₂O₃ at a temperature of 250–300 °C, which is then again oxidized to Mn₃O₄ at 1000°C.^[134] The possibility for the divalent cation to change its oxidation state might be an explanation for the lesser thermal stability of MnFe₂O₄ compared to other spinel ferrites.

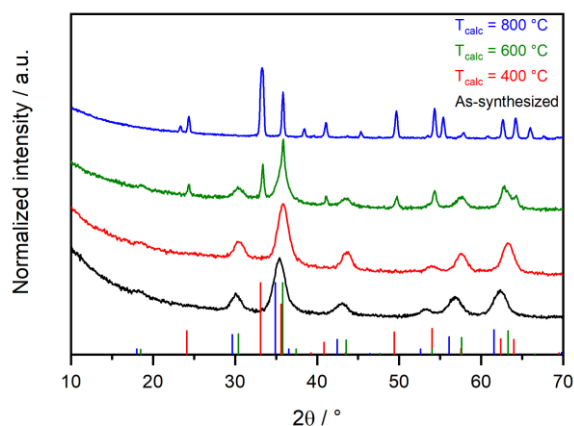


Figure 44: XRD pattern of MnFe₂O₄ nanoparticles calcined at different temperatures. References are given for MnFe₂O₄ (blue, ICDD 01-073-1964), Fe₃O₄ (green, ICDD 00-001-0449) and α-Fe₂O₃ (red, 01-084-0306)

TEM images of the as-synthesized sample confirm the synthesis of nanoparticle agglomerate forming nanoparticles (Figure 45). The individual nanoparticles are roughly 5 nm in diameter, which is comparable to the particles formed in the MgFe₂O₄ synthesis.

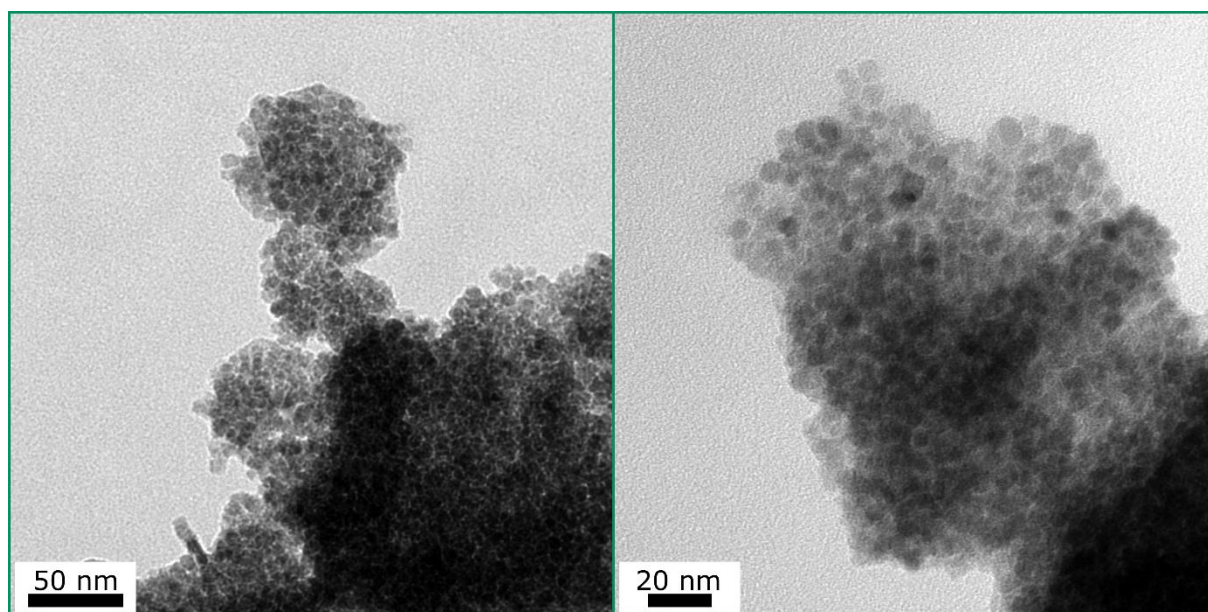


Figure 45: TEM images of as-synthesized MnFe₂O₄ nanoparticles.

Since the spinel phase decomposes above 400 °C, SQUID magnetometry curves were only measured of the as-synthesized sample and of the sample calcined at 400 °C (Figure 46,a-c). Compared to MgFe₂O₄, the MnFe₂O₄ nanoparticles show an increased saturation magnetization at an applied external magnetic field of 20000 Oe. This is not unexpected, due to the presence of additional unpaired electrons that are introduced by Mn²⁺, which has d⁵ high-spin electronic configuration.^[194] Notably, a decrease of the saturation magnetization after calcination can be observed, similar to the observations

made for the MgFe_2O_4 nanoparticles. Changes of the degree of inversion should have a negligible effect on the saturation magnetization due to the isoelectronic configuration of the A and B cations in MnFe_2O_4 . Hence, the higher M_S of the as-synthesized sample is likely a consequence of the weakly pronounced long-range ordering preventing an antiparallel alignment of spin magnetic moments, similar to the situation in MgFe_2O_4 .

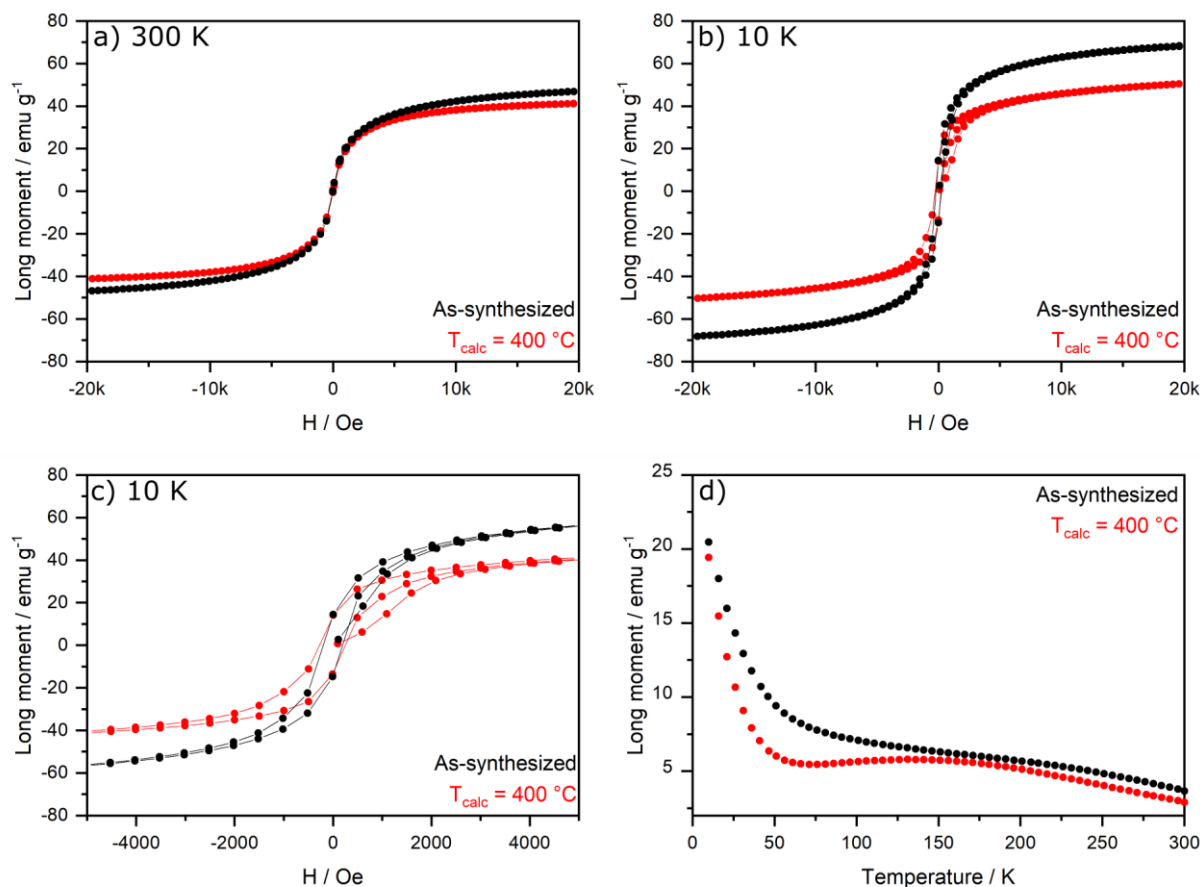


Figure 46: a) SUQID magnetization curves of MnFe_2O_4 nanoparticles before and after calcination at 400 °C, measured at 300 K. b) Magnetization curves collected at 10 K. c) enhanced view of the hysteresis region in the 10 K measurement. d) ZFCM measurement in a temperature range of 10–300 K, with an applied external magnetic field of 100 Oe.

The magnetization curve collected at 10 K shows a hysteresis, while the one collected at room temperature does not, implying that the particles are superparamagnetic at room temperature. Nevertheless, the ZFCM curve of the as-synthesized sample exhibits no maximum corresponding to a blocking temperature (Figure 46d). The reason for that is not clear, however it might be possible that T_B is located below 50 K and the maximum is simply not resolved in the respective measurement. For the sample calcined at 400 °C a broad feature can be observed, indicating a blocking temperature in the range of 100–200 K, which is considerably higher than T_B of MgFe_2O_4 nanoparticles after equal

thermal treatment. A likely explanation for this is the low temperature stability of MnFe_2O_4 , which might lead to sintering between individual nanoparticles at comparably low calcination temperatures.

4.4 The microwave-assisted synthesis of macroporous CaFe_2O_4

Since crystal structure and electronic properties of calcium ferrite have been reported to considerably differ from the material characteristics of the spinel ferrites, CaFe_2O_4 was considered a promising alternative to MgFe_2O_4 for photocatalytic applications. Especially the reported CBM, which is located at -0.6 V vs. RHE and the band gap of 1.9 eV suggest that hydrogen reformation under visible light should be easily possible using this material. Since reports about the synthesis of nanostructured CaFe_2O_4 are scarce, it should be investigated if the microwave-assisted synthesis route offers a pathway towards the synthesis of CaFe_2O_4 nanostructures.

4.4.1 Synthesis approaches for CaFe_2O_4

Due to the weak solubility of $\text{Ca}(\text{acac})_2$ in 1-phenylethanol, which prevented a complete dissolution of the precursor, it was not possible to directly adapt the synthesis for MgFe_2O_4 nanoparticles to produce CaFe_2O_4 . Sonication of the suspension at an elevated temperature of $60\text{ }^\circ\text{C}$, or an additional microwave heating step at $100\text{ }^\circ\text{C}$ for 15 min prior to the condensation above $200\text{ }^\circ\text{C}$ could not circumvent this problem. All synthesis approaches based on acetylacetonates yielded reaction products with a Ca:Fe cation ratio significantly lower than the ideal value of 0.5. Consequentially, $\alpha\text{-Fe}_2\text{O}_3$ was always formed as the main crystal phase upon calcination in air.

An alternative microwave synthesis route therefore had to be developed for the production of phase-pure CaFe_2O_4 . During the development of the synthesis, approaches based on the composition of $\text{Ca}(\text{OAc})_2 \cdot \text{H}_2\text{O}$ and $\text{Fe}(\text{NO}_3)_3 \cdot 9\text{H}_2\text{O}$ in 1,4-butanediol produced the most promising results. A microwave temperature of $300\text{ }^\circ\text{C}$ yielded a brown powder with an ideal Ca:Fe ratio of 0.5 (See Figure A7 in the appendix for an exemplary EDX spectrum), when $\text{Ca}(\text{OAc})_2$ was employed with a small stoichiometric excess of 10%. The yielded powder did however not contain any of the orthorhombic CaFe_2O_4 phase, which is likely a consequence of the complex phase diagram of the Ca-Fe-O system and the high activation barrier that needs to be overcome for the formation of the target phase.^[111,115] PXRD revealed that the obtained powder was instead composed of a mixture of CaCO_3 and Fe_3O_4 (Figure 47a). The diffraction pattern of the spinel exhibits a texture indicating the growth of this phase in a preferred crystallographic direction. This is best visible for the (440) reflection at $63^\circ 2\theta$, which is much sharper than the other spinel reflections. By thermal annealing of this powder at $900\text{ }^\circ\text{C}$ for one hour under air, phase-pure CaFe_2O_4 with orthorhombic crystal structure (Space group No. 62, $Pnma$) and an average crystallite size of 49 nm (averaged from the FWHM of the (210), (220) and (211)

reflections) was obtained. The Raman spectrum of the calcined sample shows no indication of a by-phase and all observed bands are in good accordance with the literature for CaFe_2O_4 (Figure 47b).^[195]

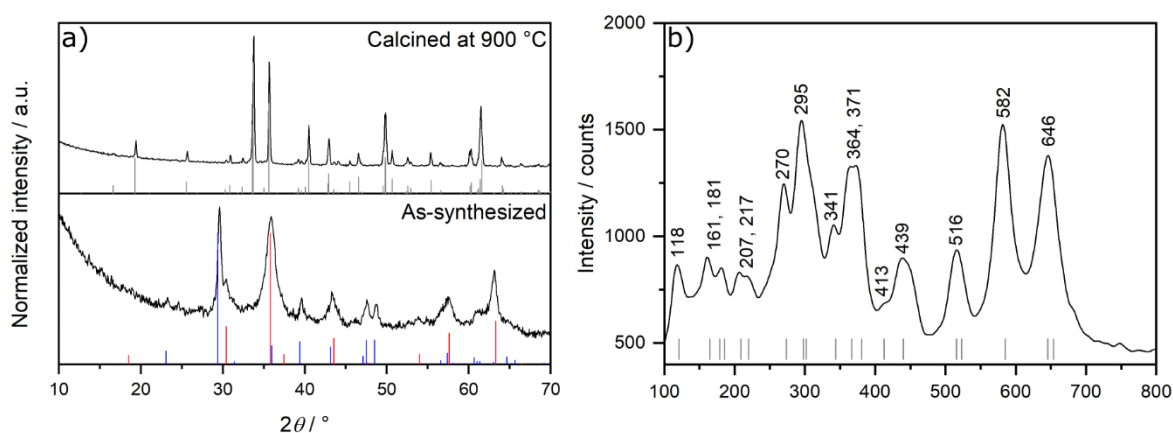


Figure 47: a) Diffraction pattern of the powder obtained after microwave synthesis and after calcination at 900 °C for one hour. References are given for CaFe_2O_4 (grey, ICDD 01-074-2136), Fe_3O_4 (red, ICDD 01-075-0449) and CaCO_3 (blue, ICDD 01-081-2027). b) Raman spectrum of CaFe_2O_4 after calcination at 900 °C. The reference is given in grey.^[195]

The homogeneous distribution of nanocrystalline CaCO_3 and Fe_3O_4 in the microwave derived powder likely facilitates the formation of CaFe_2O_4 and allows for lower calcination temperatures and shorter reaction times compared to SSR.^[116] In contrast to the highly sintered products obtained by SSR, the product synthesized *via* calcination of the microwave product exhibited a distinct sponge-like macropore structure as revealed by SEM (Figure 48). The macroporous morphology is considered beneficial regarding the application in photocatalysis and photoelectrochemistry. It offers a good balance between short diffusion pathways for photoexcited charge carriers and low concentration of defect recombination sites, due to the high crystallinity. The formation of a macroporous structure was not expected, since no templating reagent was employed during synthesis and because of the high calcination temperature that was required (despite being lower than the temperatures necessary for SSR). The morphology of the product was therefore investigated at different temperature stages to gain further insight into the formation of the pore structure.

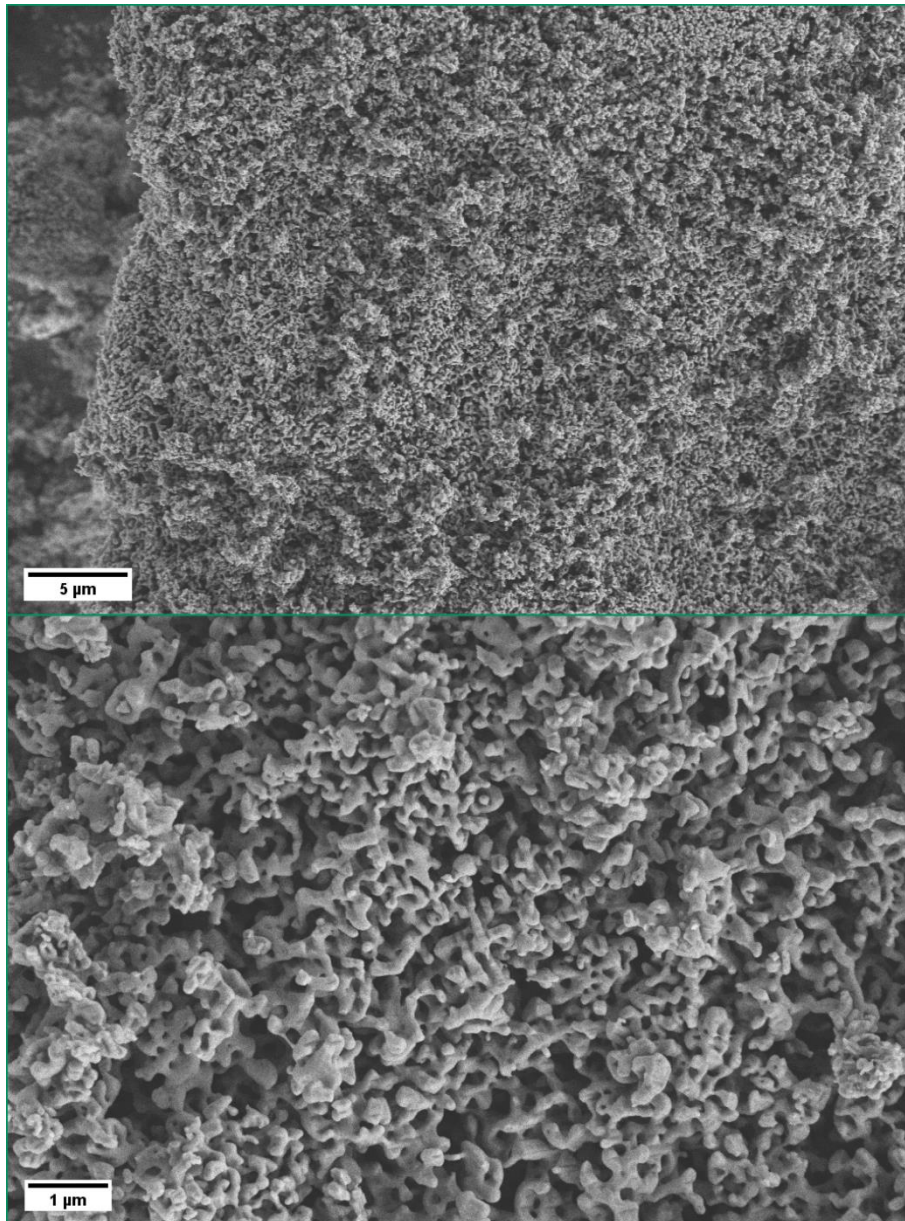


Figure 48: SEM images of macroporous CaFe_2O_4 sponge structures.

4.4.2 Formation pathway of macroporous CaFe_2O_4

Temperature dependent *In-situ* PXRD (Figure 49) implies a constantly changing phase composition during heating of the microwave product under air. The observed phase transitions involve the presence of several crystalline phases. The phase composition of the as-synthesized powder is stable up to a temperature of 600 °C. Further heating to 620 °C results in the decomposition of CaCO_3 , which is confirmed by thermogravimetric analysis showing a mass loss of roughly 10% in the respective temperature regime (Figure 50). It is presumed that traces of a persistent carbonate species might play a role in the formation of the macropore structure, even at higher temperatures. Carbonates are known to have a stabilizing effect on nanostructures, which was for example demonstrated in the

synthesis of $\text{Ba}_5\text{Ta}_4\text{O}_{15}$ layered perovskite nanofibers, where trace amounts of a residual carbonates could be identified even after calcination at $900\text{ }^\circ\text{C}$ for 10 hours.^[196]

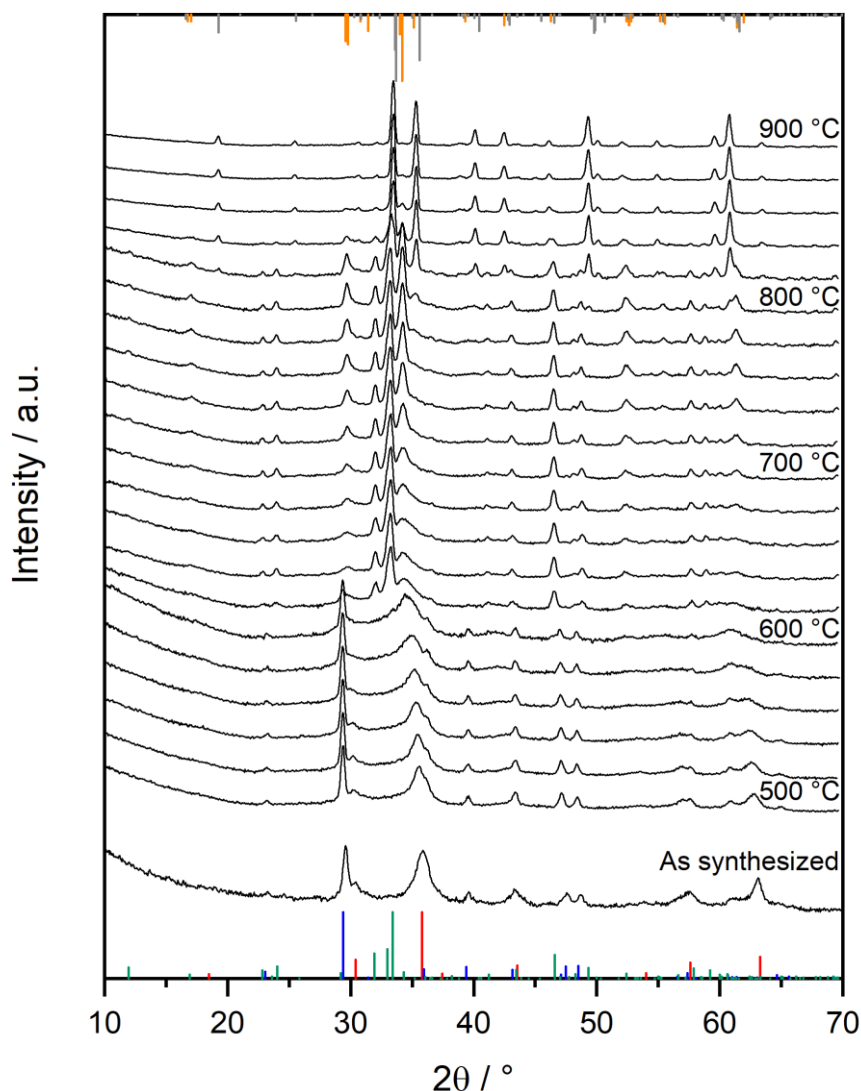


Figure 49: In-situ PXRD patterns revealing changes of the phase composition during heating of the $\text{CaCO}_3/\text{Fe}_3\text{O}_4$ precursor powder in the synthesis of macroporous CaFe_2O_4 . References are given for Fe_3O_4 (red, ICDD 01-075-0449), CaCO_3 (blue, ICDD 01-081-2027), $\text{Ca}_2\text{Fe}_2\text{O}_5$ (green, ICDD 01-071-2264), $\text{Ca}_4\text{Fe}_{14}\text{O}_{25}$ (orange, ICDD 00-013-0343), CaFe_2O_4 (grey, ICDD 01-074-2136)

After the decomposition of CaCO_3 , the calcium-rich $\text{Ca}_2\text{Fe}_2\text{O}_5$ phase is formed, which crystallizes in the orthorhombic brownmillerite structure (Space group No. 62, $Pnma$). The stoichiometry of the starting material prescribes that a calcium deficient species must be present at the same time. Indeed, when the temperature is further increased, reflections emerge that can be indexed according to the calcium-deficient, rhombohedral $\text{Ca}_4\text{Fe}_{14}\text{O}_{25}$ phase (Space group No. 167, $R\bar{3}c$). Above $800\text{ }^\circ\text{C}$ the target phase CaFe_2O_4 starts to form and at $900\text{ }^\circ\text{C}$ phase-pure, orthorhombic CaFe_2O_4 is obtained. The phase

rearrangements during the heating process are confirmed by DSC showing a positive differential voltage, which suggests ongoing endothermic processes in a temperature regime of 650–900 °C, where no mass loss is observed (Figure 50).

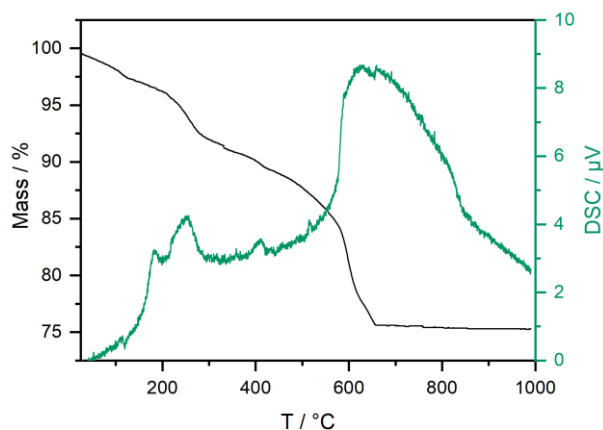


Figure 50: Temperature-induced mass loss (black) and DSC differential voltage (green) of the CaFe₂O₄ microwave product in a temperature range from room temperature to 1000 °C in air.

The composition of the as-synthesized powder was further investigated by TEM (Figure 51). CaCO₃ and Fe₃O₄ phases were identified by the visible lattice planes. After the microwave synthesis, Fe₃O₄ exhibits a nanorod morphology in agreement with the observed texture in the PXRD pattern.

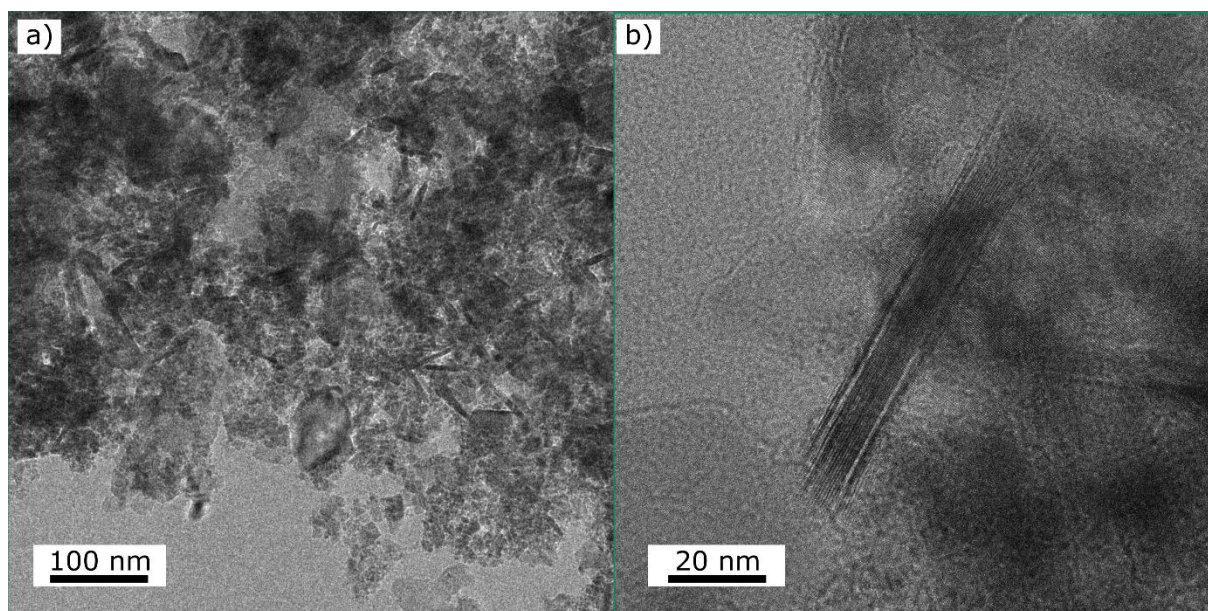


Figure 51: a) TEM image of the nanocrystalline mixture of CaCO₃ and Fe₃O₄ used in the synthesis of macroporous CaFe₂O₄. b) TEM image illustrating the nanorod morphology of Fe₃O₄ in the respective sample.

Below 600 °C, no significant changes of the morphology are observed and consequentially the Fe₃O₄ nanorods are still present after calcination at 600 °C for one hour (Figure 52e). Calcination at higher

temperatures changes the morphology, as was expected, due to mass loss and crystal phase transformations. In the sample that was calcined at 700 °C for one hour, no Fe_3O_4 nanorods can be identified anymore and a further increase on the calcination temperature is accompanied by the growth of crystallites which form nanostructured aggregates. This process continues up to a calcination temperature of 900 °C.

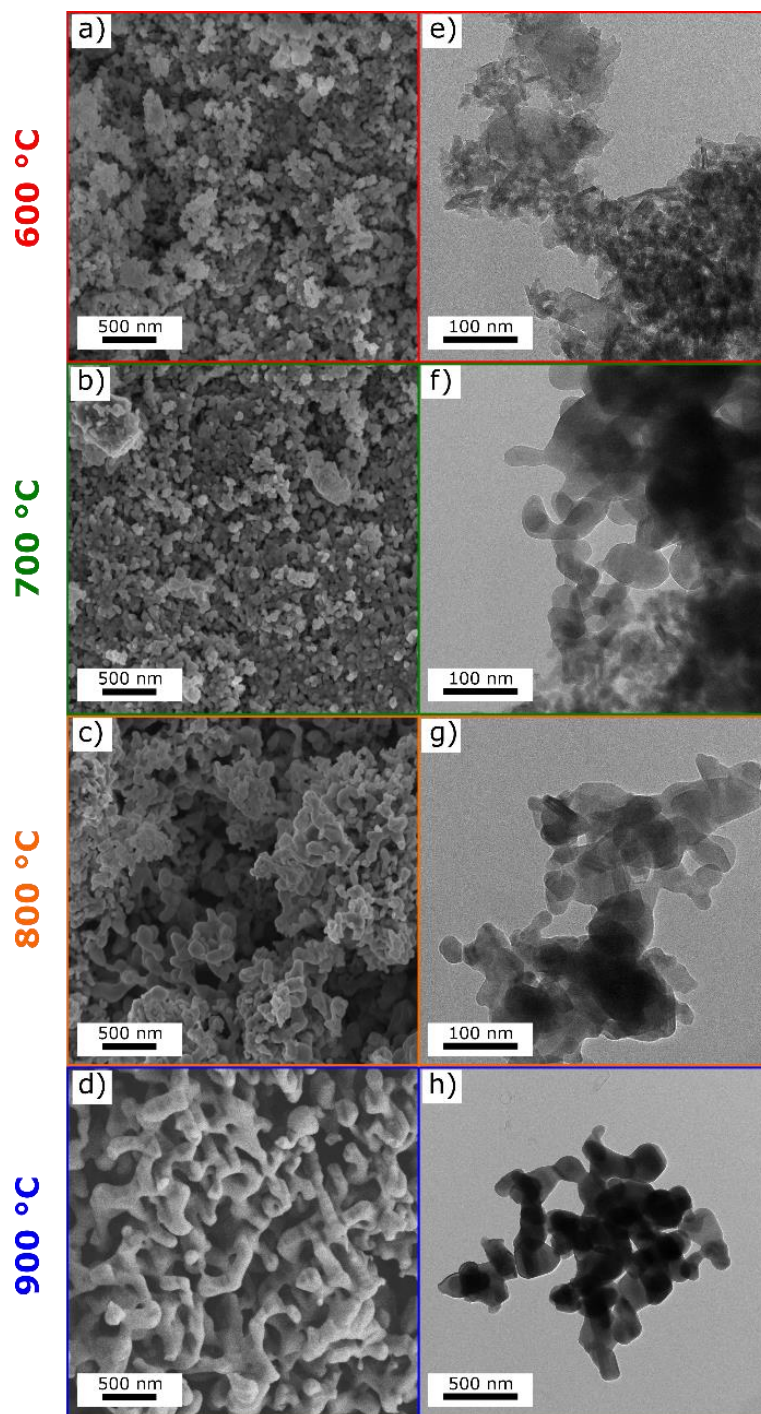


Figure 52: SEM (a–d) and TEM (e–h) images of CaFe_2O_4 illustrating the formation of the pore network upon calcination at temperatures of 600–900 °C.

The morphology changes observed by electron microscopy are reflected in the N₂-physorption isotherms (Figure 53,a–b) and mercury intrusion porosimetry experiments (Figure 53,c–d). N₂-physorption suggests that interparticular voids corresponding to the mesopore regime are already present in the as-synthesized powder. The formation of such voids is likely a consequence of the magnetic nature of the Fe₃O₄ nanorods, which facilitates their agglomeration. Above 600 °C, the agglomerated particles undergo sintering processes leading to a decrease of the BET surface area and to a shift of the pore size distribution towards the macropore regime. Notably, while the average pore volume is systematically increased with each increase of the calcination temperature, the cumulative pore volume corresponding to the macropore system remains nearly constant at a value of 0.5 cm³ g⁻¹. This observation indicates that the morphology changes are driven by the thermodynamic minimization of surface energy through the consumption of smaller pores in favor of the growth of larger pores. Simultaneously, the temperature induced phase transitions prevent the growth of large crystallites and therefore stabilize the pore network additionally to the proposed presence of carbonate residues.

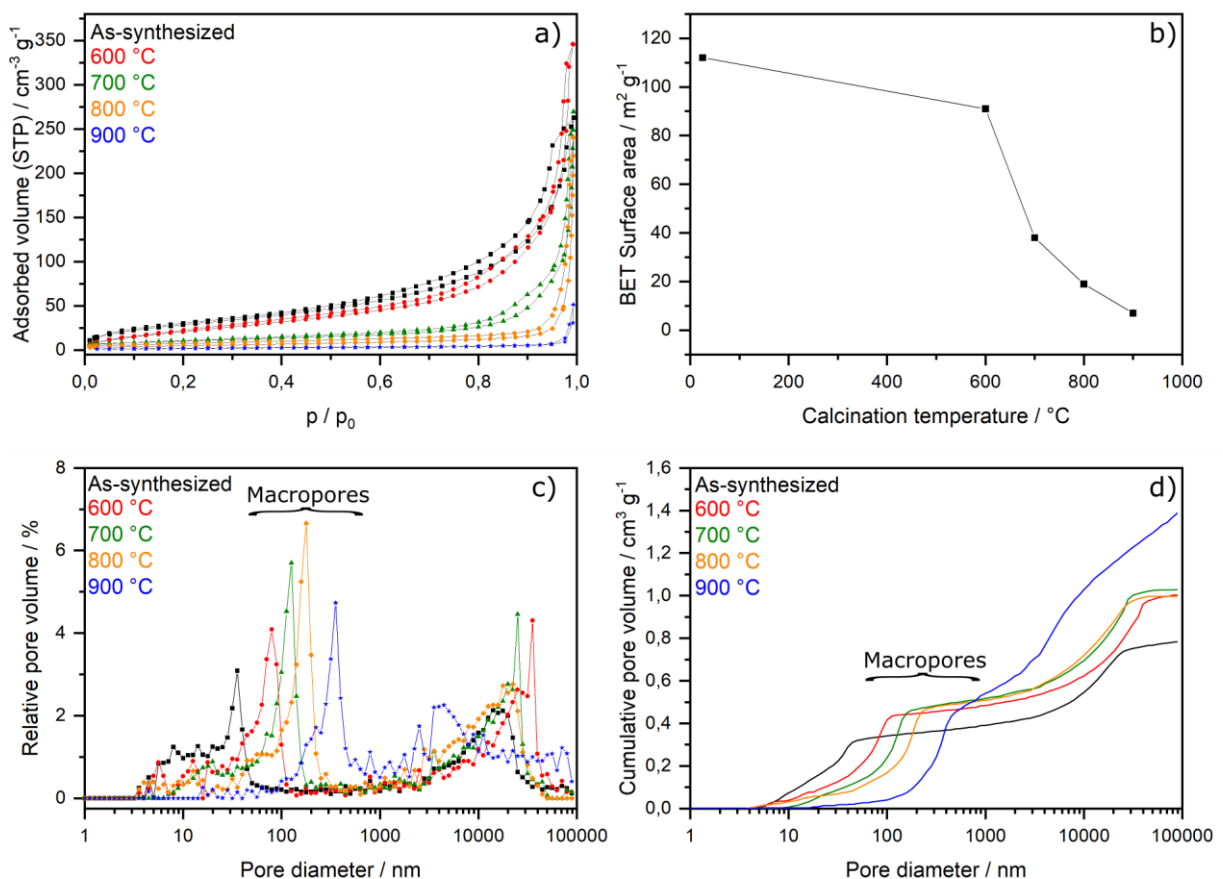


Figure 53: a) N₂-physorption isotherms of CaFe₂O₄ powders synthesized by microwave reaction and calcined for one hour at different temperatures. b) BET surface areas calculated from the respective physorption isotherms. c) MIP derived pore size distribution. d) Cumulative pore volume of the pore network, derived from the MIP experiment.

The phase-pure CaFe₂O₄ sponge structures exhibit a low BET surface area of 7 m² g⁻¹, which is however still higher than the values determined for samples synthesized by SSR.^[117] The pore size distributions that were derived from the MIP data, imply a macropore system with pore diameters in a range of 100–1000 nm (393 nm in average). The structure exhibits a cumulative pore volume of 1.4 cm³ g⁻¹, of which 0.5 cm³ g⁻¹ correspond to the macropore system and 0.9 cm³ g⁻¹ originate from cavities between individual macroporous particles.

4.4.3 Magnetic properties

Zero-field, room temperature Mössbauer spectroscopy (Figure 54a) was employed to probe the magnetic hyperfine structure of macroporous CaFe₂O₄. The spectrum of the as-synthesized sample shows a sextet, indicating a permanent magnetic moment. This is a confirmation for the presence of Fe₃O₄ in the as-synthesized sample, which was observed as nanorods in the TEM images. The two individual sextet spectra that would be expected from an inverse spinel structure could not be resolved, due to the weak and broad signals, which are a consequence of the small size and large surface-to-volume ratio of the nanorods. After calcination of the sample at 900 °C for one hour, the Mössbauer spectrum is comprised of a quadrupole doublet in accordance with the antiferromagnetism of orthorhombic CaFe₂O₄. From the fitting curve a chemical shift of $\delta = 0.37$ mm s⁻¹ and a quadrupole splitting of $\Delta EQ = 0.50$ mm s⁻¹ were determined, which is in accordance with the literature for CaFe₂O₄ comprising Fe³⁺ in the high-spin state.^[197] The drastic change in magnetic behavior of the CaFe₂O₄ sample upon the calcination-induced phase transformation is confirmed by SQUID magnetometry (Figure 54b). At an external magnetic field of 20000 Oe, a magnetization of 25 emu g⁻¹ was determined for the as-synthesized sample, which is attributed to the magnetism of the Fe₃O₄ nanorods. Due to their small size, the nanorods exhibit superparamagnetic behavior at room temperature and therefore no hysteresis is observed in the respective magnetization curve. When the SQUID measurement is performed at 10 K, a hysteresis can be observed, indicating that T_B is located above 10 K (Figure 54c). An accurate determination of T_B *via* a ZFCM measurement was however not performed in this case. After calcination of the sample at 900 °C for one hour, the sample exhibits a room temperature magnetic moment of $\mu_{eff} = 5.13$ at 293 K, which is in accordance with the expected value for a d⁵ high-spin electronic system. The negligible response to an applied external magnetic field, confirms the antiferromagnetic nature of orthorhombic CaFe₂O₄ and the complete conversion of all magnetic by-phases that are formed during synthesis and thermal treatment.

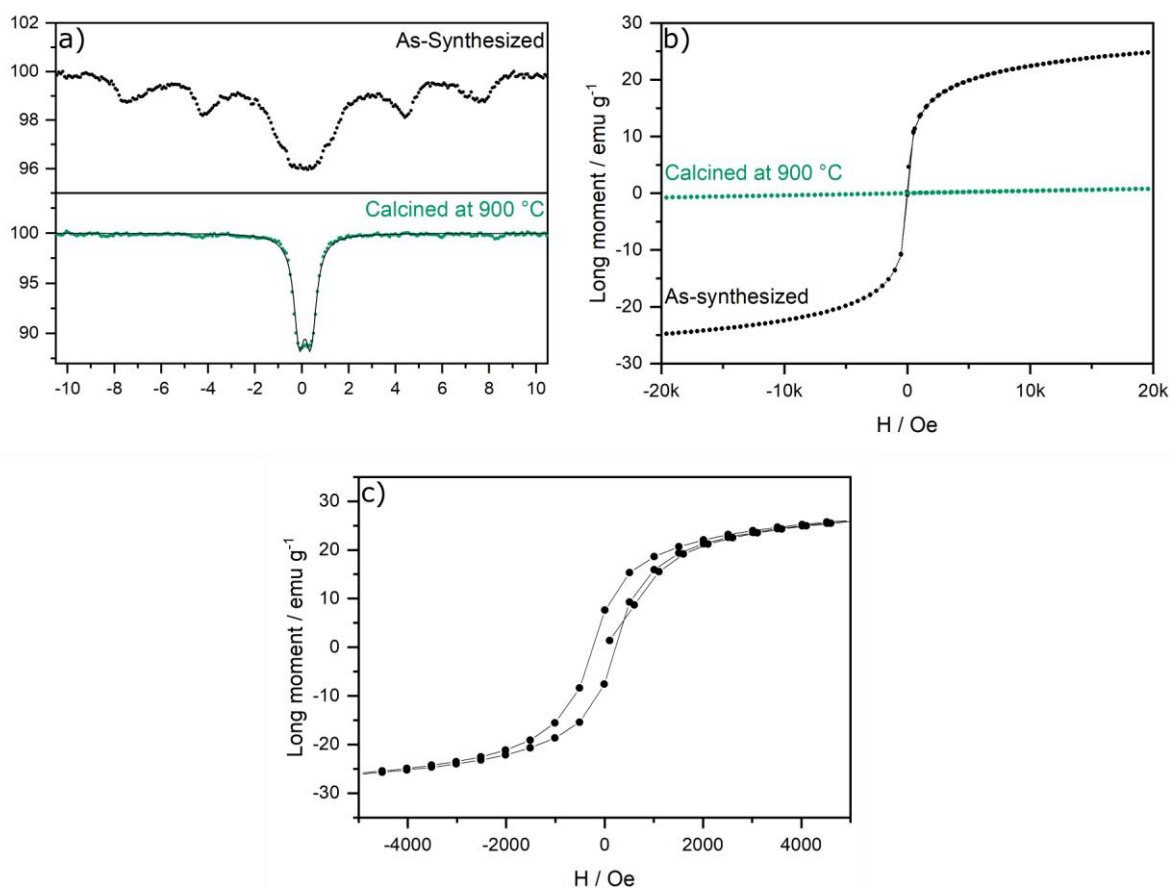


Figure 54: Mössbauer spectra of the $\text{CaCO}_3/\text{Fe}_3\text{O}_4$ precursor powder and macroporous CaFe_2O_4 after calcination at 900 °C for one hour. b) SQUID magnetization curves of the respective samples collected at 300 K. c) SQUID magnetization curve of the $\text{CaCO}_3/\text{Fe}_3\text{O}_4$ precursor powder collected at 10 K.

4.4.4 Optical properties

Equal to the spinel ferrites, CaFe_2O_4 comprises an Fe^{3+} cation with d^5 electron configuration in an oxygen coordination sphere as chromophore. Its diffuse reflectance spectrum (Figure 55a) can therefore be interpreted similar to that of MgFe_2O_4 , with the difference, that it should not comprise any transitions corresponding to Fe^{3+} in tetrahedral coordination. The visible light active excitations are attributed to $\text{O}(2p) \rightarrow \text{Fe}(3d)$ ligand-to-metal charge transfer excitations. The derivative curve (Figure 55b) illustrates that the absorption edge is indeed composed of two main transitions at 535 nm (2.3 eV) and 620 nm (2.0 eV), which is in reasonable accordance with the optical band gap of 1.9 eV that was reported in the literature and with the onset of absorption in the corresponding Kubelka-Munk spectrum (Figure 55c).^[87,105,109] A small absorption feature at 460 nm (2.7 eV) can still be made out, which would be in good accordance with the $\text{O}(2p) \rightarrow \text{Fe}(3d)$ charge transfer excitation corresponding to Fe^{3+} in tetrahedral coordination observed in the spectra of MgFe_2O_4 . Consequentially, this might indicate the presence of a trace impurity. The presence of the two major visible excitations is caused either by the distortion of the FeO_6 octahedra (According to the synchrotron diffraction based

crystal structure provided by Das *et al.*, the Fe-O bond lengths in the octahedra in orthorhombic CaFe_2O_4 vary in a range of 1.974–2.066 Å.^[110] or by crystal field exchange splitting effects.^[130]

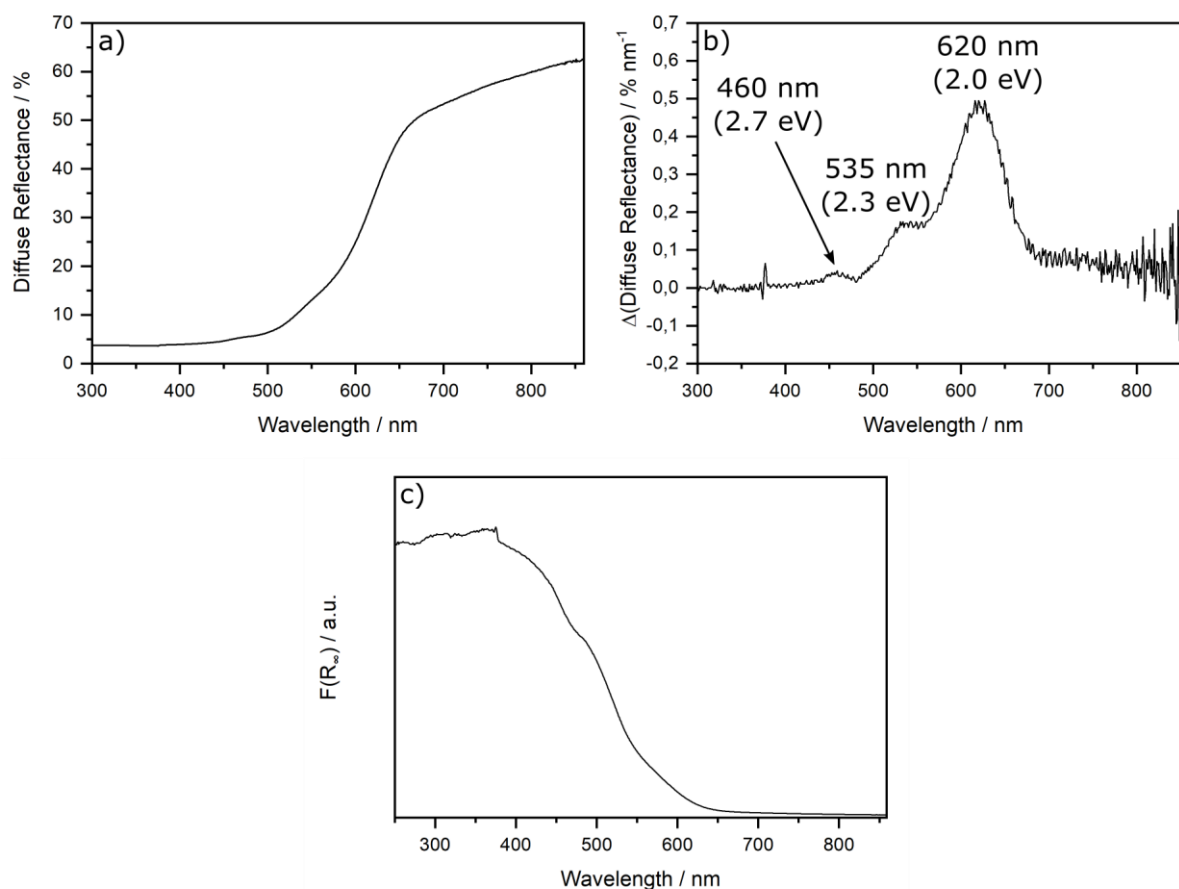


Figure 55: a) Diffuse reflectance spectrum of macroporous CaFe_2O_4 calcined at 900 °C for one hour. b) First derivative of the diffuse reflectance spectrum. c) Kubelka-Munk absorption spectrum calculated from the diffuse reflectance spectrum.

4.4.5 X-ray emission spectroscopy

VtC-XES was performed on macroporous CaFe_2O_4 to gain further insight into its electronic structure. Since no HERFD-XANES spectrum was available for CaFe_2O_4 , an approximation of the band gap from a combination of XANES and VtC-XES data could not be performed in this case. The VB energy is however determined relative to that of $\alpha\text{-Fe}_2\text{O}_3$, which was measured as a reference (Figure 56).

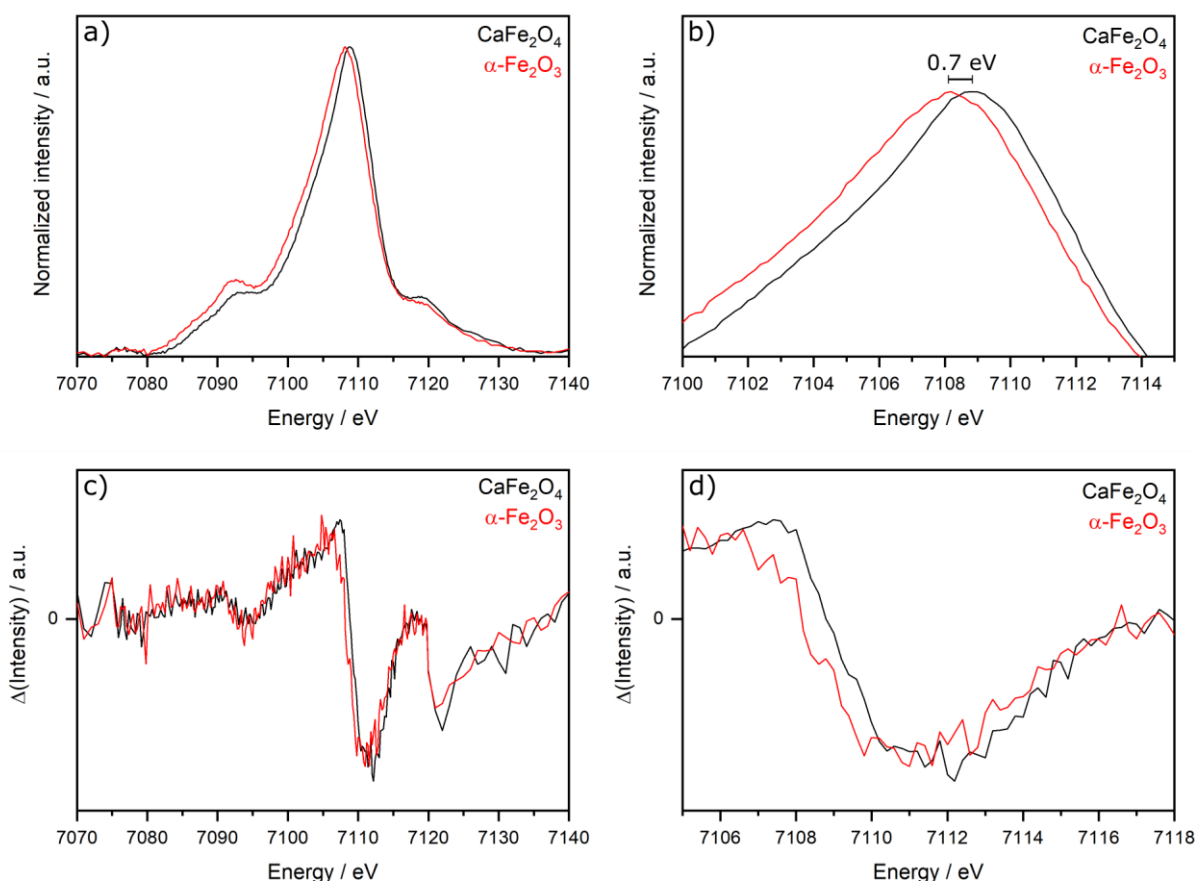


Figure 56: a) Normalized VtC-XES spectra of macroporous CaFe₂O₄ and α -Fe₂O₃. b) Enhanced depiction of VtC-XES spectrum at the K $\beta_{2,5}$ signal maximum. c) First derivative of the VtC-XES spectrum; d) Enhanced depiction of the first derivative in the region of the high-energy inflection point corresponding to the valence band edge.

A precise determination of the VBM proved challenging due to the large noise of the derivative plot (Figure 56, c-d). Nevertheless, it is clearly visible that the minimum of the derivative curve is shifted towards a higher emission energy in the case of CaFe₂O₄, suggesting a more cathodic VB potential compared to α -Fe₂O₃. From the signal maxima, the shift of the K $\beta_{2,5}$ signal can be approximated to be 0.7 eV. Assuming a CBM of +0.34 V vs. RHE^[198] and a band gap of 2.03 eV (determined by diffuse reflectance spectroscopy, see Figure A8 in the appendix), the VBM of α -Fe₂O₃ is located at +2.37 eV. Consequently, the VBM and CBM of CaFe₂O₄ are located at +1.67 V vs. RHE and -0.33 V vs. RHE, respectively, when an optical band gap of 2.0 eV (see Figure 55b) is assumed for the calculation of the CBM. Considering those results, hydrogen reformation or even overall water splitting should be possible using CaFe₂O₄. Despite the determined band gaps of α -Fe₂O₃ and CaFe₂O₄ being in accordance with the literature, it must however be kept in mind, that both materials comprise Fe³⁺ with d⁵ high-spin electronic configuration and therefore the optical band gaps likely are not equivalent to the electronic band gaps. Future research into that matter including high quality HERFD-XANES data of CaFe₂O₄ is hence presumed necessary to validate the interpretation of the VtC-XES data.

4.4.6 Photoelectrochemistry and photocatalysis

In contrast to the nanoparticle morphology of the MgFe₂O₄ samples, macroporous CaFe₂O₄ exhibits crystalline pore walls with diameters of several hundred nanometers. The semiconductor-electrolyte interface is therefore more homogeneous and can comprise a well-defined space charge layer. Hence, it was possible to conduct (photo-)electrochemical measurements on a macroporous CaFe₂O₄ photoelectrode prepared by spray-coating. Mott-Schottky analysis confirms the expected *p*-type semiconducting behavior by the negative slope of the inverse square capacitance plot (Figure 57). The flat band potential was determined to be 1.43 V vs. RHE. In the case of a *p*-type semiconductor, the position of the flat band is located slightly above the valence band maximum. Assuming an optical band gap of 2.0 eV, this implies a CBM located at -0.57 V vs. RHE, which is slightly more cathodic than the value determined by VtC-XES and in very good accordance with the values reported in the literature.^[106,108] Since this method for the determination of band potentials also relies on a band gap determined by optical spectroscopy, the results however comprise a similar uncertainty than those obtained by VtC-XES.

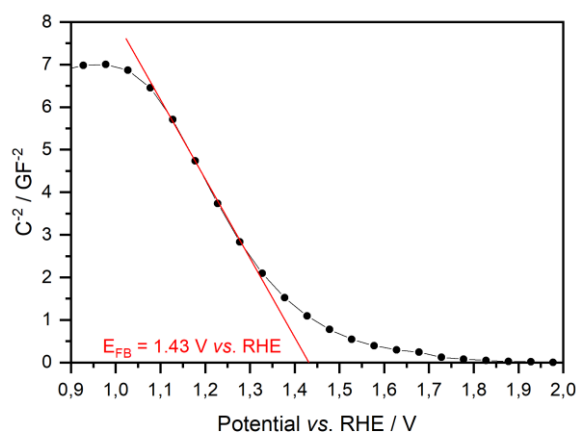


Figure 57: Mott-Schottky plot of macroporous CaFe₂O₄.

The strong localization of orbitals involved in the absorption of visible light and the small polaron mediated self-trapping^[191], which were identified as reasons for the unfavorable charge carrier dynamics in MgFe₂O₄, likely apply to CaFe₂O₄ as well and explain lacking photocatalytic activity. This is reflected in the inability of macroporous CaFe₂O₄ to split pure water in the conducted test reactions, even after the deposition of a RhCrO_x water-splitting co-catalyst.^[63] No activity was observed in such experiments, regardless if visible light or UV-light were used to irradiate the CaFe₂O₄ suspension. The addition of methanol as a hole-scavenging sacrificial agent and the deposition of 0.5 w% platinum as co-catalyst, did not facilitate the generation of hydrogen. Likewise, no activity could be observed when macroporous CaFe₂O₄ was employed for the degradation of nitrobenzene or rhodamine B under visible

light. The material can therefore be considered not suitable for bias-free photocatalytic applications unless the polaron mediated trapping of charge carriers can be overcome in the future.

When an external voltage was applied to macroporous CaFe₂O₄ photoelectrodes, chopped light voltammetry (Figure 58a) revealed a distinct photocurrent response under illumination with a white light LED ($\lambda = 400\text{--}800\text{ nm}$) in the presence of H₂O₂ as a sacrificial agent. Notably, the direction of the photocurrent changes at a potential of +0.7 V vs. RHE. This behavior is attributed to the presence of H₂O₂, which can both be reduced and oxidized by the charge carriers generated in the photoelectrode.^[199] The IPCE spectrum (Figure 58b) revealed the generation of a photocurrent under illumination with visible light of wavelengths below 600 nm, which is in very good accordance with the absorption spectrum of CaFe₂O₄ (See Figure 55c). This confirms that the optically active LMCT excitations can in principle be exploited for the generation of a photocurrent when an external electric field and a suitable sacrificial agent are present. The currently achievable current densities nevertheless are too low for the material to be considered an alternative to photovoltaics driven electrolyzers.

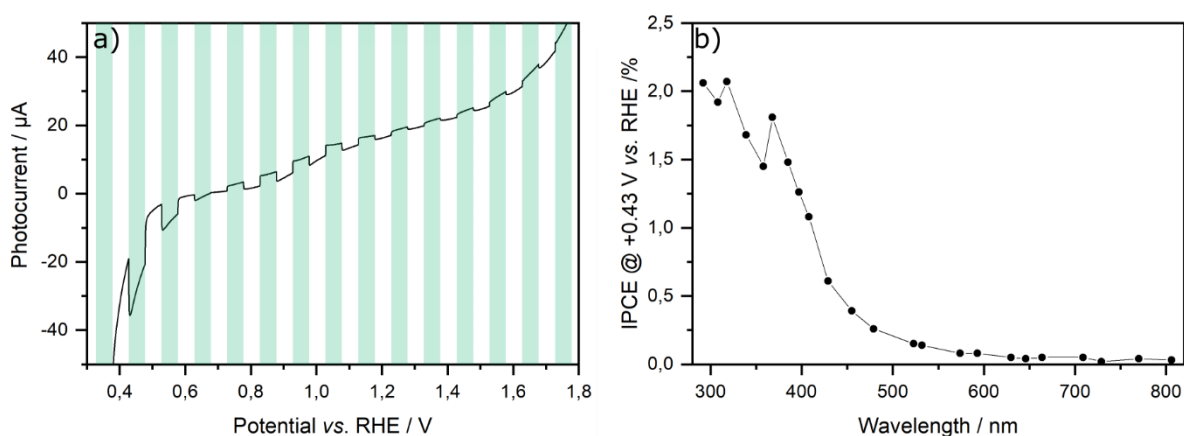


Figure 58: a) Chopped-light voltammetry of a macroporous CaFe₂O₄ photoelectrode. The intervals where the electrode was illuminated are highlighted in green; b) IPCE spectrum at an applied external bias of +0.43 V.

4.5 Microwave-assisted synthesis of macroporous MgFe₂O₄

Based on the observations made in the synthesis of macroporous CaFe₂O₄, the synthesis procedure was adapted for MgFe₂O₄. This way it should be investigated whether the formation of macropores also occurs in the case of other ferrites. In the respective synthesis, Mg(OAc)₂·4H₂O and Fe(NO₃)₃·9H₂O were subjected to microwave heating in 1,4-butanediol. In contrast to the phase mixture obtained in the synthesis for macroporous CaFe₂O₄, the microwave reaction at 300 °C for 30 min yielded a spinel

structure as the sole phase identifiable by X-ray diffraction (Figure 59). The as-synthesized material is nanocrystalline and exhibits an average crystallite size of 8 nm. After calcination at 900 °C for one hour (heating rate: 10 K min^{-1}) the crystallite size is increased to 47 nm, which is comparable to the crystallite size of CaFe_2O_4 synthesized in a similar fashion. On first glance, no indications of a by-phase can be found in the X-ray diffraction patterns, which are in good agreement with the literature (Figure 59a, ICDD 01-073-2410). On a closer look however, the (422), (511) and (440) reflections show a systematic asymmetry that might indicate the presence of another spinel phase (Figure 59b). Notably a peak shape asymmetry was not observed for the reflections at lower Bragg angles. The asymmetry is surprising, since EDX spectroscopy confirms a close-to ideal Mg:Fe cation ratio of 0.47 and the observed shoulders could not be attributed to the presence of either Fe_3O_4 or $\gamma\text{-Fe}_2\text{O}_3$, which are common by-phases in spinel ferrite syntheses. Furthermore, if either of those phases were present, the presence of $\alpha\text{-Fe}_2\text{O}_3$ would be expected after calcination at 900 °C. The origin of this observed peak shape asymmetry therefore must be further investigated in future experiments.

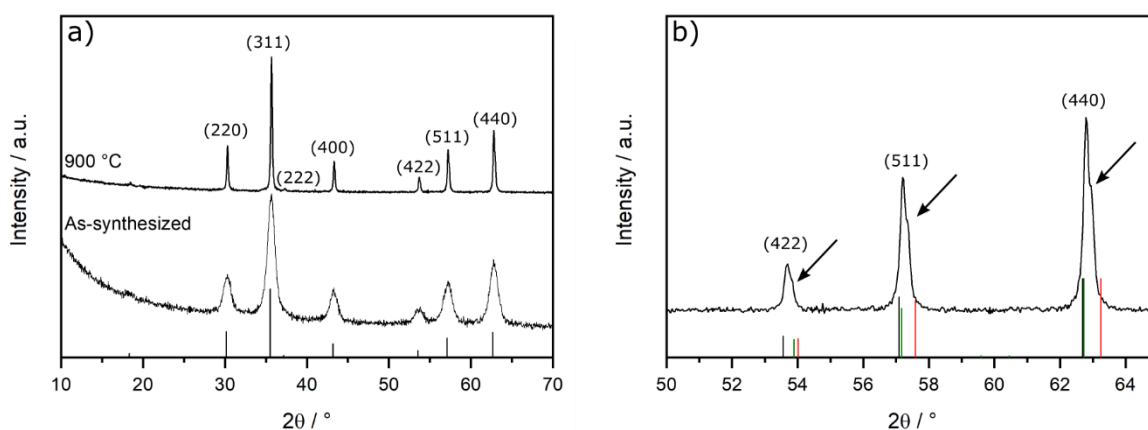


Figure 59: a) Diffraction patterns of MgFe_2O_4 synthesized via an adaption of the synthesis protocol for macroporous CaFe_2O_4 , before and after calcination at 900 °C for one hour. b) Enhanced depiction revealing a peak shape asymmetry of some reflections (indicated by arrows). References are given for MgFe_2O_4 (black, ICDD 01-073-2410), Fe_3O_4 (red, ICDD 01-075-0449) and $\gamma\text{-Fe}_2\text{O}_3$ (green, ICDD 00-004-0755)

SEM images (Figure 60) reveal that the obtained MgFe_2O_4 sample does not exhibit a macropore structure comparable to that of CaFe_2O_4 . Instead, a sintered structure of aggregated nanoparticles without considerable porosity is obtained. This confirms that the presence of CaCO_3 in the as-synthesized powder and the continuously ongoing phase transitions during the calcination process are responsible for the retention of the pore system in the case of CaFe_2O_4 (since both conditions do not apply in this synthesis for MgFe_2O_4).

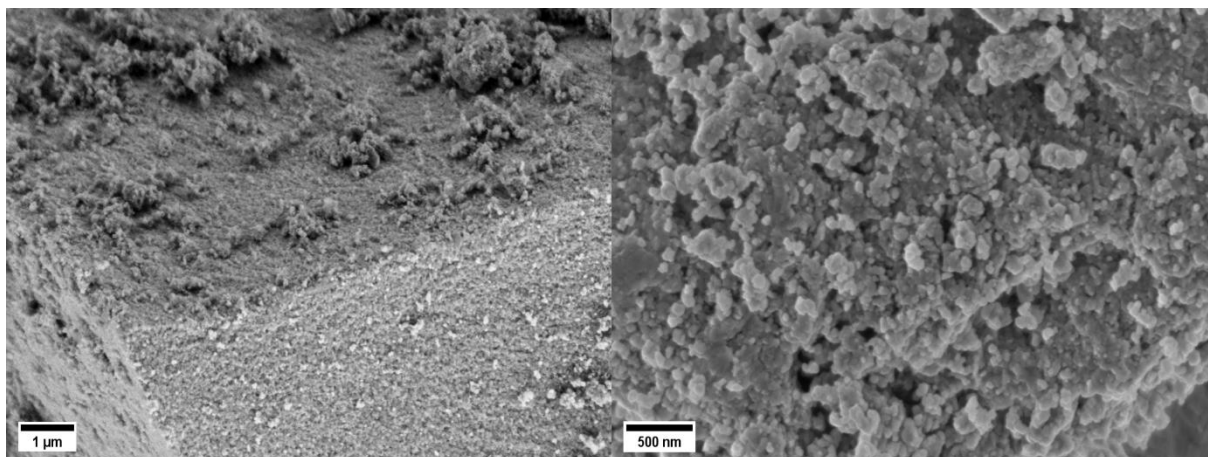


Figure 60: SEM images of MgFe_2O_4 synthesized via an adapted synthesis for macroporous CaFe_2O_4 . In contrast to CaFe_2O_4 the obtained sample exhibits no distinct macropore structure.

N_2 -physisorption and MIP must be performed in the future to confirm the optical impression and to investigate the changes of the morphology during calcination in greater detail. Despite the inability to form a macroporous structure after calcination, this synthesis strategy might be a viable alternative to the acetylacetonate-based nanoparticle synthesis, as it yields nanocrystalline MgFe_2O_4 without post-synthetic calcination and also without the need for the application of the magnesium salt in excess, thus offering a much better atom economy.

4.6 Combination of MgFe_2O_4 with functional mesoporous host networks

In search of a strategy to produce a multi-functional composite able to combine photocatalysis with other types of catalysis in a single material, an immobilization of MgFe_2O_4 nanoparticles inside the pores of a functionalized mesoporous host structure was attempted. KIT-6 type mesopore structures consisting of PMO and SiO_2 , were chosen as model frameworks for combination with the ferrite photocatalyst and different strategies for the introduction of MgFe_2O_4 into the pore network were investigated. Due to the lacking photocatalytic performance of the MgFe_2O_4 nanoparticles, which became apparent during the course of this work, the obtained composites did not show any photocatalytic activity. Nevertheless, the investigated strategies can be considered model pathways for the combination of the respective porous host networks with other, more reactive photocatalysts.

4.6.1 Combination of MgFe_2O_4 nanoparticles with KIT-6 type mesoporous SiO_2

The combination of MgFe_2O_4 nanoparticles with mesoporous KIT-6 SiO_2 was realized by infiltration of the pre-synthesized SiO_2 framework with the precursor solution used in the microwave assisted synthesis for MgFe_2O_4 nanoparticles. After the infiltration, the suspension was subjected to microwave treatment at 250 °C, similar to the initial synthesis for MgFe_2O_4 .

SAPXRD and PXRD patterns of the obtained brown powder confirm the formation of MgFe_2O_4 in the presence of a periodic pore system (Figure 61). Notably, a calcination step is not necessary in this case to induce crystallinity of MgFe_2O_4 , since the spinel phase is already crystalline in the as-synthesized product, with an average crystallite size of 6 nm. This might be explained by the presence of free hydroxyl groups on the SiO_2 surface, which act as crystallization centers for the spinel. After calcination at 600 °C for five hours the crystallite size is increased only slightly to 7 nm. The crystallite growth is therefore hindered compared to pure MgFe_2O_4 nanoparticles synthesized at 250 °C, where a crystallite size of 11.5 nm after calcination at 600 °C for only 1 h was observed. This implies, that MgFe_2O_4 is indeed formed inside the pore network, which restricts further growth of the crystallites. The retention of the KIT-6 morphology upon calcination is confirmed by SAPXRD. The shift of the reflections in the small angle regime indicates a shrinkage of the pore system as the lattice spacing of the (211) reflection is decreased from 9.5 nm to 9.0 nm. Since the measurement was performed with a commercial PXRD instrument, which is not specifically designed for measurements in the small angle regime, it can however not be excluded that the observed shift is a result of a height displacement going in line with small variations during sample preparation.

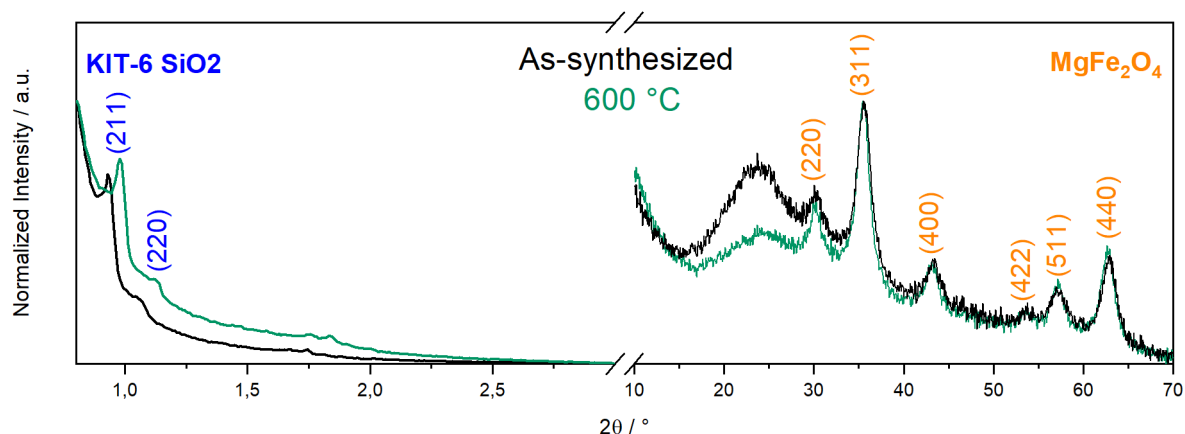


Figure 61: SAPXRD and PXRD patterns of MgFe_2O_4 @KIT-6 SiO_2 , after synthesis at 250 °C for one hour and after subsequent calcination at 600 °C for 5 hours. The observed reflections can be indexed according to the periodicity of the KIT-6 gyroidal mesopore structure (Ia3d, blue) and the spinel structure of MgFe_2O_4 (Fd3m, orange). The broad feature between 20 and 30 ° 2θ is attributed to the presence of amorphous SiO_2 .

Optical microscopy (Figure 62a) shows spherical structures, whose brown color suggests a homogeneous distribution of MgFe_2O_4 throughout the silica framework. TEM images (Figure 62b) reveal the presence of well-distributed MgFe_2O_4 nanoparticles in close phase contact with the mesoporous KIT-6 SiO_2 support.

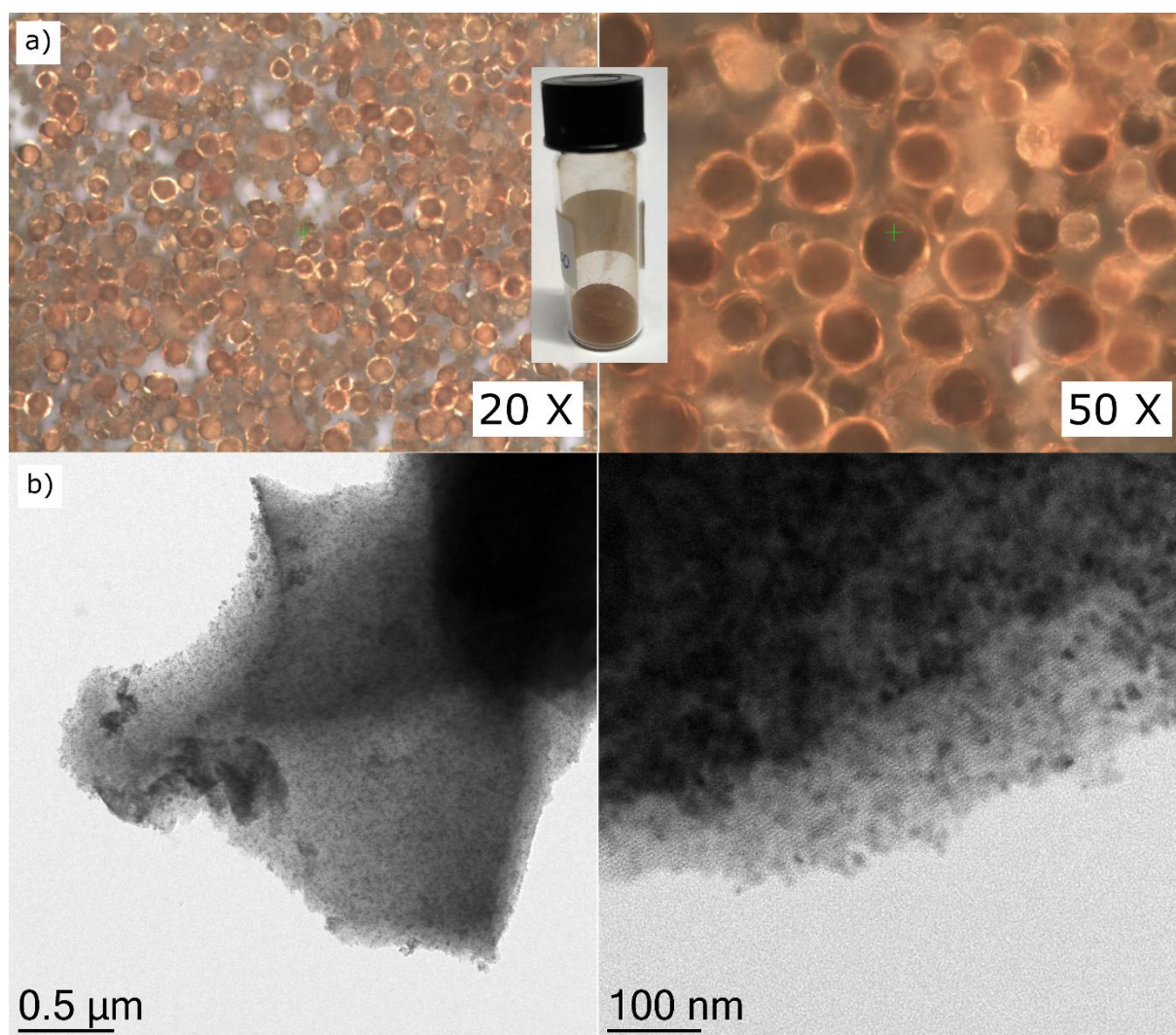


Figure 62: a) Camera and optical microscope images of $\text{MgFe}_2\text{O}_4@KIT-6 \text{SiO}_2$ after calcination at 600°C for 5 hours. b) TEM images of MgFe_2O_4 nanoparticles immobilized on mesoporous $KIT-6 \text{SiO}_2$.

N_2 physisorption (Figure 63) reveals an increase of the BET surface area of $\text{MgFe}_2\text{O}_4@KIT-6 \text{SiO}_2$ after calcination at 600°C for five hours, which is explainable by the presence of organic residues in the pores of the as-synthesized sample, which are removed during calcination. Compared to the $KIT-6 \text{SiO}_2$ starting material, the isotherms suggest a smaller BET surface area of the composite, which is attributed both to the partial filling of the pores by MgFe_2O_4 and to the higher density of the composite compared to SiO_2 (Bulk MgFe_2O_4 is more dense than bulk SiO_2). The similar hysteresis behavior observed for all isotherms indicates that the mesopore system remains accessible for gas molecules, after the introduction of the nanoparticles and the subsequent calcination.

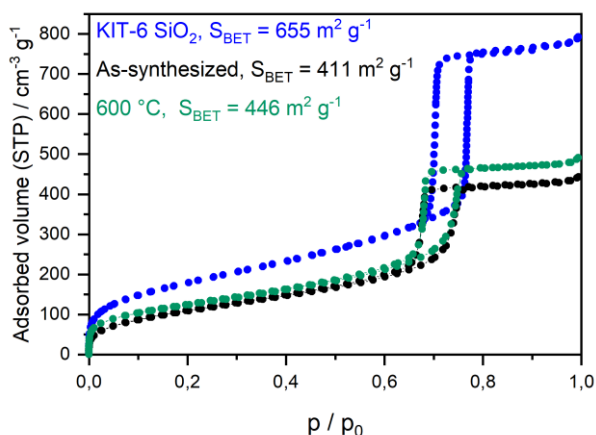


Figure 63: N₂-physorption isotherms of MgFe₂O₄@KIT-6 SiO₂ after microwave synthesis (black) and after calcination at 600 °C for one hour (black). The isotherm of the KIT-6 SiO₂ starting material is shown in blue for comparison

A close-to-ideal Mg:Fe ratio of 0.54 was determined from 3 individual sites on the sample, confirming the phase purity of the MgFe₂O₄ nanoparticles. In accordance with that, no by-phases are observed after calcination at 600 °C. Higher calcination temperatures were not investigated. A formation of iron silicates above a certain temperature is likely. The atomic ratio of Mg:Si was determined to be 0.23. Considering the molecular masses of 200 g mol⁻¹ for MgFe₂O₄ and 60 g mol⁻¹ for SiO₂, this indicates that MgFe₂O₄ accounts for roughly 43% of the mass of the composite material.

Timm *et al.* have demonstrated, that the surface of mesoporous SiO₂ structures can be effectively modified with thiol groups in the gas phase, using (3-Mercaptopropyl)trimethoxysilane in a CVD related grafting procedure.^[150] Through subsequent oxidation and protonation a solid acid can be produced from the thiol functionalized SiO₂. An adaptation of this synthesis was attempted for the production of MgFe₂O₄@KIT-6 SiO₂ with surface-attached sulfonic acid groups. Both as-synthesized MgFe₂O₄@KIT-6 SiO₂ and a sample that was calcined at 600 °C for 5 h were investigated as starting material for surface modification. Water vapor physisorption isotherms (Figure 64,a–b) show a trend similar to that observed in the functionalization of pure KIT-6 SiO₂.^[150] After surface modification with thiol groups, the material becomes significantly hydrophobic. After oxidation of the thiol moieties to sulfonic acid groups, hydrophilicity is increased again. A shift of the hysteresis loop can be observed, when as-synthesized MgFe₂O₄@KIT-6 SiO₂ was used as starting material (Figure 64a). In the case where calcined MgFe₂O₄@KIT-6 SiO₂ was chosen as starting material, this shift is much less pronounced. The difference in the hysteresis behavior and between the adsorbed volumina of water must therefore originate from the presence of the organic contamination that was indicated by N₂-physorption. Acetylacetonate residues in the pores would interfere with water absorption, due to hydrogen bonding with the carbonyl groups, explaining the higher uptake of water.

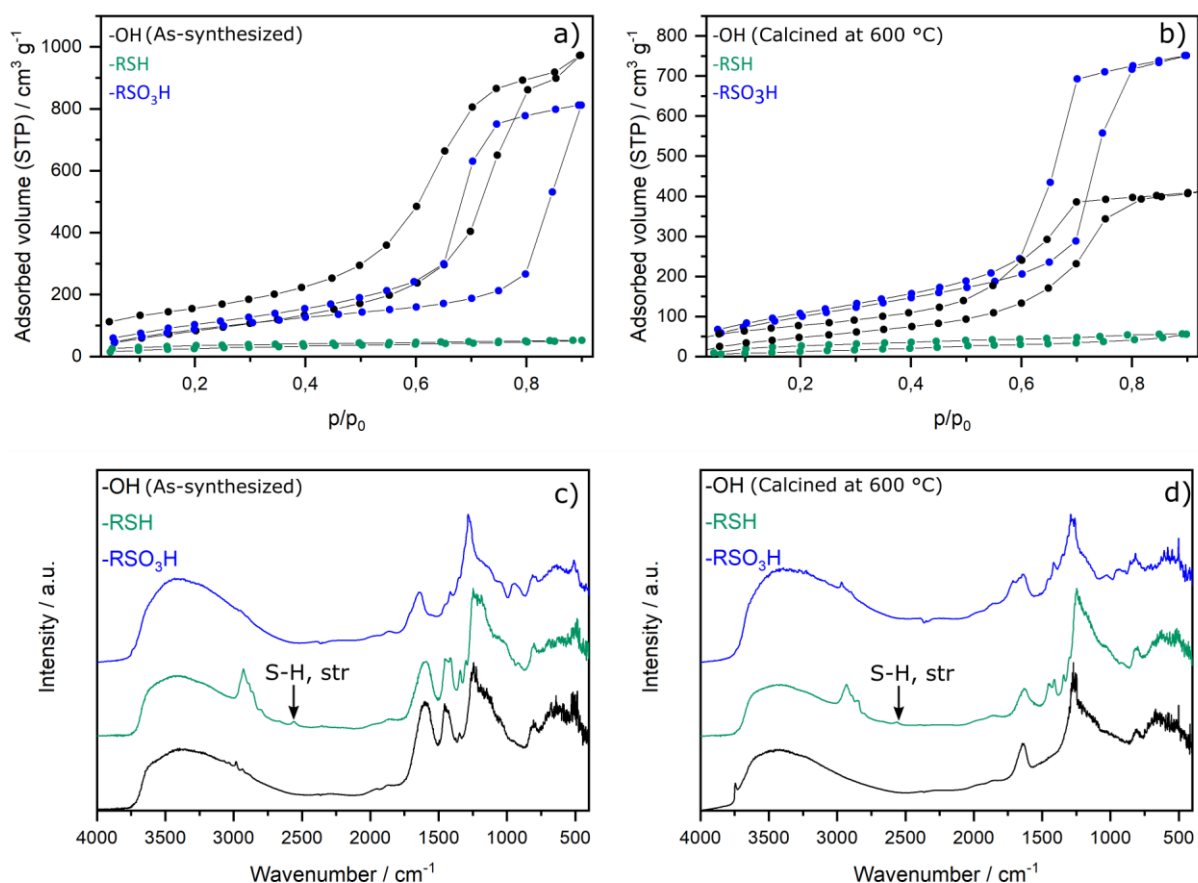


Figure 64: Water vapor physisorption isotherms (293.15 K) of as-synthesized (a) and calcined (b) MgFe_2O_4 @KIT-6 SiO_2 (black curves). The green and blue data points correspond to the isotherms of the respective sample after surface functionalization with thiol groups (-RSH) and after oxidation of the thiol groups to sulfonic acid groups (- RSO_3H), respectively. c) and d) show the DRIFT spectra of the respective samples, before (black) and after functionalization with thiol (green) and sulfonic acid (blue) groups.

Weak C-H stretching vibrations at 2935 cm^{-1} and 2950 cm^{-1} and C-H bending vibrations at 1450 cm^{-1} in DRIFT spectroscopy confirm the presence of organic residues in the as-synthesized composite (Figure 64c, black curve). For the sample that was calcined prior the CVD grafting procedure (Figure 64d, black curve) those signals are absent. The broad feature from $3000\text{--}3750 \text{ cm}^{-1}$ and the band at 1630 cm^{-1} originate from adsorbed water, and the signal at 3745 cm^{-1} is attributed to the O-H stretching vibration of isolated silanol groups on the surface of the silica framework.^[200] The broad feature at 1250 cm^{-1} and the absorption band at 810 cm^{-1} originate from the presence of SiO_2 .^[201] After functionalization with MPTMS, the signal corresponding to the free silanol groups disappears and additional bands emerge at 2840 cm^{-1} , 2890 cm^{-1} and 2930 cm^{-1} , which are attributed to C-H stretching vibrations of the attached propyl-thiol moiety, whose presence is additionally indicated by the weak S-H stretching vibration at 2560 cm^{-1} . DRIFT spectroscopy therefore confirms the successful grafting of thiol groups onto the surface of the composite. Both SiO_2 and MgFe_2O_4 can exhibit free hydroxyl groups on the surface. It is therefore likely that both the silica surface and the MgFe_2O_4 surface are modified

with thiol groups during treatment with MPTMS. Indeed, the successful functionalization of pure MgFe_2O_4 nanoparticles using this CVD approach was already demonstrated in a work by Felix Bretschneider.^[202] Oxidation of the surface-bound thiol to sulfonic acid groups is performed by stirring of the composite material in an aqueous solution of 30 w% H_2O_2 for one day and subsequent protonation by addition of HNO_3 . The increased water uptake of the material after oxidation indicates the conversion of the thiol to the more hydrophilic $\text{SO}_3\text{-H}$ groups. This is accompanied by a significantly reduced intensity of the C-H stretching modes in the DRIFT spectra, indicating a removal of residual free MPTMS in the pores of the KIT-6 structure. Successful oxidation of the surface-bound thiol groups is indicated by the shift of the C-H stretching modes towards higher energy and the disappearance of the S-H stretching mode, while signal at 3745 cm^{-1} corresponding to isolated surface silanol groups does not re-emerge after treatment with H_2O_2 .^[150] Titration and proton conduction experiments are suggested to be conducted in the future, to confirm the successful attachment of the acid and to determine the degree of functionalization. For the successful conversion of the thiol functionalized composite to the solid acid, the concentration of HNO_3 during protonation needed to be kept low, since the MgFe_2O_4 nanoparticles inside the framework tended to dissolve at low pH levels, while the SiO_2 framework remained intact. The decomposition was confirmed by the decolorization of the material and the absence of a spinel structure in the PXRD pattern after acid treatment (Figure 65). Since the product of the functionalization is itself an acid, long-term stability tests have to be performed to ensure that the composite does not decompose in when applied aqueous media.

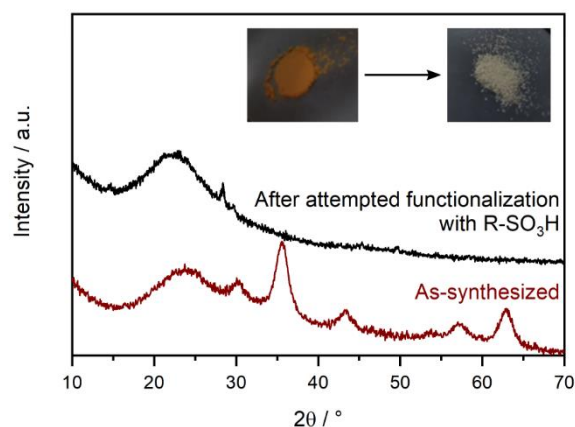


Figure 65: X-ray diffraction pattern illustrating the decomposition MgFe_2O_4 upon treatment of $\text{MgFe}_2\text{O}_4@$ KIT-6 SiO_2 at low pH levels.

4.6.2 Combination of MgFe₂O₄ nanoparticles with KIT-6 type mesoporous PMO

A synthesis for MgFe₂O₄ nanoparticles immobilized on a KIT-6 type, phenylene bridged, periodic mesoporous organosilica network was developed. In contrast to the synthesis of MgFe₂O₄@KIT-6 SiO₂, a different approach for the combination of the ferrite with the framework was chosen. The synthesis is based on the condensation of bisilylated 1,4-bis(triethoxysilyl)benzene in the presence of pre-synthesized MgFe₂O₄ nanoparticles. The resulting composite retains the high specific surface area of the PMO, while exhibiting the visible absorption characteristics of MgFe₂O₄. Furthermore, the MgFe₂O₄ nanoparticles exhibit an increased stability towards corrosion in acidic media. Since synthesis procedure and material characteristics of the MgFe₂O₄ nanoparticles are already discussed in chapter 4.2, and the synthesis of the PMO in the presence of those particles was not performed by the author of this thesis, a detailed discussion of the results will not be done at this point. The reader is instead referred to the respective publication for a detailed characterization and interpretation of the data.^[90]

5 Conclusion and outlook

The main goal of this work was the assessment of the suitability of MgFe_2O_4 and CaFe_2O_4 for photocatalytic applications. A focus was laid on the applicability towards hydrogen reformation and overall water splitting, since these techniques present promising pathways for an efficient conversion of solar energy into clean fuels in the future. Band gaps and band positions reported in the literature for MgFe_2O_4 showed large discrepancies and publications reporting hydrogen evolution using ferrite photocatalysts were scarce. An in-depth characterization of the optoelectronic properties of MgFe_2O_4 and CaFe_2O_4 was performed using self-produced material, to gain further insight into the photocatalytic abilities of ferrites. MgFe_2O_4 was synthesized in the form of nanoparticles and CaFe_2O_4 in the form of macroporous sponge structures. The work on MgFe_2O_4 was based on a nanoparticle synthesis presented by Kirchberg *et al.* in 2017. A detailed EDX-based characterization led to the realization that this synthesis produces MgFe_2O_4 nanoparticles with non-ideal cation composition. A deficiency in magnesium was detected and deemed responsible for the formation of a hematite impurity upon calcination of the nanoparticles in an oxygen-containing atmosphere. The synthesis route was therefore optimized by an adjustment of the precursor stoichiometry, to produce phase-pure MgFe_2O_4 nanoparticles with an ideal ratio between magnesium and iron cations.

Additional to the synthesis for pure MgFe_2O_4 nanoparticles, strategies were developed towards the production of composites that are composed of MgFe_2O_4 nanoparticles enclosed in a surface functionalized mesoporous(organo-)silica framework. The obtained materials can be considered first steps towards the synthesis of multi-functional catalysts combining photocatalysis with other types of catalysis (e.g. acid/base catalysis) using a single material.

A novel microwave-assisted synthesis for macroporous CaFe_2O_4 sponge structures was developed since it was not possible to adapt the MgFe_2O_4 synthesis for the production of CaFe_2O_4 . By employing a route that relies on the calcination of a microwave reaction derived intermediate nanopowder consisting of Fe_3O_4 and CaCO_3 , it was possible to synthesize phase-pure and crystalline CaFe_2O_4 with a macropore structure in only one hour at a temperature of 900 °C.

Additional to the syntheses of MgFe_2O_4 and CaFe_2O_4 , first attempts towards the microwave assisted synthesis of NiFe_2O_4 and MnFe_2O_4 were made.

A large spectrum of characterization techniques reaching from different types of diffraction experiments over multiple spectroscopic techniques to magnetic measurements were employed to ensure the phase purity of the synthesized materials. This was necessary since the presence of

by-phases is known to significantly alter the photocatalytic properties of a material. The determined crystal structures and optical absorption spectra were in good agreement with published literature. Band positions determined by Mott-Schottky analysis suggest, that MgFe_2O_4 is not able to reduce protons, which is in conflict with the values given in earlier works.^[19,97] In the case of CaFe_2O_4 , the electrochemical experiments suggest that the reduction of hydrogen is possible. Nevertheless, hydrogen evolution could not be achieved using either of the synthesized materials, irrespective of the emission spectrum of the employed light source.

A detailed interpretation of the optical spectra and an in-depth characterization of the electronic structure using XANES and VtC-XES data led to a better understanding of the absorption characteristics of ferrites. The unfavorable diffusion characteristics of charge carriers excited by the optically active $\text{O}(2p) \rightarrow \text{Fe}(3d)$ LMCT transitions (caused by a weak overlap of the involved orbitals and ultra-fast trapping mechanisms) have been identified as the main reason for the lacking photocatalytic activity. Because of this intrinsic shortcoming, the suitability of the synthesized materials in photocatalysis is presumed low. Regarding the application for proton reduction, the conducted experiments suggest that the suitability of ferrites has been overestimated in the past due to an incorrect determination of band positions as a consequence of the complex electronic structure that calls for a strict differentiation between optical band gap and electronic band gap. A semiconductor model assuming fully delocalized electronic bands is not suitable for the interpretation of the absorption spectra of ferrites and a determination of band potentials by a combination of Mott-Schottky analysis and Tauc plots can easily result in the misinterpretation of data, giving an explanation for the great dissent found in the literature. Regarding an application as a photoelectrode, the materials proved more promising, since the application of an external voltage can compensate for the unfavorable charge carrier mobility to some degree. A photocurrent generation could be observed by illumination of CaFe_2O_4 with visible light, in the presence of a suitable sacrificial agent. Strategies to improve the performance must however be developed in the future, since the achievable photocurrent densities are currently too low to compete with alternative techniques.

Due to their tunable magnetism, the MgFe_2O_4 nanoparticles are considered a promising candidate for applications in biomedicine. The cation inversion related high saturation magnetization of the as-synthesized particles makes them especially interesting for applications where very small ($d < 5$ nm) nanoparticles with high magnetization are needed. The nanoparticles should therefore be investigated further regarding such applications and their performance should be compared to the conventionally used Fe_3O_4 .

To complement the experiments conducted for this work, some further material characterization is suggested to be performed in the future.

Using mass spectrometry coupled with TGA it should be investigated whether the retention of the nanoparticle morphology upon calcination of microwave reaction derived MgFe_2O_4 nanoparticles is related to the presence of a carbonate species. Furthermore it should be investigated whether the synthesis route based on the decomposition of $\text{Mg}(\text{OAc})_2 \cdot 4\text{H}_2\text{O}$ and $\text{Fe}(\text{NO}_3)_3$ provides a viable alternative to the acetylacetonate based route that was mainly used for the production of MgFe_2O_4 nanoparticles, during this work. Since the former synthesis does not require the application of the magnesium salt in excess, it would offer a much better atom economy and is therefore considered a promising route, provided that the formation of by-phases can be avoided. Additionally, it should be investigated whether the synthesis procedure can be employed to produce ferrite nanoparticles with other *A* cations, since many of the required acetate precursors are already commercially available.

The acetylacetonate-based synthesis for NiFe_2O_4 nanoparticles needs to be optimized to ensure that no elemental nickel is formed during synthesis. The NiFe_2O_4 nanoparticles showed a strong magnetic response to the presence of a permanent magnet and therefore an in-depth characterization using Mössbauer spectroscopy and SQUID magnetometry should be performed. Concerning the MnFe_2O_4 nanoparticles it needs to be confirmed whether the peak-shape asymmetry that was observed in the PXRD patterns is related to the presence of an iron oxide impurity, before any further going characterization is performed.

As mentioned before, the suitability of ferrites for photocatalytic applications is presumed low. Nevertheless, if further photocatalytic test reactions are to be performed in the future, the deposition of co-catalysts on such small nanoparticles must be optimized, since photodeposition and wet-impregnation techniques likely result in a non-ideal coverage, when only small amounts of the co-catalyst are employed.

HERFD-XANES spectroscopy needs to be performed on macroporous CaFe_2O_4 , to probe the electronic structure of the conduction band states and to get a full picture of the band structure by combining those measurements with the VtC-XES spectra that were already measured in the course of this work. Going in line with this, optical absorption spectroscopy should be extended into the NIR regime to investigate the role of crystal field transitions in the absorption of visible light. Furthermore such advanced X-ray based techniques should also be employed on other ferrites and transition metal oxides comprising elements with a partially filled *d*-shell, to confirm whether the conclusions drawn from the data on MgFe_2O_4 and CaFe_2O_4 , apply to those materials as well.

The achievable loading of sulfonic acid groups on the $\text{MgFe}_2\text{O}_4@\text{SiO}_2$ composite material should be determined using titration with a base. Furthermore, the acid-stability of those composites needs to be further confirmed to assure that the material does not decompose when applied for acid-base catalysis. To circumvent emerging stability issues, a coating of the composite with an ultra-thin SiO_2 or Al_2O_3 protection layer, prior to the functionalization with acid groups, can be considered. Such a protection layer could be realized via atomic layer deposition.

6 References

- [1] J. Cook, N. Oreskes, P. T. Doran, W. R. L. Anderegg, B. Verheggen, E. W. Maibach, J. S. Carlton, S. Lewandowsky, A. G. Skuce, S. A. Green, D. Nuccitelli, P. Jacobs, M. Richardson, B. Winkler, R. Painting, K. Rice, *Environ. Res. Lett.* **2016**, *11*, 048002.
- [2] W. M. Jolly, M. A. Cochrane, P. H. Freeborn, Z. A. Holden, T. J. Brown, G. J. Williamson, D. M. J. S. Bowman, *Nat. Commun.* **2015**, *6*, 1.
- [3] E. Wollenberg, S. J. Vermeulen, E. Girvetz, A. M. Loboguerrero, J. Ramirez-Villegas, *Glob. Food Sec.* **2016**, *11*, 34.
- [4] International Energy Agency, *World Energy Outlook 2019*; Paris, **2019**.
- [5] T. Kim, W. Song, D. Y. Son, L. K. Ono, Y. Qi, *J. Mater. Chem. A* **2019**, *7*, 2942.
- [6] T. A. Faunce, J. Prest, D. Su, S. J. Hearne, F. Iacopi, *MRS Energy Sustain.* **2018**, *5*, 1.
- [7] A. Fujishima, K. Honda, *Nature* **1972**, *238*, 37.
- [8] D. Spasiano, R. Marotta, S. Malato, P. Fernandez-Ibañez, I. Di Somma, *Appl. Catal., B* **2015**, *170–171*, 90.
- [9] M. Gagliardi, *Photocatalysts: Technologies and Global Markets: AVM069A*; **2010**.
- [10] M. Gagliardi, *Photocatalysts: Technologies and Global Markets: AVM069B*; **2015**.
- [11] W. S. Koe, J. W. Lee, W. C. Chong, Y. L. Pang, L. C. Sim, *Environ. Sci. Pollut. Res.* **2020**, *27*, 2522.
- [12] A. Majumdar, A. Pal, *Clean Technol. Environ. Policy* **2020**, *22*, 11.
- [13] X. Xue, R. Chen, C. Yan, P. Zhao, Y. Hu, W. Zhang, S. Yang, Z. Jin, *Nano Res.* **2019**, *12*, 1229.
- [14] X. Li, J. Yu, M. Jaroniec, X. Chen, *Chem. Rev.* **2019**, *119*, 3962.
- [15] N. Vu, S. Kaliaguine, T. Do, *Adv. Funct. Mater.* **2019**, *29*, 1901825.
- [16] K. Dornelles, M. Roriz, V. F. Roriz, R. Caram, K. A. Dornelles, M. Roriz, V. F. Roriz, R. M. Caram, In *Conference Paper: ISES Solar World Congress 2011*; **2011**.
- [17] C. Acar, I. Dincer, G. F. Naterer, *Int. J. Energy Res.* **2016**, *40*, 1449.
- [18] P. Garcia-Muñoz, F. Fresno, V. A. de la Peña O’Shea, N. Keller, *Top. Curr. Chem.* **2020**, *378*, 6.
- [19] R. Dillert, D. H. Taffa, M. Wark, T. Bredow, D. W. Bahnemann, *APL Mater.* **2015**, *3*, 104001.
- [20] Y. AlSalka, L. I. Granone, W. Ramadan, A. Hakki, R. Dillert, D. W. Bahnemann, *Appl. Catal., B* **2019**, *244*, 1065.
- [21] F. W. Clarke, H. S. Washington, *The composition of the earth’s crust*; US Government Printing Office, **1924**.
- [22] B. F. Decker, J. S. Kasper, *Acta Crystallogr.* **1957**, *10*, 332.
- [23] S. M. Antao, I. Hassan, J. B. Parise, *Am. Mineral.* **2005**, *90*, 219.
- [24] A. Bloesser, J. Timm, H. Kurz, W. Milius, S. Hayama, J. Breu, B. Weber, R. Marschall, *Sol. RRL* **2020**, 1900570.

- [25] K. K. Kefeni, T. A. M. Msagati, T. T. Nkambule, B. B. Mamba, *Mater. Sci. Eng. C* **2020**, *107*, 110314.
- [26] C. Sun, J. S. H. Lee, M. Zhang, *Adv. Drug Deliv. Rev.* **2008**, *60*, 1252.
- [27] J. H. Kim, D. Hansora, P. Sharma, J. W. Jang, J. S. Lee, *Chem. Soc. Rev.* **2019**, *48*, 1908.
- [28] V. Quaschnig, *Erneuerbare Energien und Klimaschutz Hintergründe - Techniken und Planung - Ökonomie und Ökologie - Energiewende*; Carl Hanser Verlag GmbH & Co. KG, **2018**.
- [29] X. Yang, D. Wang, *ACS Appl. Energy Mater.* **2018**, *1*, 6657.
- [30] C. C. L. McCrory, S. Jung, I. M. Ferrer, S. M. Chatman, J. C. Peters, T. F. Jaramillo, *J. Am. Chem. Soc.* **2015**, *137*, 4347.
- [31] M. S. Prévot, K. Sivula, *J. Phys. Chem. C* **2013**, *117*, 17879.
- [32] S. Hu, M. R. Shaner, J. A. Beardslee, M. Lichterman, B. S. Brunschwig, N. S. Lewis, *Science* **2014**, *344*, 1005.
- [33] F. Bloch, *Zeitschrift für Phys.* **1929**, *52*, 555.
- [34] H. Kisch, *Semiconductor Photocatalysis - Principles and Applications*; Wiley-VCH, **2015**.
- [35] F. E. Osterloh, *ACS Energy Lett.* **2017**, *2*, 445.
- [36] D. X. Xu, Z. W. Lian, M. L. Fu, B. Yuan, J. W. Shi, H. J. Cui, *Appl. Catal., B* **2013**, *142–143*, 377.
- [37] G. Wang, B. Huang, X. Ma, Z. Wang, X. Qin, X. Zhang, Y. Dai, M.-H. Whangbo, *Angew. Chem., Int. Ed.* **2013**, *52*, 4810.
- [38] X. Liu, L. T. Su, S. K. Karuturi, J. Luo, L. Liu, X. Liu, J. Guo, T. C. Sum, R. Deng, H. J. Fan, A. I. Y. Tok, *Adv. Mater.* **2013**, *25*, 1603.
- [39] K. Sivula, R. van de Krol, *Nat. Rev. Mater.* **2016**, *1*, 15010.
- [40] X. Chen, Y. Low, A. C. S. Samia, C. Burda, J. L. Gole, *Adv. Funct. Mater.* **2005**, *15*, 41.
- [41] A. Mukherji, C.-H. Sun, S. C. Smith, G.-Q. Q. Lu, L.-Z. Wang, *J. Phys. Chem. C* **2011**, *115*, 15674.
- [42] K. Shankar, K. C. Tep, G. K. Mor, C. A. Grimes, *J. Phys. D.: Appl. Phys.* **2006**, *39*, 2361.
- [43] L. I. Granone, A. C. Ulpe, L. Robben, S. Klimke, M. Jahns, F. Renz, T. M. Gesing, T. Bredow, R. Dillert, D. W. Bahnemann, *Phys. Chem. Chem. Phys.* **2018**, *20*, 28267.
- [44] A. C. Ulpe, K. C. L. Bauerfeind, L. I. Granone, A. Arimi, L. Megatiff, R. Dillert, S. Warfsmann, D. H. Taffa, M. Wark, D. W. Bahnemann, T. Bredow, *Z. Phys. Chem.* **2020**, *234*, 719.
- [45] S. Harrison, *Exploring and Exploiting Charge-Carrier Confinement in Semiconductor Nanostructures*; Lancaster University, **2016**.
- [46] F. E. Osterloh, *Chem. Soc. Rev.* **2013**, *42*, 2294.
- [47] F. A. Chowdhury, M. L. Trudeau, H. Guo, Z. Mi, *Nat. Commun.* **2018**, *9*, 1.
- [48] Z. H. N. Al-Azri, W.-T. Chen, A. Chan, V. Jovic, T. Ina, H. Idriss, G. I. N. Waterhouse, *J. Catal.* **2015**, *329*, 355.
- [49] J. Yang, D. Wang, H. Han, C. Li, *Acc. Chem. Res.* **2013**, *46*, 1900.

-
- [50] R. Marschall, *Adv. Funct. Mater.* **2014**, *24*, 2421.
- [51] W. Gao, J. Lu, S. Zhang, X. Zhang, Z. Wang, W. Qin, J. Wang, W. Zhou, H. Liu, Y. Sang, *Adv. Sci.* **2019**, *6*, 1901244.
- [52] R. Li, H. Han, F. Zhang, D. Wang, C. Li, *Energy Environ. Sci.* **2014**, *7*, 1369.
- [53] N. Murakami, S. Kawakami, T. Tsubota, T. Ohno, *J. Mol. Catal. A: Chem.* **2012**, *358*, 106.
- [54] N. Satoh, T. Nakashima, K. Kamikura, K. Yamamoto, *Nat. Nanotechnol.* **2008**, *3*, 106.
- [55] A. S. Cherevan, L. Deilmann, T. Weller, D. Eder, R. Marschall, *ACS Appl. Energy Mater.* **2018**, *1*, 5787.
- [56] S. C. Warren, K. Voitchovsky, H. Dotan, C. M. Leroy, M. Cornuz, F. Stellacci, C. Hébert, A. Rothschild, M. Grätzel, *Nat. Mater.* **2013**, *12*, 842.
- [57] J. Li, N. Wu, *Catal. Sci. Technol.* **2015**, *5*, 1360.
- [58] W. Mönch, *Electronic Properties of Semiconductor Interfaces*; Springer, **2013**.
- [59] J. Kiwi, M. Grätzel, *J. Phys. Chem.* **1984**, *88*, 1302.
- [60] M. Hara, J. T. Lean, T. E. Mallouk, *Chem. Mater.* **2001**, *13*, 4668.
- [61] G. Blondeel, A. Harriman, G. Porter, D. Urwin, J. Kiwi, *J. Phys. Chem.* **1983**, *87*, 2629.
- [62] C. C. L. McCrory, S. Jung, I. M. Ferrer, S. M. Chatman, J. C. Peters, T. F. Jaramillo, *J. Am. Chem. Soc.* **2015**, *137*, 4347.
- [63] K. Maeda, K. Teramura, H. Masuda, T. Takata, N. Saito, Y. Inoue, K. Domen, *J. Phys. Chem. B* **2006**, *110*, 13107.
- [64] Y. Wu, H. Wang, Y. Sun, T. Xiao, W. Tu, X. Yuan, G. Zeng, S. Li, J. W. Chew, *Appl. Catal., B* **2018**, *227*, 530.
- [65] P. Voepel, M. Weiss, B. M. Smarsly, R. Marschall, *J. Photochem. Photobiol., A* **2018**, *366*, 34.
- [66] N. Serpone, E. Borgarello, M. Grätzel, *J. Chem. Soc., Chem. Commun.* **1984**, 342.
- [67] K. C. Christoforidis, P. Fornasiero, *ChemCatChem* **2017**, *9*, 1523.
- [68] P. Herrasti, L. Peter, *J. Electroanal. Chem. Interfacial Electrochem.* **1991**, *305*, 241.
- [69] A. B. Jorge, D. J. Martin, M. T. S. Dhanoa, A. S. Rahman, N. Makwana, J. Tang, A. Sella, F. Corà, S. Firth, J. A. Darr, P. F. McMillan, *J. Phys. Chem. C* **2013**, *117*, 7178.
- [70] G. Zhang, Z. A. Lan, L. Lin, S. Lin, X. Wang, *Chem. Sci.* **2016**, *7*, 3062.
- [71] T. A. Kandiel, I. Ivanova, D. W. Bahnemann, *Energy Environ. Sci.* **2014**, *7*, 1420.
- [72] K. Maeda, K. Domen, *J. Phys. Chem. C* **2007**, *111*, 7851.
- [73] A. Kudo, Y. Miseki, *Chem. Soc. Rev.* **2009**, *38*, 253.
- [74] X. Wang, K. Maeda, X. Chen, K. Takanabe, K. Domen, Y. Hou, X. Fu, M. Antonietti, *J. Am. Chem. Soc.* **2009**, *131*, 1680.
-

- [75] Q. Wang, M. Nakabayashi, T. Hisatomi, S. Sun, S. Akiyama, Z. Wang, Z. Pan, X. Xiao, T. Watanabe, T. Yamada, N. Shibata, T. Takata, K. Domen, *Nat. Mater.* **2019**, *18*, 827.
- [76] R. D. Shannon, *Acta Cryst.* **1976**, *A32*, 751.
- [77] V. Vasanthi, A. Shanmugavani, C. Sanjeeviraja, R. Kalai Selvan, *J. Magn. Magn. Mater.* **2012**, *324*, 2100.
- [78] K. Dileep, B. Loukya, N. Pachauri, A. Gupta, R. Datta, *J. Appl. Phys.* **2014**, *116*, 103505.
- [79] M. Ristić, B. Hannoyer, S. Popović, S. Musić, N. Bajraktaraj, *Mater. Sci. Eng., B* **2000**, *77*, 73.
- [80] M. P. Pasternak, S. Nasu, K. Wada, S. Endo, *Phys. Rev. B* **1994**, *50*, 6446.
- [81] V. Šepelák, D. Baabe, D. Mienert, F. J. Litterst, K. D. Becker, *Scr. Mater.* **2003**, *48*, 961.
- [82] H. L. Andersen, C. Granados-Miralles, M. Saura-Múzquiz, M. Stingaciu, J. Larsen, F. Søndergaard-Pedersen, J. V. Ahlburg, L. Keller, C. Frandsen, M. Christensen, *Mater. Chem. Front.* **2019**, *3*, 668.
- [83] H. S. C. O'Neill, *Eur. J. Mineral.* **1992**, *4*, 571.
- [84] Y. Hemmi, N. Ichikawa, N. Saito, T. Masuda, *J. Nucl. Sci. Technol.* **1994**, *31*, 1202.
- [85] D. H. Taffa, R. Dillert, A. C. Ulpe, K. C. L. Bauerfeind, T. Bredow, D. W. Bahnemann, M. Wark, *J. Photonics Energy* **2016**, *7*, 012009.
- [86] B. Ren, Y. Huang, C. Han, M. N. Nadagouda, D. D. Dionysiou, *Ferrites as Photocatalysts for Water Splitting and Degradation of Contaminants*; American Chemical Society, **2016**.
- [87] H. G. Kim, P. H. Borse, J. S. Jang, E. D. Jeong, O.-S. Jung, Y. J. Suh, J. S. Lee, *Chem. Commun.* **2009**, 5889.
- [88] H. Zazoua, A. Boudjemaa, R. Chebout, K. Bachari, *Int. J. Energy Res.* **2014**, *38*, 2010.
- [89] R. Dom, P. H. Borse, K.-S. Hong, S. Choi, B. S. Lee, M. G. Ha, J. P. Kim, E. D. Jeong, H. G. Kim, *J. Korean Phys. Soc.* **2015**, *67*, 1639.
- [90] K. Kirchberg, A. Becker, A. Bloesser, T. Weller, J. Timm, C. Suchomski, R. Marschall, *J. Phys. Chem. C* **2017**, *121*, 27126.
- [91] M. Shahid, L. Jingling, Z. Ali, I. Shakir, M. F. Warsi, R. Parveen, M. Nadeem, *Mater. Chem. Phys.* **2013**, *139*, 566.
- [92] J. Jiang, W. Fan, X. Zhang, H. Bai, Y. Liu, S. Huang, B. Mao, S. Yuan, C. Liu, W. Shi, *New J. Chem.* **2016**, *40*, 538.
- [93] K. Tezuka, M. Kogure, Y. J. Shan, *Catal. Commun.* **2014**, *48*, 11.
- [94] K. Shetty, B. S. Prathibha, D. Rangappa, K. S. Anantharaju, H.P. Nagaswarupa, H. Nagabhushana, S. C. Prashantha, *Mater. Today: Proc.* **2017**, *4*, 11764.
- [95] K. Shetty, B. S. Prathibha, D. Rangappa, K. S. Anantharaju, H. P. Nagaswarupa, V. Gangaraju, *Asian J. Chem.* **2020**, *32*, 501.
- [96] F. A. Benko, F. P. Koffyberg, *Mater. Res. Bull.* **1986**, *21*, 1183.

-
- [97] R. A. Henning, P. Uredat, C. Simon, A. Bloesser, P. Cop, M. T. Elm, R. Marschall, *J. Phys. Chem. C* **2019**, *123*, 18240.
- [98] R. Köferstein, T. Walther, D. Hesse, S. G. Ebbinghaus, *J. Mater. Sci.* **2013**, *48*, 6509.
- [99] T. P. Sumangala, I. Pasquet, L. Presmanes, Y. Thimont, C. Bonningue, N. Venkataramani, S. Prasad, V. Baco-Carles, P. Tailhades, A. Barnabé, *Ceram. Int.* **2018**, *44*, 18578.
- [100] Y. Huang, Y. Tang, J. Wang, Q. Chen, *Mater. Chem. Phys.* **2006**, *97*, 394.
- [101] W. Liu, R. Jin, Y. Li, Y. Wu, X. Cao, S. Hu, *Int. J. Electrochem. Sci.* **2018**, *13*, 9520.
- [102] S. Sun, H. Zeng, *J. Am. Chem. Soc.* **2002**, *124*, 8204.
- [103] S. Sun, H. Zeng, D. B. Robinson, S. Raoux, P. M. Rice, S. X. Wang, G. Li, *J. Am. Chem. Soc.* **2004**, *126*, 273.
- [104] M. Gateshki, V. Petkov, S. K. Pradhan, T. Vogt, *J. Appl. Crystallogr.* **2005**, *38*, 772.
- [105] Y. Matsumoto, M. Omae, K. Sugiyama, E. Sato, *J. Phys. Chem.* **1987**, *91*, 577.
- [106] Y. Matsumoto, M. Obata, J. Hombo, *J. Phys. Chem.* **1994**, *98*, 2950.
- [107] R. Dom, H. G. Kim, P. H. Borse, *ChemistrySelect* **2017**, *2*, 2556.
- [108] H. G. Kim, P. H. Borse, W. Choi, J. S. Lee, *Angew. Chem., Int. Ed.* **2005**, *44*, 4585.
- [109] Z. Liu, Z. G. Zhao, M. Miyauchi, *J. Phys. Chem. C* **2009**, *113*, 17132.
- [110] R. Das, S. Karna, Y. C. Lai, F. C. Chou, *Cryst. Growth Des.* **2016**, *16*, 499.
- [111] T. Hidayat, D. Shishin, S. A. Deckerov, E. Jak, *Met. Mater. Trans. B* **2016**, *47*, 256.
- [112] A. K. Das, R. Govindaraj, A. Srinivasanan, *J. Magn. Magn. Mater.* **2018**, *451*, 526.
- [113] G. Lal, K. Punia, S. N. Dolia, P. A. Alvi, S. Dalela, S. Kumar, *Ceram. Int.* **2019**, *45*, 5837.
- [114] A. Samariya, S. N. Dolia, A. S. Prasad, P. K. Sharma, S. P. Pareek, M. S. Dhawan, S. Kumar, *Curr. Appl. Phys.* **2013**, *13*, 830.
- [115] R. Wei, X. Lv, M. Yang, J. Xu, *Ultrason. Sonochem.* **2017**, *38*, 281.
- [116] N. Sharma, K. M. Shaju, G. V. Subba Rao, B. V. R. Chowdari, *J. Power Sources* **2003**, *124*, 204.
- [117] Z. Zhang, W. Wang, *Mater. Lett.* **2014**, *133*, 212.
- [118] J. Wang, Y. Wang, Y. Liu, S. Li, F. Cao, G. Qin, *Funct. Mater. Lett.* **2017**, *10*, 1750058.
- [119] A. M. EL-Rafei, A. S. El-Kalliny, T. A. Gad-Allah, *J. Magn. Magn. Mater.* **2017**, *428*, 92.
- [120] K. Kirchberg, R. Marschall, *Sustainable Energy Fuels* **2019**, *3*, 1150.
- [121] W. Kim, C. Y. Suh, S. W. Cho, K. M. Roh, H. Kwon, K. Song, I. J. Shon, *Talanta* **2012**, *94*, 348.
- [122] N. Pinna, S. Grancharov, P. Beato, P. Bonville, M. Antonietti, M. Niederberger, *Chem. Mater.* **2005**, *17*, 3044.
- [123] P. Xue, D. He, A. Xu, Z. Gu, Q. Yang, F. Engström, B. Björkman, *J. Alloys Compd.* **2017**, *712*, 640.
- [124] L. Zheng, K. Fang, M. Zhang, Z. Nan, L. Zhao, D. Zhou, M. Zhu, W. Li, *RSC Adv.* **2018**, *8*, 39177.
- [125] R. J. Harrison, A. Putnis, *Surv. Geophys.* **1998**, *19*, 461.
-

- [126] M. Sultan, R. Singh, *J. Phys. D.: Appl. Phys.* **2009**, *42*, 115306.
- [127] S. Piccinin, *Phys. Chem. Chem. Phys.* **2019**, *21*, 2957.
- [128] B. Fromme, *d-d Excitations in Transition-Metal Oxides: A Spin-Polarized Electron Energy-Loss Spectroscopy (SPEELS) Study*; Springer, **2007**.
- [129] P. A. Cox, *Transition Metal Oxides: An Introduction to Their Electronic Structure and Properties*; Oxford University Press, **2010**.
- [130] D. M. Sherman, *Phys. Chem. Miner.* **1985**, *12*, 161.
- [131] C. Lohaus, *The Fermi Level in Hematite - Doping, Band Alignment, and Charge Transitions*; Technische Universität Darmstadt, **2018**.
- [132] C. Lohaus, A. Klein, W. Jaegermann, *Nat. Commun.* **2018**, *9*, 1.
- [133] Y. Tanabe, S. Sugano, *J. Phys. Soc. Jpn.* **1954**, *9*, 753.
- [134] A. F. Hollemann, N. Wiberg, *Lehrbuch der anorganischen Chemie, 102. Aufl.*; Walter de Gruyter & Co.: Berlin, New York.
- [135] M. Victory, R. P. Pant, S. Phanjoubam, *Mater. Chem. Phys.* **2020**, *240*, 122210.
- [136] M. A. Willard, L. K. Kurihara, E. E. Carpenter, S. Calvin, V. G. Harris, *Int. Mater. Rev.* **2004**, *49*, 125.
- [137] S. Bansal, Y. Kumar, D. K. Das, P. P. Singh, *Chem. Chem. Technol.* **2019**, *13*, 163.
- [138] N. Domracheva, M. Caporali, E. Rentschler, *Novel Magnetic Nanostructures*; 2018.
- [139] L. M. Corliss, J. M. Hastings, W. Kunmann, *Phys. Rev.* **1967**, *160*, 408.
- [140] P. Heidari, S. M. Masoudpanah, *J. Mater. Res. Technol.* **2020**, *9*, 4469.
- [141] A. H. Lu, E. L. Salabas, F. Schüth, *Angew. Chem., Int. Ed.* **2007**, *46*, 1222.
- [142] S. P. Yeap, J. Lim, B. S. Ooi, A. L. Ahmad, *J. Nanoparticle Res.* **2017**, *19*, 368.
- [143] Y. Lu, Y. Yin, B. T. Mayers, Y. Xia, *Nano Lett.* **2002**, *2*, 183.
- [144] T. Tago, T. Hatsuta, K. Miyajima, M. Kishida, S. Tashiro, K. Wakabayashi, *J. Am. Ceram. Soc.* **2002**, *85*, 2188.
- [145] M. Fröba, R. Köhn, G. Bouffaud, O. Richard, G. Van Tendeloo, *Chem. Mater.* **1999**, *11*, 2858.
- [146] Z. Xu, C. Li, X. Kang, D. Yang, P. Yang, Z. Hou, J. Lin, *J. Phys. Chem. C* **2010**, *114*, 16343.
- [147] F. Hoffmann, M. Cornelius, J. Morell, M. Fröba, *Angew. Chem., Int. Ed.* **2006**, *45*, 3216.
- [148] H. H. Weetall, *Biochim. Biophys. Acta, Enzymol.* **1970**, *212*, 1.
- [149] D. Margolese, J. A. Melero, S. C. Christiansen, B. F. Chmelka, G. D. Stucky, *Chem. Mater.* **2000**, *12*, 2448.
- [150] J. Timm, R. Marschall, *Adv. Sustain. Syst.* **2018**, *2*, 1700170.
- [151] M. Cornelius, F. Hoffmann, M. Fröba, *Chem. Mater.* **2005**, *17*, 6674.
- [152] F. Kleitz, S. H. Choi, R. Ryoo, *Chem. Commun.* **2003**, 2136.

-
- [153] G. M. Do Nascimento, *Introductory Chapter: The Multiple Applications of Raman Spectroscopy*; IntechOpen, **2018**.
- [154] P. Kubelka, F. Munk, *Z. Tech. Phys.* **1931**, *12*, 593.
- [155] J. Tauc, *Mater. Res. Bull.* **1968**, *3*, 37.
- [156] M. Bauer, *Phys. Chem. Chem. Phys.* **2014**, *16*, 13827.
- [157] P. Glatzel, M. Sikora, G. Smolentsev, M. Fernández-García, *Catal. Today* **2009**, *145*, 294.
- [158] E. Gallo, P. Glatzel, *Adv. Mater.* **2014**, *26*, 7730.
- [159] R. L. Mössbauer, *Z. Phys.* **1958**, *151*, 124.
- [160] D. G. Rancourt, J. Y. Ping, *Nucl. Instruments Methods Phys. Res. Sect. B* **1991**, *58*, 85.
- [161] J. Clarke, A. I. Braginsk, *The SQUID Handbook Vol. 1, Fundamentals and technology of SQUIDs and SQUID systems*; Wiley-VCH, **2004**.
- [162] R. Doll, M. Näbauer, *Phys. Rev. Lett.* **1961**, *7*, 51.
- [163] B. D. Josephson, *Phys. Lett.* **1962**, *1*, 251.
- [164] M. Thommes, K. Kaneko, A. V Neimark, J. P. Olivier, F. Rodriguez-Reinoso, J. Rouquerol, K. S. W. Sing, *Pure Appl. Chem* **2015**, *87*, 1051.
- [165] S. Brunauer, P. H. Emmett, E. Teller, *J. Am. Chem. Soc.* **1938**, *60*, 309.
- [166] J. Rouquerol, P. Llewellyn, F. Rouquerol, *Stud. Surf. Sci. Catal.* **2007**, *160*, 49.
- [167] E. W. Washburn, *Phys. Rev.* **1921**, *17*, 273.
- [168] Z. Zhao, R. V. Goncalves, S. K. Barman, E. J. Willard, E. Byle, R. Perry, Z. Wu, M. N. Huda, A. J. Moulé, F. E. Osterloh, *Energy Environ. Sci.* **2019**, *12*, 1385.
- [169] C. Baumanis, J. Z. Bloh, R. Dillert, D. W. Bahnemann, *J. Phys. Chem. C* **2011**, *115*, 25442.
- [170] A. Hankin, F. E. Bedoya-Lora, J. C. Alexander, A. Regoutz, G. H. Kelsall, *J. Mater. Chem. A* **2019**, *7*, 26162.
- [171] C. Suchomski, B. Breitung, R. Witte, M. Knapp, S. Bauer, T. Baumbach, C. Reitz, T. Brezesinski, *Beilstein J. Nanotechnol.* **2016**, *7*, 1350.
- [172] M. Niederberger, G. Garnweitner, *Chem. - Eur. J.* **2006**, *12*, 7282.
- [173] Z. Wang, P. Lazor, S. K. Saxena, H. S. C. O'Neill, *Mater. Res. Bull.* **2002**, *37*, 1589.
- [174] A. M. Jubb, H. C. Allen, *ACS Appl. Mater. Interfaces* **2010**, *2*, 2804.
- [175] B. I. Pokrovskii, A. K. Gapeev, K. V. Pokholov, L. N. Kommissarova, I. V. Igonina, A. M. Babeshkin, *Kristallografiya* **1972**, *17*, 793.
- [176] R. D. Waldron, *Phys. Rev.* **1955**, *99*, 1727.
- [177] P. Dutta, S. Pal, M. S. Seehra, N. Shah, G. P. Huffman, *J. Appl. Phys.* **2009**, *105*, 07B501.
- [178] C. J. Chang, Z. Lee, M. D. Wei, C. C. Chang, K. W. Chu, *Int. J. Hydrogen Energy* **2015**, *40*, 11436.
- [179] N. Pailhé, A. Wattiaux, M. Gaudon, A. Demourgues, *J. Solid State Chem.* **2008**, *181*, 1040.
-

- [180] A. Gaur, B. D. Shrivastava, H. L. Nigam, *Proc. Indian Natl. Sci. Acad., Part B* **2013**, *79*, 921.
- [181] F. M. F. De Groot, P. Glatzel, U. Bergmann, P. A. Van Aken, R. A. Barrea, S. Klemme, M. Hävecker, A. Knop-Gericke, W. M. Heijboer, B. M. Weckhuysen, *J. Phys. Chem. B* **2005**, *109*, 20751.
- [182] F. De Groot, G. Vankó, P. Glatzel, *J. Phys.: Condens. Matter* **2009**, *21*, 104207.
- [183] T. E. Westre, P. Kennepohl, J. G. DeWitt, B. Hedman, K. O. Hodgson, E. I. Solomon, *J. Am. Chem. Soc.* **1997**, *119*, 6297.
- [184] F. De Groot, *Chem. Rev.* **2001**, *101*, 1779.
- [185] P. Glatzel, In *AIP Conference Proceedings*; **2003**; pp. 250–255.
- [186] P. Glatzel, U. Bergmann, *Coord. Chem. Rev.* **2005**, *249*, 65.
- [187] B. Gilbert, C. Frandsen, E. R. Maxey, D. M. Sherman, *Phys. Rev. B* **2009**, *79*, 035108.
- [188] M. Nowakowski, J. Czaplá-Masztafiak, J. Szlachetko, W. M. Kwiatek, *Chem. Phys.* **2017**, *493*, 49.
- [189] M. Pichler, J. Szlachetko, I. E. Castelli, N. Marzari, M. Döbeli, A. Wokaun, D. Pergolesi, T. Lippert, *ChemSusChem* **2017**, *10*, 2099.
- [190] J. Szlachetko, K. Michalow-Mauke, M. Nachtegaal, J. Sá, *J. Chem. Sci.* **2014**, *126*, 511.
- [191] S. Biswas, S. Wallentine, S. Bandaranayake, L. R. Baker, *J. Chem. Phys.* **2019**, *151*, 104701.
- [192] Z. Ž. Lazarević, D. L. Sekulić, V. N. Ivanovski, N. Ž. Romčević, *Int. J. Mater. Metall. Eng.* **2015**, *9*, 1066.
- [193] K. N. Subramanyam, *J. Phys. C: Solid State Phys.* **1971**, *4*, 2266.
- [194] M. J. Thompson, K. J. Blakeney, S. D. Cady, M. D. Reichert, J. Del Pilar-Albaladejo, S. T. White, J. Vela, *Chem. Mater.* **2016**, *28*, 1668.
- [195] N. Kolev, M. N. Iliev, V. N. Popov, M. Gospodinov, *Solid State Commun.* **2003**, *128*, 153.
- [196] N. C. Hildebrandt, J. Soldat, R. Marschall, *Small* **2015**, *11*, 2051.
- [197] D. Hirabayashi, Y. Sakai, T. Yoshikawa, K. Mochizuki, Y. Kojima, K. Suzuki, K. Ohshita, Y. Watanabe, *Hyperfine Interact.* **2006**, *167*, 809.
- [198] Y. Xu, M. A. A. Schoonen, *Am. Mineral.* **2000**, *85*, 543.
- [199] L. Stegbauer, S. Zech, G. Savasci, T. Banerjee, F. Podjaski, K. Schwinghammer, C. Ochsenfeld, B. V. Lotsch, *Adv. Energy Mater.* **2018**, *8*, 1703278.
- [200] D. Macina, A. Opióła, M. Rutkowska, S. Basąg, Z. Piwowarska, M. Michalik, L. Chmielarz, *Mater. Chem. Phys.* **2017**, *187*, 60.
- [201] T. N. Tran, T. Van Anh Pham, M. L. Phung Le, T. P. Thoa Nguyen, V. M. Tran, *Adv. Nat. Sci. Nanosci. Nanotechnol.* **2013**, *4*, 045007.
- [202] F. Bretschneider, *Eine Untersuchung über die allgemeine Anwendbarkeit der CVD-vermittelten Silanisierung*; University of Bayreuth, 2019.

7 Appendix

7.1 Additional figures

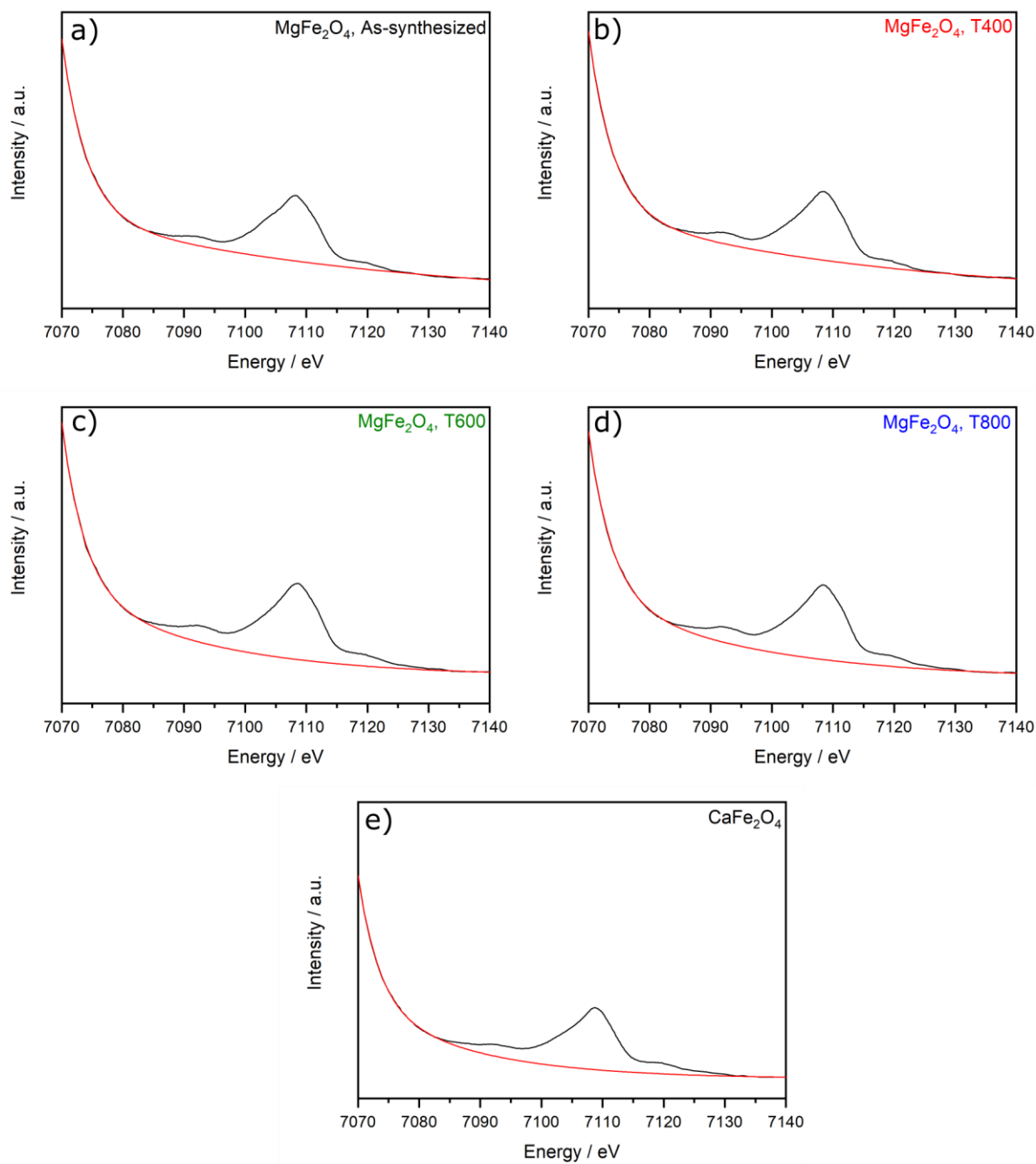


Figure A1: Fit curves that were used for the removal of the $K\beta_{1,3}$ fluorescence background of the VtC spectra of $MgFe_2O_4$ and $CaFe_2O_4$.

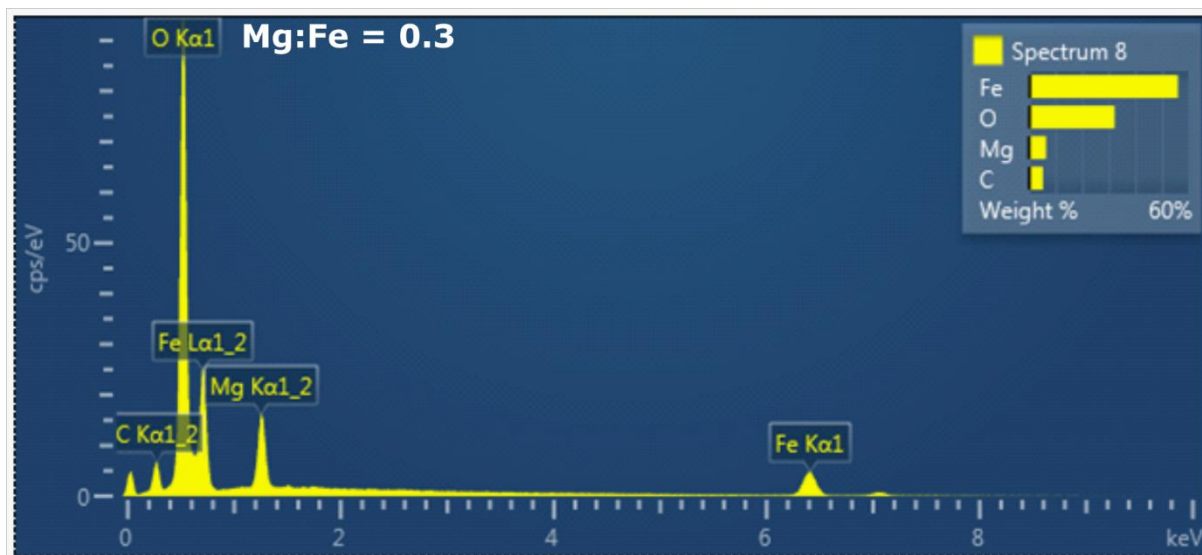


Figure A2: Exemplary EDX spectrum of MgFe₂O₄ nanoparticles synthesized at 200 °C according to the synthesis of Kirchberg et al., prior to optimization of the stoichiometry.

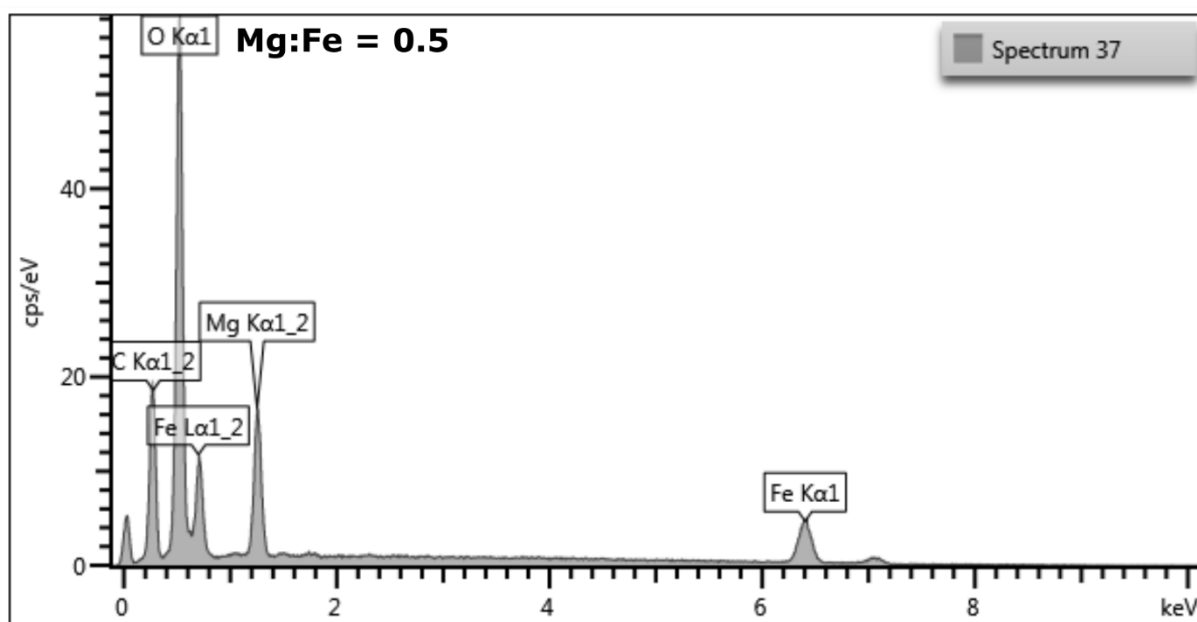


Figure A3: Exemplary EDX spectrum of MgFe₂O₄ nanoparticles synthesized at 200 °C with an optimized precursor stoichiometry.

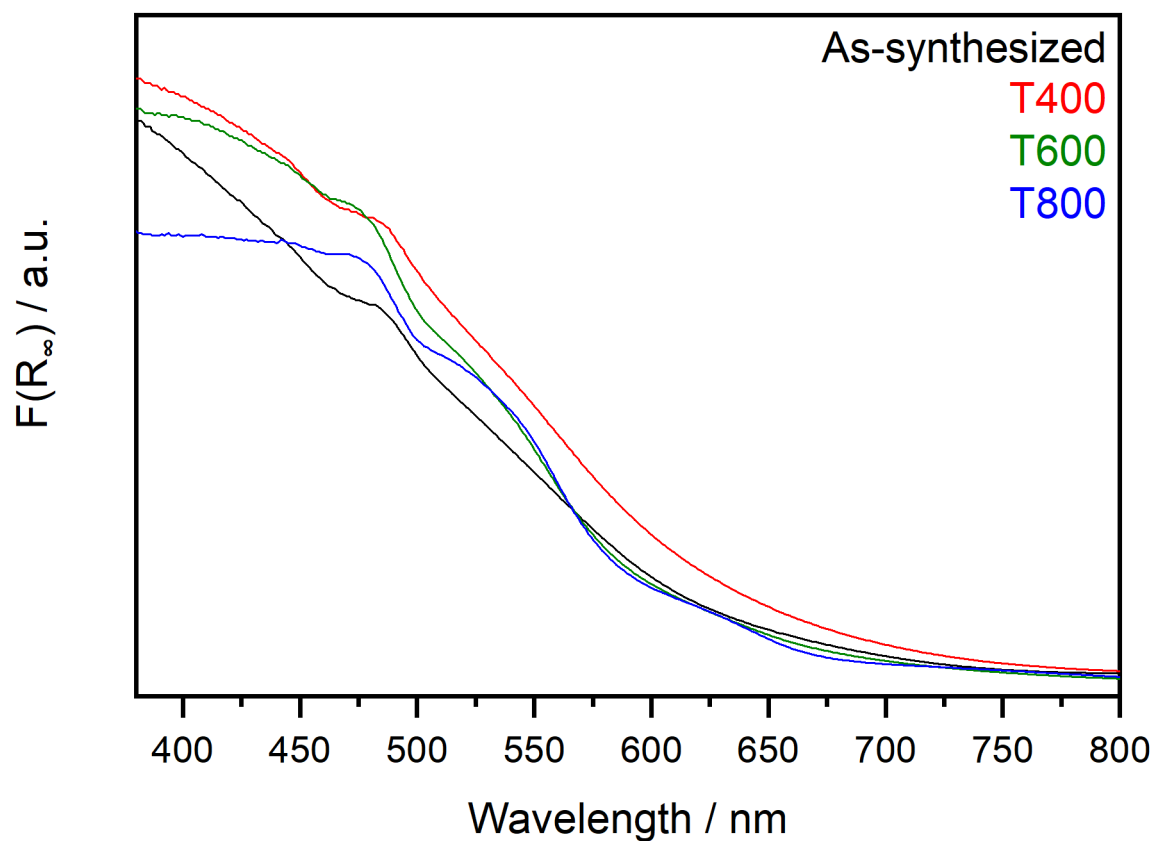


Figure A4: Kubelka-Munk absorption spectra of MgFe₂O₄ nanoparticles synthesized at a microwave temperature of 200 °C and calcined at 400 °C, 600 °C and 800 °C under air for one hour.

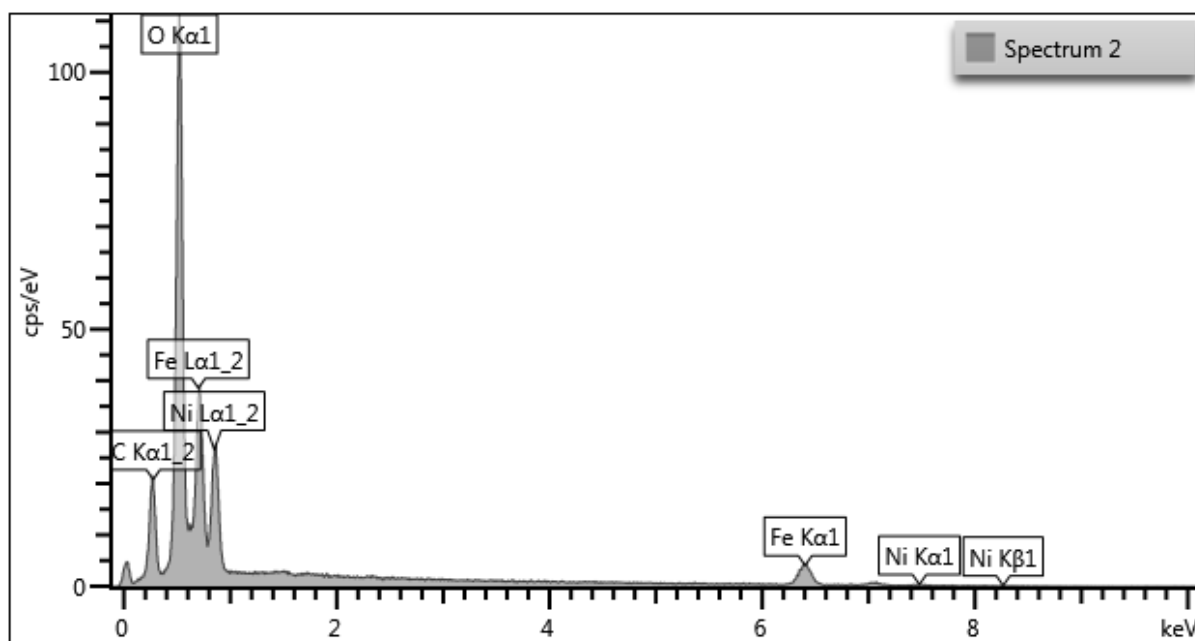


Figure A5: Exemplary EDX spectrum of NiFe₂O₄ nanoparticles synthesized at 225 °C.

7.1 Additional figures

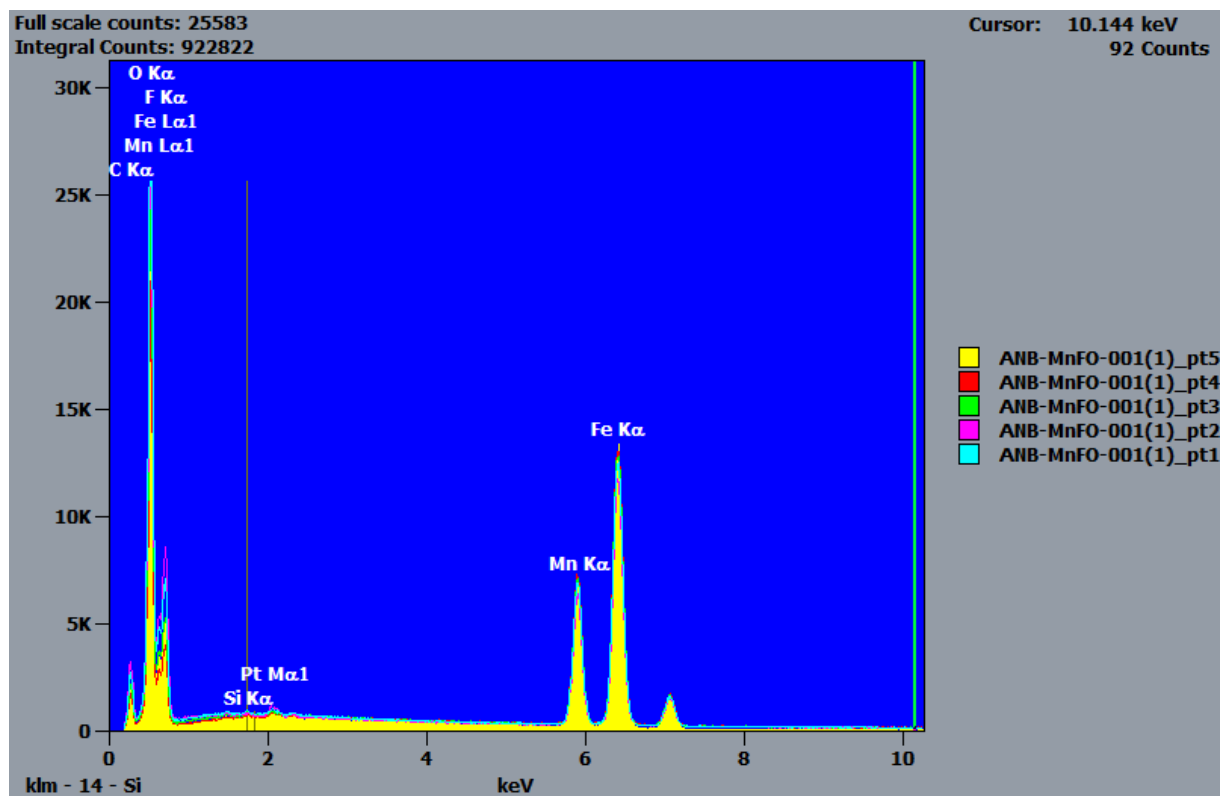


Figure A6: Exemplary EDX spectrum of MnFe₂O₄ nanoparticles synthesized at 250 °C.

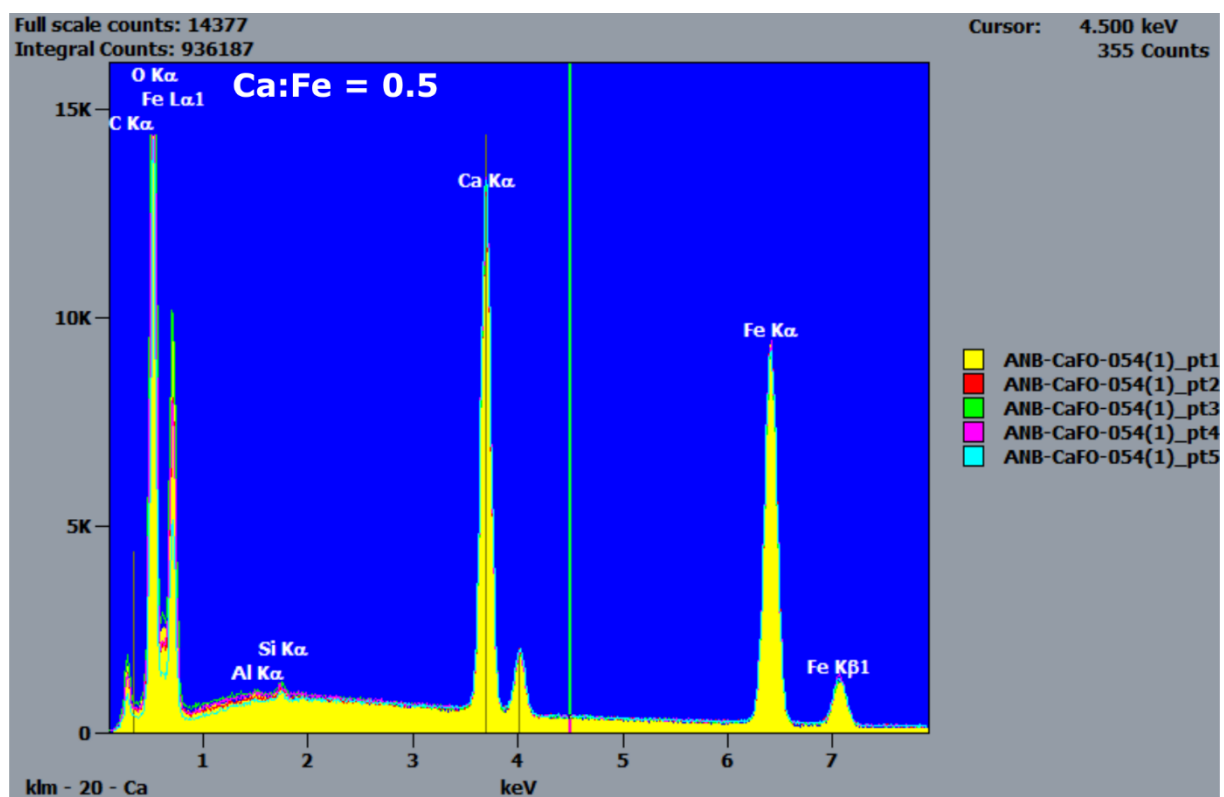


Figure A7: Exemplary EDX spectrum of macroporous CaFe₂O₄.

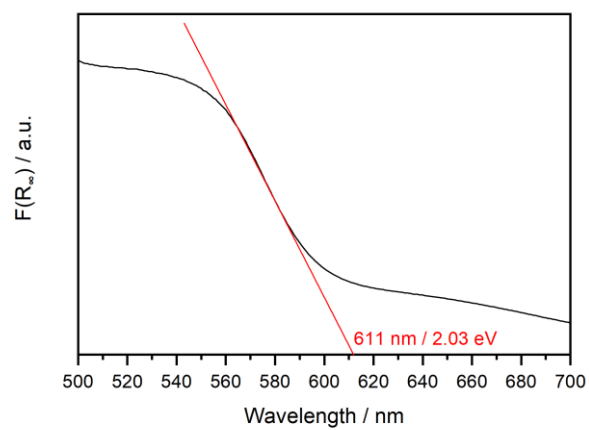


Figure A8: Kubelka-Munk absorption spectrum of the $\alpha\text{-Fe}_2\text{O}_3$ powder that was measured as a reference in the X-ray emission spectroscopy experiments.

7.2 List of symbols and abbreviations

OAc	Acetate
acac	Acetylacetonate
ATR	Attenuated total reflection
BET	Brunauer-Emmet-Teller
CB	Conduction band
CBM	Conduction band minimum
CLV	Chopped light voltammetry
CVD	Chemical vapor deposition
$d_{\text{Crystallite}}$	Crystallite diameter
DSC	Differential scanning calorimetry
E_{F}	Fermi level
$E_{\text{F,redox}}$	RedOx Fermi potential
E_{g}	Band gap energy
E_{ox}	Oxidation potential
E_{ph}	Photon energy
E_{red}	Reduction potential
EDX	Energy-dispersive X-ray spectroscopy
<i>e.g.</i>	<i>exempli gratia</i> (for example)
fcc	Face centered cubic
FTIR	Fourier-transform infrared
FTO	Fluorine doped tin oxide
FWHM	Full width at half maximum
HERFD	High energy resolution fluorescence detected
HOMO	Highest occupied molecular orbital
I_0	Direct current through superconducting loop
I_s	Screening current
I_c	Critical current
IPCE	Incident photon to current efficiency
IR	Infrared
LCAO	Linear combination of atomic orbitals
LMCT	Ligand-to-metal charge transfer
LUMO	Lowest unoccupied molecular orbital
MIP	Mercury intrusion porosimetry
MPTMS	3-Mercaptopropyl)trimethoxysilane
M_s	Saturation magnetization
$M_{s,\text{corr}}$	Corrected saturation magnetization
NIR	Near infrared
NLDFT	Non-local density functional theory
OAc	Acetate
PHD	pulse-height discrimination
Φ_{B}	Schottky Barrier height
PMO	periodic mesoporous organosilica
PTFE	Polytetrafluoroethylene
PXRD	powder X-ray diffraction

RedOx	Reduction-oxidation
RhB	Rhodamine B
RHE	Reversible hydrogen electrode
SAED	Selected area electron diffraction
SAPXRD	Small angle powder X-ray diffraction
SAXS	Small angle X-ray scattering
S_{BET}	BET surface area
SEM	Scanning electron microscope
SQUID	Superconducting quantum interference device
SSR	solid-state reaction
STH	solar-to-hydrogen efficiency
T_{B}	Blocking temperature
T_{Calc}	Calcination temperature
TEM	Transmission electron microscopy
TFY	Total fluorescence yield
TGA	Thermogravimetric analysis
T_{MW}	Microwave temperature
UV	ultraviolet
VB	Valence band
VBM	Valence band minimum
VtC	Valence-to-core
WAPXRD	Wide angle powder X-ray diffraction
XANES	X-ray absorption near edge structure spectroscopy
XAS	X-ray absorption spectroscopy
XES	X-ray emission spectroscopy
ZFCM	Zero field cooled magnetization

7.3 Publications derived from this PhD work

- [1] K. Kirchberg, A. Becker, A. Bloesser, T. Weller, J. Timm, C. Suchomski, R. Marschall; "Stabilization of Monodisperse, Phase-Pure MgFe_2O_4 Nanoparticles in Aqueous and Nonaqueous Media and Their Photocatalytic Behavior", *J. Phys. Chem. C* **2017**, *121*, 27126.
- [2] R. A. Henning, P. Uredat, C. Simon, A. Bloesser, P. Cop, M. T. Elm, R. Marschall; "Characterization of MFe_2O_4 (M = Mg, Zn) Thin Films Prepared by Pulsed Laser Deposition for Photoelectrochemical Applications", *J. Phys. Chem. C* **2019**, *123*, 18240.
- [3] J. Timm, A. Bloesser, S. Zhang, C. Scheu, R. Marschall; "Stabilization of nanosized MgFe_2O_4 nanoparticles in phenylene-bridged KIT-6-type ordered mesoporous organosilica (PMO)", *Microporous Mesoporous Mater.* **2019**, *293*, 1.
- [4] A. Bloesser, J. Timm, H. Kurz, W. Milius, J. Brey, B. Weber, R. Marschall; "A Novel Synthesis Yielding Macroporous CaFe_2O_4 Sponges for Solar Energy Conversion", *Sol. RRL* **2020**, 1900570.
- [5] A. Bloesser, H. Kurz, J. Timm, F. Wittkamp, C. Simon, S. Hayama, B. Weber, U. P. Apfel, R. Marschall; "Tailoring the Size, Inversion Parameter, and Absorption of Phase Pure Magnetic MgFe_2O_4 Nanoparticles for Photocatalytic Degradations", *ACS Appl. Nano Mater.* **2020**, *3*, 11587.

7.4 Other publications

- [1] A. Bloesser, P. Voepel, M. O. Loeh, A. Beyer, K. Volz, R. Marschall; "Tailoring the diameter of electrospun layered perovskite nanofibers for photocatalytic water splitting", *J. Mater. Chem. A* **2018**, *6*, 1971.
- [2] A. Bloesser, R. Marschall; "Layered Perovskite Nanofiber Heterojunctions with Tailored Diameter to Enhance Photocatalytic Water Splitting Performance", *ACS Appl. Energy Mater.* **2018**, *1*, 2520.
- [3] D. Tetzlaff, C. Simon, D. S. Achilleos, M. Smialkowski, K. Junge, A. Bloesser, S. Piontek, H. Kasap, D. Siegmund, E. Reisner, R. Marschall, U.-P. Apfel; " $\text{Fe}_x\text{Ni}_{9-x}\text{S}_8$ (x = 3–6) as potential photocatalysts for solar-driven hydrogen production?", *Faraday Discuss.* **2019**, *215*, 216.
- [4] D. R. Wagner; K. Ament; L. Mayr; T. Martin; A. Bloesser; H. Schmalz; R. Marschall; F. E. Wagner; J. Brey; "Terrestrial Solar Radiation Driven Photodecomposition of Ciprofloxacin in Clinical Wastewater Applying Mesostructured Iron (III) Oxide", *Environ. Sci. Pollut. Res.* **2020**.

7.5 Contributions

- [1] “Synthesis and characterization of MgFe_2O_4 nanocrystals towards applications as photocatalyst in renewable fuel generation and green chemistry” André Blösser, Kristin Kirchberg, Roland Marschall, *6th International Conference on Semiconductor Photochemistry (SP6)*, Oldenburg, Germany, 11th to 14th of September 2017, poster contribution.
- [2] “Revisiting the microwave-assisted water-free synthesis of MgFe_2O_4 nanoparticles towards applications in photocatalysis” André Bloesser, Christopher Simon, Roland Marschall, *19th International Symposium on the Reactivity of Solids (ISRS-19)*, Bayreuth, Germany, 15th to 18th of July, poster contribution.
- [3] “Revisiting the microwave-assisted water-free synthesis of MgFe_2O_4 nanoparticles towards applications in photocatalysis” André Bloesser, Christopher Simon, Roland Marschall, *7th EuChemS Chemistry Congress*, Liverpool, United Kingdom, 26th to 30th of August, 2018, poster contribution.
- [4] “Revisiting the microwave-assisted water-free synthesis of MgFe_2O_4 nanoparticles towards applications in photocatalysis” André Bloesser, Christopher Simon, Roland Marschall, *2. Jahrestagung der Fachgruppe Chemie und Energie (GDCH)*, Mülheim (Ruhr), Germany, 30th of September to 2nd of October 2018, oral presentation.
- [5] “Combination of two different light absorbing materials – creating a new potent visible light absorbing photocatalyst” Jana Timm, André Bloesser, Roland Marschall, *6th International Conference on Multifunctional, Hybrid and Nanomaterials*, Sitges, Spain, 11th to 15th of March 2019, oral presentation.
- [6] “Synthesis and characterization of MgFe_2O_4 nanoparticles towards applications in photocatalysis” André Bloesser, Roland Marschall, *Bunsentagung 2019 - 118th General Assembly of the German Bunsen Society for Physical Chemistry*, Jena, Germany, 30th of May to 1st of June 2019, poster contribution.
- [7] “Synthesis and characterization of magnesium ferrite nanoparticles for photocatalytic applications” André Bloesser, Roland Marschall, *7th International Conference on Semiconductor Photochemistry (SP7)*, Milano, Italy, 11th to 14th of September 2019, poster contribution.

8 Acknowledgements

Meinem Doktorvater Prof. Dr. Roland Marschall möchte ich ganz herzlich dafür danken, dass er mit der spannenden Thematik der Photokatalyse mein Interesse an der physikalischen Chemie wecken konnte und mir die Möglichkeit gab, zahlreiche Praktika, die Masterarbeit und schließlich die Promotion in seiner Arbeitsgruppe zu absolvieren. Vielen Dank für die Unterstützung und dafür, dass du immer ein offenes Ohr hattest, egal worum es ging. Wenn ich mich mit meiner Forschung einmal in einer Sackgasse wähnte, konnte ich mir immer sicher sein, dass du mit einem Schwall guter Ideen wieder für neue Motivation sorgst. Vielen Dank auch für die Möglichkeit, an so vielen internationalen Konferenzen teilnehmen zu können und wissenschaftliche Großeinrichtungen wie Synchrotronstrahlenquellen besuchen zu können. Das waren natürlich Highlights während der Promotion. Besonders gefreut habe ich mich auch darüber, dass die Vereinbarkeit von Arbeit und Familie in der AG Marschall so gut funktioniert.

Entsprechend möchte ich an dieser Stelle auch meiner Familie für das gleiche danken :) Allen voran meiner Frau Wiebke, die große Opfer gebracht hat, damit ich meine Promotion in Bayreuth weiterführen kann und die mich während der gesamten Zeit großartig unterstützt hat. Danke auch an meine Töchter Fenja und Elin, für jedes Lachen, das mir beim Nachhausekommen entgegengestrahlt ist. Bei meinen Eltern möchte ich mich für die durchgehende Unterstützung während meines Studiums und des gesamten Lebens bedanken. Danke auch an meine Schwester, Wiebkes Familie und alle meine Freunde, die in der Freizeit und auf vielen Festivals immer für die nötige Abwechslung gesorgt haben.

Bei allen aktuellen und ehemaligen Mitgliedern der AG Marschall möchte ich mich für die große Hilfsbereitschaft, die tolle Arbeitsatmosphäre und die vielen Messungen, die ihr für mich durchgeführt habt, bedanken. Besonderer Dank gilt Jana Timm, für ihre Hilfe bei der Planung und Durchführung der Synchrotron-Messungen und Morten Weiß und Christopher Simon für ihre Unterstützung während dieser Forschungsaufenthalte. Morten Weiß gebührt weiterhin besonderer Dank für sein unfassbares Engagement bei der Organisation unserer Labore und seine fachkundige Unterstützung bei vielen Experimenten.

Bedanken möchte ich mich auch bei der Arbeitsgruppe Smarsly in Gießen, für die Möglichkeit, in der ersten Hälfte der Promotion viele Arbeiten in ihren Laboren durchzuführen und für die Unterstützung während dieser Zeit. Danke für die produktiven Diskussionen und Anregungen, egal ob in den Seminaren oder in der Kaffeeküche. Vielen Dank an alle dort, die Messungen für mich durchgeführt haben und mir so – auch nach meinem Wechsel an die Uni Bayreuth – sehr geholfen haben. Besonders danken möchte ich hierbei Rafael Meusch für die Quecksilberporosimetrie und Kevin Turke, der mein Ansprechpartner und Koordinator für kleinere Messungen aller Art war. Besonderer Dank gilt auch den

Duderinos dafür, dass man abseits der Arbeit, beim Cocktailwürfeln oder legendären Towerfall Ascension Duellen einfach mal auf andere Gedanken kommen konnte.

Für die gute Zusammenarbeit im Zuge des Projektes QuinoLight geht mein Dank an Dr. Jonathan Bloh, Prof. Dr. Dirk Ziegenbalg, Julia Patzsch und Fabian Guba. Für die finanzielle Unterstützung im Zuge dieses Projektes möchte ich der Arbeitsgemeinschaft industrieller Forschungsvereinigungen (AIF) danken.

Prof. Dr. Ulf Peter Apfel und Florian Wittkamp danke ich für Mößbauer Spektroskopie, Hubert Wörner, Kevin Turke, Felix Badaczewski und Kevin Ament für die thermogravimetrische Analyse, Hannah Kurz und Prof. Dr. Birgit Weber für Mößbauer Spektroskopie und SQUID Magnetometrie und Markus Drechsler, Kristin Kirchberg, Pascal Vöpel, Elif Özkan und Christopher Simon für die Transmissionselektronenmikroskopie. Marion Breunig danke ich für ihre Hilfe bei der FTIR Spektroskopie und Dr. Wolfgang Milius für seine Hilfe bei *in-situ* PXRD Messungen. Kristina Kvashnina und Shusaku Hayama möchte ich für ihre Unterstützung bei den Messungen mit Synchrotronstrahlung danken.

Mein Dank gilt außerdem natürlich allen, die an dieser Stelle vergessen wurden.

9 Eidesstattliche Versicherung und Erklärung

(§ 8 Satz 2 Nr. 3 PromO Fakultät)

Hiermit versichere ich eidesstattlich, dass ich die Arbeit selbstständig verfasst und keine anderen als die von mir angegebenen Quellen und Hilfsmittel benutzt habe (vgl. Art. 64 Abs. 1 Satz 6 BayHSchG).

(§ 8 Satz 2 Nr. 3 PromO Fakultät)

Hiermit erkläre ich, dass ich die Dissertation nicht bereits zur Erlangung eines akademischen Grades eingereicht habe und dass ich nicht bereits diese oder eine gleichartige Doktorprüfung endgültig nicht bestanden habe.

(§ 8 Satz 2 Nr. 4 PromO Fakultät)

Hiermit erkläre ich, dass ich Hilfe von gewerblichen Promotionsberatern bzw. –vermittlern oder ähnlichen Dienstleistern weder bisher in Anspruch genommen habe noch künftig in Anspruch nehmen werde.

(§ 8 Satz 2 Nr. 7 PromO Fakultät)

Hiermit erkläre ich mein Einverständnis, dass die elektronische Fassung der Dissertation unter Wahrung meiner Urheberrechte und des Datenschutzes einer gesonderten Überprüfung unterzogen werden kann.

(§ 8 Satz 2 Nr. 8 PromO Fakultät)

Hiermit erkläre ich mein Einverständnis, dass bei Verdacht wissenschaftlichen Fehlverhaltens Ermittlungen durch universitätsinterne Organe der wissenschaftlichen Selbstkontrolle stattfinden können.

.....
Ort, Datum, Unterschrift